UNIVERSITY OF CALIFORNIA, SAN DIEGO

METHODS AND DEVICES FOR COMPREHENSIVE MOLECULAR ANALYSIS OF SINGLE CELLS

A dissertation submitted in partial satisfaction of the requirements
for the degree Doctor of Philosophy

in

Bioengineering

by

Alexander Philip Hsiao

Committee in Charge:

Professor Xiaohua Huang, Chair
Professor Michael Heller, Co-Chair
Professor Sadik Esener
Professor Shyni Varghese
Professor Liangfang Zhang

2012

The Dissertation of Alexander Philip Hsiao is approved, and it is acceptable in quality and form for publication on microfilm and electronically:

_____

_____

_____

_____
Co-Chair

_____
Chair

University of California, San Diego

2012

DEDICATION

To my family and my fiancée,

Thank you so much for your unending advice, support, and love.

TABLE OF CONTENTS

Signature Page ..... **iii**

Dedication ..... **iv**

Table of Contents ..... **v**

List of Figures ..... **viii**

Acknowledgements ..... **xii**

Curriculum Vita ..... **xv**

Abstract of the Dissertation ..... **xvii**

1 Introduction **1**

1.1 Single-cell Analysis 1

1.2 Current Methods for Single-cell Analysis 2

1.3 Scope of the Dissertation 4

1.4 References 6

2 Microfluidic Devices for Single-Cell Capture, Isolation, and Lysis **11**

2.1 Abstract 11

2.2 Introduction 12

2.3 Dielectrophoretic Cell Capture Devices 13

2.3.1 Introduction 13

2.3.2 Experimental Methods 15

2.3.3 Results and Discussion 22

2.3.4 Summary 27

2.4 Hydrodynamic Cell Capture Devices 27

2.4.1 Introduction 27

2.4.2 Experimental Methods 30

2.4.3 Results and Discussion 41

2.4.4 Summary 59
2.5 Summary and Future Directions 60
2.6 Acknowledgements 61
2.7 References 62
3 Methods for Single-Cell Proteome Analysis 66
3.1 Abstract 66
3.2 Introduction 67
3.3 High-density Antibody-conjugated Microbead Arrays 69
3.3.1 Introduction 69
3.3.2 Experimental Methods 71
3.3.3 Results and Discussion 83
3.3.4 Summary 92
3.4 Integration of Microbead Arrays into PDMS Devices 93
3.4.1 Introduction 93
3.4.2 Experimental Methods 94
3.4.3 Results and Discussion 99
3.4.4 Summary 106
3.5 Summary and Future Directions 107
3.6 Acknowledgements 109
3.7 References 110
4 Methods for Single-Cell Gene Expression Profiling 117
4.1 Abstract 117
4.2 Introduction 118
4.3 Experimental Methods 120
4.4 Results and Discussion 130
4.5 Summary and Future Directions 147
4.6 Acknowledgements 149

4.7 References 149
5 Electric-field Directed Assembly of Active Enzyme-Nanoparticle Layers..... 153
5.1 Abstract 153
5.2 Introduction 154
5.3 Experimental Methods 156
5.4 Results and Discussion 160
5.5 Summary and Future Directions 170
5.6 Acknowledgements 171
5.7 References 172
6 Conclusions 176

LIST OF FIGURES

Figure 2-1. Fabrication of the pDEP electrodes..... 15

Figure 2-2. Layout of the microfluidic device..... 20

Figure 2-3. Capture of single cells by pDEP in a microfluidic device. 22

Figure 2-4. Bright-field images of the pDEP electrodes aligned and compartmentalized between two PDMS valves. 24

Figure 2-5. Capture and lysis of a single Jurkat cell. 26

Figure 2-6. Principle of the hydrodynamic cell trap. 29

Figure 2-7. Fabrication protocol for PDMS fluidic channel molds. 31

Figure 2-8. Photoresist mold for a single-cell hydrodynamic trapping and analysis device. 32

Figure 2-9. Assembled PDMS single-cell trapping and analysis device. 39

Figure 2-10. Plot of relative volumetric flows Q1/Q2 in the hydrodynamic traps relative to path 2 length..... 42

Figure 2-11. 2D-FEM model of fluid flow in basic hydrodynamic traps. 43

Figure 2-12. 2D-FEM model of fluid flow in hydrodynamic traps with side-channels. .. 44

Figure 2-13. 3D-FEM model of fluid flow in hydrodynamic traps. 45

Figure 2-14. FEM models of fluid flow from side-channels. 47

Figure 2-15. CAD design of a single-cell trapping and analysis device..... 48

Figure 2-16. Capture of single cells in various hydrodynamic trap designs..... 50

Figure 2-17. Isolation of single-cell trap compartments with PDMS valves..... 53

Figure 2-18. PDMS devices aligned to gold electrodes for electric-field cell lysis. 54

Figure 2-19. Cell lysis by electric field in hydrodynamic traps..... 55

Figure 2-20. Single unit of a single-cell capture and analysis device with side channels. 56

Figure 2-21. Single-cell capture and chemical lysis in secondary compartments. 57

Figure 3-1. Fabrication and assembly of the electrophoretic device. 75

Figure 3-2. Photographs of the assembled electrophoretic fluidic device. 76

Figure 3-3. Sandwich immunoassay on antibody-conjugated microbeads assembled via electrophoretic deposition. 80

Figure 3-4. Arrays of microwells and antibody-conjugated microbeads. 83

Figure 3-5. Spatial and fluorescence encoding of antibody-conjugated microbead arrays. 84

Figure 3-6. Standard curves for the sandwich immunoassays performed on antibody-conjugated microbead arrays. 86

Figure 3-7. Light transmission through an ITO film subjected to electrophoretic conditions. 88

Figure 3-8. Finite element analysis of the electric-field distribution within the microfabricated electrophoretic device. 90

Figure 3-9. Imaging of microbeads under and near a gold counter electrode line. 91

Figure 3-10. Substrate preparation and antibody-conjugated microbead assembly in the PDMS microfluidic devices. 99

Figure 3-11. Protective patterning of functionalized surfaces and magnetic bead assembly. 102

Figure 3-12. Protective patterning and assembly of antibody-conjugated microbeads in PDMS microchannels. 105

Figure 3-13. Incorporation of high-density antibody-microbead arrays into the single-cell analysis compartments. 108

Figure 4-1. Single cell mRNA capture and analysis methodology. 119

Figure 4-2. Protective patterning scheme for producing carboxyl surfaces in PDMS microchannels. 131

Figure 4-3. Functionalization scheme of substrate surfaces for capture of mRNA. 132

Figure 4-4. Verification of the polyT surface by Cy5-labeled 25mer-polyA oligo capture. 133

Figure 4-5. Single fluorescein-mRNA-150A molecule capture on functionalized surfaces in PDMS microchannels. 139

Figure 4-6. Capture kinetics of synthetic mRNA-150A in PDMS microchannels. 140

Figure 4-7. Single mRNA molecules from HeLa cells captured on functionalized surfaces in PDMS microchannels. 143

Figure 4-8. Capture kinetics of HeLa cell mRNA in PDMS microfluidic channels. 144

Figure 4-9. cDNA synthesis on polyT functionalized substrates. 146

Figure 5-1. Electric field directed assembly (layering) of biomolecule-NPs by different binding mechanisms. 155

Figure 5-2. Images of the 400 site platinum electrode CMOS microelectronic array and a cross-section of the structure. 156

Figure 5-3. Verification of the assembly of enzyme-nanoparticle layers. 161

Figure 5-4. Verification of assembly by ESEM. 162

Figure 5-5. Monitoring layer assembly by fluorescence. 164

Figure 5-6. ESEM images of enzyme-NP layering. 166

Figure 5-7. Retention of enzyme activity. 167

Figure 5-8. Proposed coupling of bi-enzyme NP layers. 169

ACKNOWLEDGEMENTS

First and foremost, I would like to thank my chair and primary adviser, Dr. Xiaohua Huang, for all the support and guidance that he has given me during my graduate career. He always offered me great insight and advice in my work while providing me the freedom and resources to explore my interests and grow not only as a scientist but also as a person. For all the opportunities and experiences he has given me, I am truly grateful.

Secondly, I would like to thank my co-chair, Dr. Michael J. Heller, for all his support and advice over the years. My first few years of Ph.D. work were in his lab and I thank him for all the opportunities he gave me early in my graduate work. I also greatly appreciate his unending support throughout the remaining years of my Ph.D. work.

I would like to thank Dr. Kristopher Barbee, who was a friend and important mentor to me when I first joined Dr. Huang's lab. I truly appreciate all that he taught me, from lab techniques to microfabrication to how to approach science. Together we had a fruitful collaboration and much of the knowledge I learned from him was instrumental towards my work in this dissertation.

I would like to thank Ho Suk Lee for his contributions and assistance in setting up systems for single-cell microfluidics; from solenoid valves to alignment systems to PDMS fabrication. I also thank him for his advice in setting up experiments, maintaining cell cultures, and providing insight for my microfluidic designs.

I would like to thank Matthew Walsh for his support and work in single-molecule detection and sequencing. His expertise and experimental support contributed significantly to my work in gene expression analysis from single cells.

I would like to thank Dr. Aric Joneja and Dr. Zhixia Liu for their advice and expertise in DNA and molecular biology techniques. Their help was paramount in setting up experiments and interpreting results for my work in gene expression analysis from single cells. I would like to thank Matt Chandrangsu for his range of advice and assistance. He provided me great help in microfabrication techniques, machining, surface chemistry, setting up an automated thermal block, and experimental ideas.

I would like to thank Dr. Eric Roller for his work and support in setting up and implementing automated systems for our imaging and fluidic systems. His work was significant in both imaging and analyzing results for high-density microbead arrays as well as TIRF detection of single molecules.

I would like to thank Dr. Nora Theilacker for her help and expertise in antibodies and antibody-conjugated microbeads. Her experience and understanding in these areas aided me significantly in my work on antibody-conjugated microbeads.

I would like to thank Robert Mifflin for his advice and knowledge in electrical systems. Additionally, his many resources helped me significantly in setting up a functional PDMS microfluidic chip fabrication and alignment workspace. I would like to thank Dr. Kwang-Seuk Ko for his expertise in chemistry. His advice in setting up conjugation reactions and surface chemistry was greatly appreciated.

I would like to thank Dr. Dietrich Dehlinger for his guidance and assistance in my early work in Dr. Heller's lab. His training and methods contributed significantly to my work on electric-field directed assembly. I would like to thank Dr. Jennifer Marciniak for her assistance and advice in cell culture. I also thank Ximin Chen for her assistance in maintaining cell cultures.

A portion of this work was conducted in the Nano3 cleanroom facility at UCSD. I would like to thank Ryan Anderson, Larry Grissom, Sean Parks, Dr. Xuekun Lu, and Dr. Bernd Fruhberger for their training and technical support. A portion of this work was conducted at the Nanotech Cleanroom Facility at UC Santa Barbara as well as at the Triangle National Lithography Center at NC State University. I would like to thank both facilities' staff for their assistance.

Chapter 2, in part, is a reprint of the material as it appears in: Hsiao, A.P., Barbee, K.D. and Huang, X. Microfluidic Device for the Capture and Isolation of Single Cells. *Proc. of SPIE,* 7759, 77590W, doi: 10.1117/12.861563, (2010). The dissertation author was the primary investigator and author of this publication.

Chapter 3, in part, is a reprint of the material as it appears in: Barbee, K.D., Hsiao, A.P., Roller, E.E., Huang, X. Multiplexed Protein Detection Using Antibody-conjugated Microbead Arrays in a Microfabricated Electrophoretic Device. *Lab on a Chip*, 10 (22), 3084-3093, (2010). The dissertation author was a co-investigator and co-author of this publication.

Chapter 5, in part, is a reprint of the material as it appears in: Hsiao, Alexander P. and Heller, Michael J., "Electric-field directed self-assembly of active enzyme-nanoparticle structures", *Journal of Biomedicine and Biotechnology,* 2012, ID 178487, 9 pages, doi:10.1155/2012/178487, (2012). Copyright 2012 Alexander P. Hsiao, Michael J. Heller, Hindawi Publishing Corp. The dissertation author was the primary investigator and author of this publication.

CURRICULUM VITA

Education

- Ph.D. in Bioengineering 2012
  University of California, San Diego
- M.S. in Bioengineering 2007
  University of California, San Diego
- B.S. in Bioengineering 2005
  University of California, Berkeley

Research Experience

University of California, San Diego

- **Genomics and Systems Biotechnology Lab** (Prof. Xiaohua Huang, 2008-2012)

1) Designed and fabricated an innovative microfluidic device for the capture, isolation, and lysis of single cells and *in situ* genomic or proteomic analysis, and 2) collaborated to develop breakthroughs in electric-field directed assembly of protein-conjugated microsphere arrays for sensitive high-throughput assays

- **Heller Research Lab** (Prof. Michael J. Heller, 2006-2008)

Devised novel methods for the electric-field directed self-assembly of active enzyme nanoparticle layers on microelectrode arrays in application to a manufacturing process to create scalable and affordable bio/chemical sensor arrays

University of California, Berkeley

- **Cell and Tissue Engineering Lab** (Prof. Song Li, 2004-2005)

Investigated the effects of fluid shear stress on the differentiation and proliferation of human mesenchymal stem cells for transformational cell therapies

Publications

Peer-reviewed journals

- Hsiao, A.P. and Heller, M.J., Electric Field Directed Self-Assembly of Active Enzyme-Nanoparticle Structures. *Journal of Biomedicine and Biotechnology*, 2012, Article ID 178487, doi:10.1155/2012/178487. (2012)
- Barbee, K.D., Hsiao, A.P., Roller, E.E., Huang, X. Multiplexed Protein Detection Using Antibody-conjugated Microbead Arrays in a Microfabricated Electrophoretic Device. *Lab on a Chip*, 10 (22), 3084-3093 (2010)
- Barbee, K.D., Hsiao, A.P., Heller, M.J. and Huang, X., Electric Field Directed Assembly of High-Density Microbead Arrays. *Lab on a Chip,* 9 (22), 3268-3274 (2009)

Conference proceedings

- Hsiao, A.P., Barbee, K.D. and Huang, X. Microfluidic Device for the Capture and Isolation of Single Cells. *Proc. of SPIE,* 7759, 77590W, doi: 10.1117/12.861563 (2010)

- Heller, M.J. and Hsiao, A.P., Multilayer BioDerivatized Nanoparticle Composites by Electric Field Directed Self-Assembly. *TechConnect World Conference: Nanotech 2010 Technical Proceedings* (2010)
- Barbee, K.D., Hsiao, A.P., Roller, E.E. and Huang, X.H., Multiplexed Protein Detection Using Antibody-Conjugated Microbead Arrays Assembled on a Microfabricated Electrophoretic Device. *TechConnect World Conference: Microtech 2010 Technical Proceedings.* (2010)
- Heller, M.J. and Hsiao, A.P. Electric Field Directed Fabrication of Multilayer BioNanoparticle Based Composites. *18th Intl. Conference on Composites/Nano Engineering.* (2010)

Presentations

Oral Presentations

- Hsiao, A.P., Barbee, K.D. and Huang, X., Microfluidic Device for Parallel Capture and Isolation of Single Cells, *SPIE Optics and Photonics: Nanoscience and Engineering 2010*, San Diego, CA (Invited)
- Hsiao, A.P., Barbee, K.D., Roller, E.E. and Huang, X., Multiplexed Protein Detection Using Antibody-Conjugated Microbead Arrays Assembled on a Microfabricated Electrophoretic Device, *TechConnect World Conference: Microtech 2010*, Anaheim, CA
- Heller, M.J. and Hsiao, A.P., Multilayer BioDerivatized Nanoparticle Composites by Electric Field Directed Self-Assembly, *TechConnect World Conference: Nanotech 2010*, Anaheim, CA

Poster Presentations

- Hsiao, A.P., Barbee, K.D., Huang, X., An Integrated Microfluidic Device for the Capture and Analysis of Single Cells, *Select Biosciences: Single Cell Analysis Summit 2010,* San Diego, CA
- Barbee, K.D.; Hsiao, A.P.; Heller, M.J. and Huang, X., Electric Field Directed Assembly of High-Density Microbead Arrays, *Lab on a Chip World Congress 2009*, San Francisco, CA
- Barbee, K.D.; Roller. E.E.; Hsiao, A.P.; Chaisson, M.; Heller, M.J.; Pevzner, P. and Huang, X., Single Molecule DNA Sequencing by Ligation, *NHGRI Sequencing Technology Meeting 2009*, San Diego, CA
- Hsiao, A.P., Dehlinger, D. and Heller, M.J., Directed Self-Assembly of Bio-Derivatized Nanoparticles into Micron Size Biosensor Devices, *TechConnect World Conference: Nanotech 2008,* Boston, MA
- Dehlinger, D., Sullivan, B., Krishnan, R., Lefkowitz, R., Hsiao, A. and Heller, M., Electric Field Directed Self-Assembly of Heterogeneous 3D Nanostructures, *NSF SINAM Workshop on Nanomanufacturing 2007,* Berkeley, CA

Patents and Disclosures

- Barbee, K. D.; Hsiao, A. P.; Huang, X. Microfabricated Devices for Electric Field Directed Assembly of DNA and Protein Arrays**.** *Provisional Patent Application.* 2010-279. *(2010)*

ABSTRACT OF THE DISSERTATION

METHODS AND DEVICES FOR COMPREHENSIVE MOLECULAR ANALYSIS OF SINGLE CELLS

by

Alexander Philip Hsiao

Doctor of Philosophy in Bioengineering

University of California, San Diego, 2012

Professor Xiaohua Huang, Chair

Professor Michael J. Heller, Co-Chair

Typical analytical methods for evaluating the protein and gene expression of cells rely on the molecular analysis of analytes from a large number of cells. These methods, however, do not reveal insight into the heterogeneous nature of cells and instead only provide average results of the bulk population. Moreover, these methods are insensitive to low copy number proteins or mRNA that may in fact play a significant role in a cell's phenotypic state. The ability to discern the true distributions of protein and gene

expression in a cell population will give rise to the effective identification of unique subpopulations. This allows for a deeper understanding of disease progression, molecular pathways, and cellular differentiation by revealing previously undetectable states of cells. Therefore, it is essential that technologies capable of isolating and comprehensively analyzing many single cells in parallel be developed.

In this dissertation, I present new methods and technologies for integrating the capture and isolation of single cells with comprehensive, quantitative on-chip molecular analysis within a single microfluidic platform. I first present the design, development, and function of polymethyldisiloxane (PDMS) microfluidic devices capable of trapping and fully isolating many single cells along a series of compartments. Additionally, I discuss various methods for trapping (dielectrophoretic or hydrodynamic) and lysing (electric-field or chemical) of the cells directly in individual, nanoliter-sized compartments. Subsequently, I present methods for the fabrication, assembly, and application of high-density antibody-conjugated microbead arrays for single-cell proteome analysis. I then discuss how such arrays can be integrated directly into the PDMS devices using a protective patterning scheme to overcome current challenges in producing patterned, modified surfaces in PDMS devices. I also present methods we have developed which could enable analysis of single-cell gene expression by directly sequencing the mRNA transcripts captured from each single cell on the device. Finally, I present my work on electric field-directed assembly of enzyme-nanoparticle layers for biosensor applications. Together, these methods and devices constitute key advancements towards the development of a technology capable of fully integrating single-cell capture and comprehensive molecular analysis.

1 INTRODUCTION

1.1 Single-cell Analysis

It is widely known that cells, even those in the same population, are heterogeneous in nature[1-5]. In efforts to better understand this heterogeneity, there has been increased interest in developing methods and technologies to analyze cells at the single-cell level[6-22]. This is necessary because common molecular analysis techniques, such as Western blotting or enzyme-linked immunosorbant assays (ELISA) for protein detection and microarrays or quantitative-polymerase-chain reaction (qPCR) for gene expression analysis, are bulk analysis methods which require thousands of cells and produce only an average result of the population. Repeated experimentation generates a distribution of this mean and not a definitive profile of the population. This is of extreme significance when seeking to understand areas such as stem cell differentiation, cancer cell development, and cell response to drugs or therapeutics where a small number of cells can have profound impacts. Currently, our understanding of cell development and disease progression is limited to studying significantly distinguishable cellular states. But to truly understand the mechanisms and pathways involved, we will need to be able to identify the subtle changes between each state and single-cell analysis can be the tool to accomplish this.

As a specific example, one only needs to look at our understanding of cancer. Tumor masses are composed of a heterogeneous mix of cells, including some normal,

non-cancerous cells and other cancer cells with a wide range differentiated cancer cell states[18, 19, 21, 23, 24]. Analysis of the whole tumor mass does not reveal precise information about the state of the cancer. Thus, single-cell analysis techniques are important in being able to identify the precise composition of cells in the tumor. This will ultimately allow for a more accurate determination of cancer stages and could lead to improved treatment. Another example is the debate over cancer stem cells. Cancer stem cells are presumed to be a very small population of cells which have the characteristics of stem cells, such as self-renewal, and the ability to differentiate into various cancer lineages[25]. Cancer stem cells may even be resistant to certain chemotherapeutics and responsible for deadly regeneration of tumors and metastases. However, this area of research is still hotly debated, partly due to the fact that cancer stem cells are so difficult to isolate and characterize[26-28]. Characterization of tumor masses and cancer cells by single-cell analysis could have great implications in shedding light on this debate. It would provide a definitive description of each tumor cell state and allow for identification of the presence and function of cancer stem cells.

1.2 Current Methods for Single-cell Analysis

Single-cell analysis has its roots since the first cells were observed under a microscope. Over time we have turned to other well established methods which include histological staining, *in situ* hybridization, micropipette, patch-clamp, mass cytometry, and flow cytometry[6, 7, 29-33]. Methods such as micropipette and patch clamp are extremely low throughput. Cell staining and *in situ* hybridization are only slightly better in

multiplexing ability, but still require cumbersome preparation procedures. The most popular of all these methods is flow cytometry and flow cytometry applications such as fluorescence-assisted cell sorting (FACS).

Flow cytometry is extremely high throughput in cell number and in recent years has increased in multiplexing ability[31]. Cells are tagged with fluorescent antibodies, for either membrane-bound or intracellular proteins, or with fluorescently labeled probes for mRNA or DNA detection. Multiple markers can be detected simultaneously as each cell's fluorescent signature is identified. Such methods have allowed for identification of cell subpopulations and are important in enrichment of samples or cell collection. Although flow cytometry has numerous advantages, it is not without its shortcomings. Preparation of samples still requires extensive time and labor. Additionally, the multiplexing ability of flow cytometry is limited by fluorescence spectral overlap. Moreover, tagging of targets is performed directly in whole cells and without being able to fully lyse or solubilize the cell some molecules may be difficult to probe. Also, cell secreted proteins are not able to be analyzed using flow cytometry methods. To obtain comprehensive molecular analysis, flow cytometry must then be coupled with sequencing or mass spectrometry which involves expensive equipment and cumbersome preparation protocols.

In recent years there has been a movement toward the development of microfluidic devices for single-cell analysis[8, 10, 17, 20, 22, 34-38]. Microfluidic devices have well known advantages including reduced sample and reagent volumes, lower cost, and ease of prototyping. Additionally, by incorporating standard microfabrication techniques, devices can be easily scaled-up for high-throughput applications. Specifically for single-

cell analysis, these devices have dimensions in the same range as those of mammalian cells, which allow for a more controlled and precise manipulation of single cells while maintaining reagent volumes to a minimum. Moreover, these devices can support live cell culturing, which add another dimension to the analysis of cell response to stimuli over time[9, 39]. In addition, microfluidic devices can be fabricated to incorporate multiple functionalities; including cell capture, lysis, reagent delivery, and analysis all on the same device.

1.3 Scope of the Dissertation

My work in this dissertation is focused on the development of a microfluidic device for comprehensive molecular analysis of single-cells. The device aims to serve as a platform on which many single cells can be captured and analyzed for their protein or gene expression. Design and development of the platform targets a few key challenges: first, the device must be able to capture many single cells and fully isolate each cell. This is to ensure that there is no cross-contamination between cells for downstream analysis. Secondly, the device should support cell lysis and release the cellular contents into small volume compartments. Lysis methods must be compatible with downstream analysis for either protein or mRNA. Compartment volumes are kept to a minimum to ensure a high concentration of analytes for increased sensitivity of detection. Finally, the device should integrate molecular analysis methods for highly multiplexed identification of cell contents.

In Chapter 2, I present the design and development of novel microfluidic devices for the capture, isolation, and lysis of many single cells. Polymethyldisiloxane (PDMS) microfluidic devices are designed and fabricated to capture single cells in series along microfluidic channels. Devices presented are capable of either dielectrophoretic (DEP) or hydrodynamic cell capture. Individual cells are then compartmentalized using a series of PDMS valves and then lysed directly in nanoliter sized compartments using either electric-field or chemical cell lysis. The microfluidic device serves as the foundation of the single-cell analysis device.

In Chapter 3, I present the development of technology to enable protein analysis from single-cells. Innovative methods for the fabrication and assembly of high-density antibody-conjugated microbead arrays are presented. Microfabrication techniques are used to pattern high-density arrays of wells in which antibody-conjugated microbeads are assembled into by electric-field. The antibody-microbead arrays showed sensitivity down to the picomolar range using test antigens. Additionally, I present methods on how the antibody-conjugated microbead arrays can be integrated directly into the single-cell capture compartments in the microfluidic devices.

In Chapter 4, I present the development of methods to enable gene expression profiling directly from single-cells in the microfluidic device. In particular, I address the significance of quantitative mRNA capture from each cell. Substrate surfaces are functionalized and protectively patterned to be compatible with PDMS device assembly. It is then shown that mRNA can be captured onto the substrate surface by hybridization of the 3'-polyA tails on each transcript to surface bound polyT. Results from mRNA

capture kinetics experiments show quantitative capture of mRNA at single-cell concentrations on the order of minutes.

In Chapter 5, I present my work on electric-field directed assembly of active enzyme-nanoparticle layers. Though this work was completed independently of the single-cell analysis device, it presents novel methods for which active biosensors can be rapidly assembled. Electric-fields are used to direct the assembly of enzymes and nanoparticles into higher order structures. It is shown that each layer can be assembled in seconds and alternate addressing of enzymes and nanoparticles can form as many as 39 layers. Additionally, enzyme activity is retained indicating that the electric-field assembly methods are both gentle and efficient.

1.4 References

1. L. Cai, N. Friedman and X. S. Xie, "Stochastic protein expression in individual cells at the single molecule level," *Nature*, vol. 440, no. 7082, pp. 358-62 (2006)

2. M. B. Elowitz, A. J. Levine, E. D. Siggia and P. S. Swain, "Stochastic gene expression in a single cell," *Science*, vol. 297, no. 5584, pp. 1183-6 (2002)

3. B. Huang, H. Wu, D. Bhaya, A. Grossman, S. Granier, B. K. Kobilka and R. N. Zare, "Counting low-copy number proteins in a single cell," *Science*, vol. 315, no. 5808, pp. 81-4 (2007)

4. J. M. Levsky and R. H. Singer, "Gene expression and the myth of the average cell," *Trends Cell Biol*, vol. 13, no. 1, pp. 4-6 (2003)

5. J. R. S. Newman, S. Ghaemmaghami, J. Ihmels, D. K. Breslow, M. Noble, J. L. DeRisi and J. S. Weissman, "Single-cell proteomic analysis of S. cerevisiae reveals the architecture of biological noise," *Nature*, vol. 441, no. 7095, pp. 840-846 (2006)

6. M. Batish, A. Raj and S. Tyagi, "Single molecule imaging of RNA in situ," *Methods Mol Biol*, vol. 714, no. pp. 3-13 (2011)

7. S. C. Bendall, E. F. Simonds, P. Qiu, A. D. Amir el, P. O. Krutzik, R. Finck, R. V. Bruggner, R. Melamed, A. Trejo, O. I. Ornatsky, R. S. Balderas, S. K. Plevritis, K. Sachs, D. Pe'er, S. D. Tanner and G. P. Nolan, "Single-cell mass cytometry of differential immune and drug responses across a human hematopoietic continuum," *Science*, vol. 332, no. 6030, pp. 687-96 (2011)

8. N. Bontoux, L. Dauphinot, T. Vitalis, V. Studer, Y. Chen, J. Rossier and M. C. Potier, "Integrating whole transcriptome assays on a lab-on-a-chip for single cell gene profiling," *Lab on a Chip*, vol. 8, no. 3, pp. 443-450 (2008)

9. D. Di Carlo, L. Y. Wu and L. P. Lee, "Dynamic single cell culture array," *Lab Chip*, vol. 6, no. 11, pp. 1445-9 (2006)

10. R. Fan, O. Vermesh, A. Srivastava, B. K. Yen, L. Qin, H. Ahmad, G. A. Kwong, C. C. Liu, J. Gould, L. Hood and J. R. Heath, "Integrated barcode chips for rapid, multiplexed analysis of proteins in microliter quantities of blood," *Nat Biotechnol*, vol. 26, no. 12, pp. 1373-8 (2008)

11. T. Kalisky and S. R. Quake, "Single-cell genomics," *Nat Methods*, vol. 8, no. 4, pp. 311-4 (2011)

12. K. Kurimoto, Y. Yabuta, Y. Ohinata and M. Saitou, "Global single-cell cDNA amplification to provide a template for representative high-density oligonucleotide microarray analysis," *Nature Protocols*, vol. 2, no. 3, pp. 739-752 (2007)

13. J. M. Levsky, S. M. Shenoy, R. C. Pezo and R. H. Singer, "Single-cell gene expression profiling," *Science*, vol. 297, no. 5582, pp. 836-40 (2002)

14. C. Ma, R. Fan, H. Ahmad, Q. Shi, B. Comin-Anduix, T. Chodon, R. C. Koya, C. C. Liu, G. A. Kwong, C. G. Radu, A. Ribas and J. R. Heath, "A clinical microchip for evaluation of single immune cells reveals high functional heterogeneity in phenotypically similar T cells," *Nat Med*, vol. 17, no. 6, pp. 738-43 (2011)

15. M. Saitou, Y. Yabuta and K. Kurimoto, "Single-cell cDNA high-density oligonucleotide microarray analysis: detection of individual cell types and properties in complex biological processes," *Reproductive Biomedicine Online*, vol. 16, no. 1, pp. 26-40 (2008)

16. A. Stahlberg and M. Bengtsson, "Single-cell gene expression profiling using reverse transcription quantitative real-time PCR," *Methods*, vol. 50, no. 4, pp. 282-8 (2010)

17. A. K. White, M. VanInsberghe, O. I. Petriv, M. Hamidi, D. Sikorski, M. A. Marra, J. Piret, S. Aparicio and C. L. Hansen, "High-throughput microfluidic single-cell RT-qPCR," *Proceedings of the National Academy of Sciences of the United States of America*, vol. 108, no. 34, pp. 13999-14004 (2011)

18. X. Xu, Y. Hou, X. Yin, L. Bao, A. Tang, L. Song, F. Li, S. Tsang, K. Wu, H. Wu, W. He, L. Zeng, M. Xing, R. Wu, H. Jiang, X. Liu, D. Cao, G. Guo, X. Hu, Y. Gui, Z. Li, W. Xie, X. Sun, M. Shi, Z. Cai, B. Wang, M. Zhong, J. Li, Z. Lu, N. Gu, X. Zhang, L. Goodman, L. Bolund, J. Wang, H. Yang, K. Kristiansen, M. Dean and Y. Li, "Single-cell exome sequencing reveals single-nucleotide mutation characteristics of a kidney tumor," *Cell*, vol. 148, no. 5, pp. 886-95 (2012)

19. Y. Hou, L. Song, P. Zhu, B. Zhang, Y. Tao, X. Xu, F. Li, K. Wu, J. Liang, D. Shao, H. Wu, X. Ye, C. Ye, R. Wu, M. Jian, Y. Chen, W. Xie, R. Zhang, L. Chen, X. Liu, X. Yao, H. Zheng, C. Yu, Q. Li, Z. Gong, M. Mao, X. Yang, L. Yang, J. Li, W. Wang, Z. Lu, N. Gu, G. Laurie, L. Bolund, K. Kristiansen, J. Wang, H. Yang, Y. Li and X. Zhang, "Single-cell exome sequencing and monoclonal evolution of a JAK2-negative myeloproliferative neoplasm," *Cell*, vol. 148, no. 5, pp. 873-85 (2012)

20. D. Di Carlo and L. P. Lee, "Dynamic single-cell analysis for quantitative biology," *Analytical Chemistry*, vol. 78, no. 23, pp. 7918-25 (2006)

21. N. Navin, J. Kendall, J. Troge, P. Andrews, L. Rodgers, J. McIndoo, K. Cook, A. Stepansky, D. Levy, D. Esposito, L. Muthuswamy, A. Krasnitz, W. R. McCombie, J. Hicks and M. Wigler, "Tumour evolution inferred by single-cell sequencing," *Nature*, vol. 472, no. 7341, pp. 90-4 (2011)

22. H. C. Fan, J. Wang, A. Potanina and S. R. Quake, "Whole-genome molecular haplotyping of single cells," *Nat Biotechnol*, vol. 29, no. 1, pp. 51-7 (2011)

23. N. Navin and J. Hicks, "Future medical applications of single-cell sequencing in cancer," *Genome Med*, vol. 3, no. 5, pp. 31 (2011)

24. A. Stahlberg, M. Kubista and P. Aman, "Single-cell gene-expression profiling and its potential diagnostic applications," *Expert Rev Mol Diagn*, vol. 11, no. 7, pp. 735-40 (2011)

25. C. T. Jordan, M. L. Guzman and M. Noble, "Cancer stem cells," *N Engl J Med*, vol. 355, no. 12, pp. 1253-61 (2006)

26. H. Clevers, "The cancer stem cell: premises, promises and challenges," *Nat Med*, vol. 17, no. 3, pp. 313-9 (2011)

27. P. Dirks, "Cancer stem cells: Invitation to a second round," *Nature*, vol. 466, no. 7302, pp. 40-1 (2010)

28. C. T. Jordan, "Cancer stem cells: controversial or just misunderstood?," *Cell Stem Cell*, vol. 4, no. 3, pp. 203-5 (2009)

29. E. M. Gaynor, M. L. Mirsky and H. A. Lewin, "Use of flow cytometry and RT-PCR for detecting gene expression by single cells," *Biotechniques*, vol. 21, no. 2, pp. 286-91 (1996)

30. P. O. Krutzik, J. M. Crane, M. R. Clutter and G. P. Nolan, "High-content single-cell drug screening with phosphospecific flow cytometry," *Nature Chemical Biology*, vol. 4, no. 2, pp. 132-142 (2008)

31. S. P. Perfetto, P. K. Chattopadhyay and M. Roederer, "Innovation - Seventeen-colour flow cytometry: unravelling the immune system," *Nature Reviews Immunology*, vol. 4, no. 8, pp. 648-U5 (2004)

32. E. Evans and A. Yeung, "Apparent viscosity and cortical tension of blood granulocytes determined by micropipet aspiration," *Biophysical Journal*, vol. 56, no. 1, pp. 151-60 (1989)

33. A. E. Spruce, A. Iwata, J. M. White and W. Almers, "Patch clamp studies of single cell-fusion events mediated by a viral fusion protein," *Nature*, vol. 342, no. 6249, pp. 555-8 (1989)

34. T. C. Chao and A. Ros, "Microfluidic single-cell analysis of intracellular compounds," *J R Soc Interface*, vol. 5 Suppl 2, no. pp. S139-50 (2008)

35. S. Koster, F. E. Angile, H. Duan, J. J. Agresti, A. Wintner, C. Schmitz, A. C. Rowat, C. A. Merten, D. Pisignano, A. D. Griffiths and D. A. Weitz, "Drop-based microfluidic devices for encapsulation of single cells," *Lab Chip*, vol. 8, no. 7, pp. 1110-5 (2008)

36. J. S. Marcus, W. F. Anderson and S. R. Quake, "Microfluidic single-cell mRNA isolation and analysis," *Analytical Chemistry*, vol. 78, no. 9, pp. 3084-9 (2006)

37. B. K. McKenna, J. G. Evans, M. C. Cheung and D. J. Ehrlich, "A parallel microfluidic flow cytometer for high-content screening," *Nat Methods*, vol. 8, no. 5, pp. 401-3 (2011)

38. A. R. Wheeler, W. R. Throndset, R. J. Whelan, A. M. Leach, R. N. Zare, Y. H. Liao, K. Farrell, I. D. Manger and A. Daridon, "Microfluidic device for single-cell analysis," *Analytical Chemistry*, vol. 75, no. 14, pp. 3581-6 (2003)

39. S. Kobel, A. Valero, J. Latt, P. Renaud and M. Lutolf, "Optimization of microfluidic single cell trapping for long-term on-chip culture," *Lab Chip*, vol. 10, no. 7, pp. 857-63 (2010)

2 MICROFLUIDIC DEVICES FOR SINGLE-CELL CAPTURE, ISOLATION, AND LYSIS

2.1 Abstract

The platform for single-cell analysis must first be able to capture, isolate, and lyse many single cells. The design, development, and function of polydimethylsiloxane (PDMS) based microfluidic devices capable of these functions are presented in this chapter. The device consists of three layers aligned and bonded together: a PDMS valve control layer, a PDMS flow channel layer, and a glass substrate layer. Together these layers form a device which is capable of trapping many single cells in individual, nanoliter-sized compartments where they are fully isolated from one another using pneumatically controlled PDMS valves. Cell lysis is then performed within the individual compartments. Moreover, the device design allows for the potential integration of numerous downstream *in situ* analysis techniques. Multiple device designs are demonstrated to show the functionality of both dielectrophoretic and hydrodynamic cell capture, along with both electrical and chemical cell lysis. Ultimately, the microfluidic device is the foundation of the single-cell analysis platform and provides for efficient capture and isolation of many single cells while also providing the versatility to integrate various capture, lysis, and downstream analysis techniques directly on-chip.

2.2 Introduction

Microfluidic devices offer many advantages for single-cell analysis. These devices, with dimensions in the same range as those of mammalian cells, allow for a more controlled and precise manipulation of single cells while maintaining reagent volumes to a minimum. In addition, microfluidic devices can be fabricated to incorporate multiple functions enabling cell capture, lysis, and analysis within the same device. Many microfluidic platforms have been demonstrated for the analysis of single cell contents[1-9]. These approaches, however, can only be used to interrogate a single cell or a few cells at a time. There is still a lack of devices that enable the capture and isolation of a large number of individual cells for high-throughput analyses. Other methods are available for parallel capture of a large number of cells by physical barriers[6, 10-13], pre-fabricated arrays[14-17], or electric fields[5, 18-20], but these methods do not fully isolate each cell from one another. This means they are not compatible with downstream processes, such as single-cell protein or gene expression analysis, where the cellular contents from each cell must be kept isolated after cell lysis. Many of these devices also do not integrate analysis on-chip, resulting in a significant risk of sample loss during extraction from the device for off-chip analyses. In addition, off-chip reactions (e.g. – cDNA synthesis, PCR, gel electrophoresis) no longer take advantage of the small volumes in microfluidic devices which could result in loss of detection sensitivity. One high-throughput, microfluidic method uses separation and analysis of single cells into emulsions[21-24]. While this technique is very good at fully isolating each cell and confining the cells to small volumes, the creation of uniform emulsions is not trivial. Moreover, there are often many

emulsions which contain either zero or multiple cells. Also, once formed, the emulsions should not be broken. This means all analysis reagents must be incorporated into the emulsion droplet and analysis may be limited a single step or reaction.

Ultimately, the device must satisfy a few key parameters: the efficient capture, isolation, and lysis of many single cells as wells as the ability to integrate multiplexed analysis of the intracellular molecules. In this chapter, I present the design and development of a microfluidic device that addresses these key issues. Devices are presented that are capable of trapping many single-cells in series from a cell suspension using either dielectrophoretic or hydrodynamic capture. Single-cells are then fully isolated into nanoliter-sized compartments using a system of PDMS valves. Each cell is then lysed directly in their respective compartments using either electric-field or chemical lysis. These small volume compartments provide a high-molecule concentration volume and large surface area for incorporation of downstream on-chip analysis methods.

2.3 Dielectrophoretic Cell Capture Devices

2.3.1 Introduction

Methods are described for trapping and isolating cells in series using dielectrophoretic cell capture and a system of PDMS channels and valves. Individual cells are captured by positive dielectrophoresis (pDEP) atop a microfabricated electrode pattern along the length of a fluidic channel. The cells are then isolated from one another using pneumatically actuated PDMS valves into compartments where they can then be lysed open by an electric field.

Dielectrophoresis (DEP) is the phenomena in which particles, including cells, can be manipulated in a non-uniform electric field[25]. The equation for the dielectrophoretic force on a spherical particle (cell) is as follows:

$$F = 2\pi\varepsilon_m R^3 \,\mathrm{Re}[CM(\omega)\nabla E^2(r,\omega)] \qquad j = \sqrt{-1}$$

$$CM = \frac{\varepsilon'_p - \varepsilon'_m}{\varepsilon'_p + 2\varepsilon'_m} \qquad \varepsilon = \text{electrical permittivity}$$

$$\varepsilon' = \varepsilon + \sigma / j\omega \qquad \sigma = \text{conductivity}$$

m = media; p = particle (cell)

The direction of cell movement is dependent upon the particle's relative permittivity to the medium, as shown by the Claussius-Mosotti factor (CM). Additionally, this factor is a function of the solution conductivity and the frequency. This means that by changing the solution and/or changing the applied frequency, different DEP responses can be attained. In pDEP, the particles move towards the high field gradient whereas in negative dielectrophoresis (nDEP), the particles move towards the low field gradient.

Both pDEP and nDEP have been shown to be capable of manipulating and trapping single cells with minimal perturbation to the cell itself[5, 7, 18, 19]. pDEP, having a stronger holding force, is employed in this device to capture individual cells from the solution flow using microfabricated electrodes. Each captured cell is compartmentalized by actuating a series of PDMS valves to close off the fluidic channels. Monolithic PDMS valves are commonly used in microfluidic devices and are derived from work by Unger *et al*[26]. Similar valves have been used in many microfluidic devices for cell capture and formation of low volume compartments[1, 2, 27, 28]. Following cell compartmentalization, the same electrodes are then used to lyse the cells by applying an electric field[3, 7, 29]. Finally, our device will support downstream parallel molecular analysis of single cells within the

compartments, such as protein analysis using pre-fabricated antibody arrays and digital gene expression analysis by direct single molecule sequencing[30].

2.3.2 Experimental Methods

Fabrication of pDEP capture electrodes on glass wafers

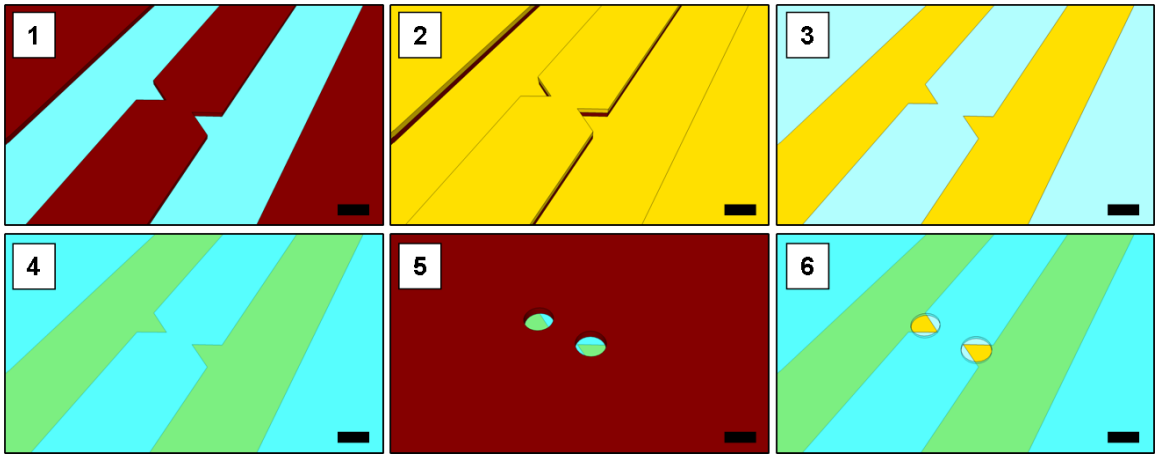

Figure 2-1. Fabrication of the pDEP electrodes. (1) Cleaned wafers are coated with photoresist and electrodes are patterned by photolithography. (2) Ti/Au/Ti is deposited by sputter coating. (3) Metal lift-off is performed, leaving behind patterned electrodes. (4) A 250 nm silicon dioxide layer is deposited by PECVD. (5) 10 µm holes are patterned in the photoresist over the electrode tips. (6) 10 µm holes are wet-etched into the silicon dioxide and the photoresist stripped. Scale bars are 10 µm in each panel.

As illustrated in Figure 2-1, the electrodes were fabricated using standard photolithography and metal lift-off techniques on 100 mm diameter glass wafers. The glass wafers were first cleaned by immersion in a 2% Micro-90 (Cole Parmer) detergent solution for 15 minutes in an ultrasonic water bath. Following a rinse in dH_2O, the wafers were further cleaned by immersion in a 1:1:5 mixture of dH_2O: 30% NH_4OH: 30% H_2O_2 (RCA1), and then in a 3:1 mixture of 98% H_2SO_4: 30% H_2O_2 (Piranha) for 1 hour in each solution at 80 °C. (Caution: Piranha solution is extremely dangerous and should be

handled with care.) The glass substrates were thoroughly rinsed with dH_2O and stored in dH_2O until use.

Following a dehydration bake at 120 °C for 10 minutes, the cleaned glass wafers were coated with hexamethyldisilazane (HMDS) (Shin-Etsu MicroSi, Inc.) and then spun dry at 4000 rpm on a spin-coater. A layer of Shipley Microposit LOL1000 (Rohm & Haas Electronic Materials, LLC) was then applied onto the wafer to a thickness of approximately 100 nm by spin-coating at 3000 rpm. After a soft-bake of the LOL1000 for 5 minutes at 150-170 °C, a positive photoresist, Shipley Microposit S1818 (Rohm & Haas Electronic Materials, LLC), is spin-coated at 4000 rpm onto the wafer and soft-baked at 115°C for 90 seconds. The wafer was then exposed on a Karl Suss MA6 mask aligner in vacuum contact mode for 22 seconds using a transparency mask (Fineline Imaging). The photoresist was then developed in MF-321 (Rohm & Haas Electronic Materials, LLC) for 1 minute, rinsed in dH_2O and dried with nitrogen gas. Resist descum was then performed by exposing the patterned wafers to oxygen plasma in a Technics PEII-B plasma system at 100 W RF and 3×10^{-3} Torr O_2. Films of titanium, gold, and titanium were subsequently deposited onto the patterned photoresist by sputter coating on a Denton Discovery 18 sputter system. Titanium was deposited at 150 W for 1 minute, followed by gold at 200 W for 4 minutes, and titanium again at 150 W for 30 seconds at 3.0×10^{-3} Torr Ar at 36-38 sccm. Metal liftoff was then performed by immersing the wafers in Microposit 1165 (Rohm & Haas Electronic Materials, LLC) remover with ultrasonication in a 70 °C water bath for 1 hour. The wafers were rinsed with isopropyl alcohol and dried with nitrogen gas.

Silicon dioxide was then deposited onto the patterned electrodes in an Oxford Plasmalab plasma-enhanced chemical vapor deposition (PECVD) system to a height of ~250 nm. Deposition was conducted at 350 °C and 20 W RF using 710 sccm N_2O and 170 sccm SiH_4 at 1 Torr. The silicon dioxide layer was then coated with a layer of HMDS by spin-coating at 4000 rpm and then with a layer of positive photoresist, Shipley Megaposit SPR 220-3.0 (Rohm & Haas Electronic Materials, LLC), by spin-coating at 3000 rpm. Following a soft-bake at 115 °C for 90 seconds, the wafer was exposed again on the MA6 mask aligner in vacuum contact mode for 15 seconds using a transparency mask (CAD/Art Services). A post-exposure bake was performed at 115 °C for 90 seconds and the photoresist was then developed in MF-24A developer (Rohm & Haas Electronic Materials, LLC) for 1 minute. The wafer was then rinsed in dH_2O and dried with nitrogen gas. The remaining photoresist was hard-baked at 120 °C for 10 minutes. Finally, the pattern was etched through the silicon dioxide to expose the underlying electrodes by immersing the entire wafer in a buffered oxide etch (6:1 of 40% NH_4F: 49% HF) for 135 seconds and then thoroughly rinsing in dH_2O. The photoresist was then stripped by immersing the wafer in acetone and then isopropyl alcohol. Finally, the wafer was rinsed with dH_2O and dried with nitrogen gas.

Fabrication of molds for PDMS fluidic and valve control channels

The molds for PDMS fluidic and valve control channels were fabricated using the procedure developed by Unger *et al*[26]. 100 mm silicon wafers (MEMC Electronic Materials, Inc.) were first cleaned thoroughly by immersing in Piranha solution at 85 °C for 10 minutes, followed by a rinse in dH_2O, a one minute immersion in buffered oxide

etch (6:1 of 40% NH_4F: 49% HF), and then another rinse in dH_2O. The wafer was then dehydrated by baking at 120 °C for 15 minutes.

For the fluidic channel molds, the wafer was primed with HMDS by spin-coating at 4000 rpm. A positive photoresist, Shipley Microposit SPR 220-7.0 (Rohm & Haas Electronic Materials, LLC), was then spin-coated onto the wafers at 3000 rpm for 1 minute. After the wafer was soft-baked at 115 °C for 2 minutes, an additional layer of SPR 220-7.0 was spin-coated onto the wafer and soft-baked at 115 °C for 3 minutes. The photoresist was then exposed using a transparency photomask (CAD/Art Services) on a Quintel contact aligner for 75 seconds at 10 mW/cm^2. The wafers were then stored overnight at ambient conditions. The wafer was then developed in MF-24A for 10-40 minutes, rinsed thoroughly in dH_2O, and dried with nitrogen gas. To achieve rounded features needed for the fluidic channels, the photoresist was reflowed by heating at 120 °C for 20 minutes.

For the valve control channel molds, a negative tone photoresist, SU 8-25 (MicroChem Corp.), was spin-coated onto the wafers at 1100 rpm after a dehydration bake. The photoresist was then soft-baked at 65 °C for 5 minutes and then 95 °C for 15 minutes. The wafer was then exposed to the valve pattern using a transparency photomask on a Quintel contact aligner for 20 seconds. The photoresist was then baked at 65 °C for 1 minute and 95 °C for 4 minutes, and then developed in SU-8 developer (MicroChem Corp.) for 6 minutes. The wafer was then rinsed in isopropyl alcohol and dried with nitrogen gas. Finally, the photoresist was hard-baked at 130 °C for 15 minutes to enhance the mold strength and durability.

All mold height and profile measurements were performed with a Dektak 150 surface profiler (Veeco Instruments, Inc.) using 5 mg of force and a 12.5 μm diameter probe tip.

Fabrication of PDMS fluidic channels and valves

Prior to use, the molds for the fluidic channel and valve control layer were passivated with tridecafluoro-1, 1, 2, 2-tetrahydrooctyl-1-trichlorosilane (Pfaltz and Bauer) by vapor deposition. The wafer-molds were placed for 1 hr in a vacuum chamber containing 15 μL of the fluorosilane solution in a small aluminum dish. 10 g of a 20:1 mixture (part A: part B = 20:1) of Sylgard 184 (Dow Corning) and 40 g of a 5:1 mixture were prepared and degassed in a vacuum chamber. The 5:1 PDMS mixture was poured onto the valve control channels mold in a polycarbonate dish and degassed again in a vacuum chamber. The 20:1 PDMS mixture was spin-coated onto the fluidic channel layer mold at 1150 rpm. Both PDMS layers were then allowed to cure at 65 °C for 30 minutes. The PDMS valve control layer was then peeled off the mold and holes were punched through the layer for fluid connections with a 0.5 mm diameter punch (Ted Pella, Inc.). The PDMS valve control layer was aligned to the fluidic channel layer and the two were bonded together by heating at 80 °C for 1 hour. The two layers were then peeled off the fluidic channel mold together and holes were punched for the fluid channel inlets and outlets.

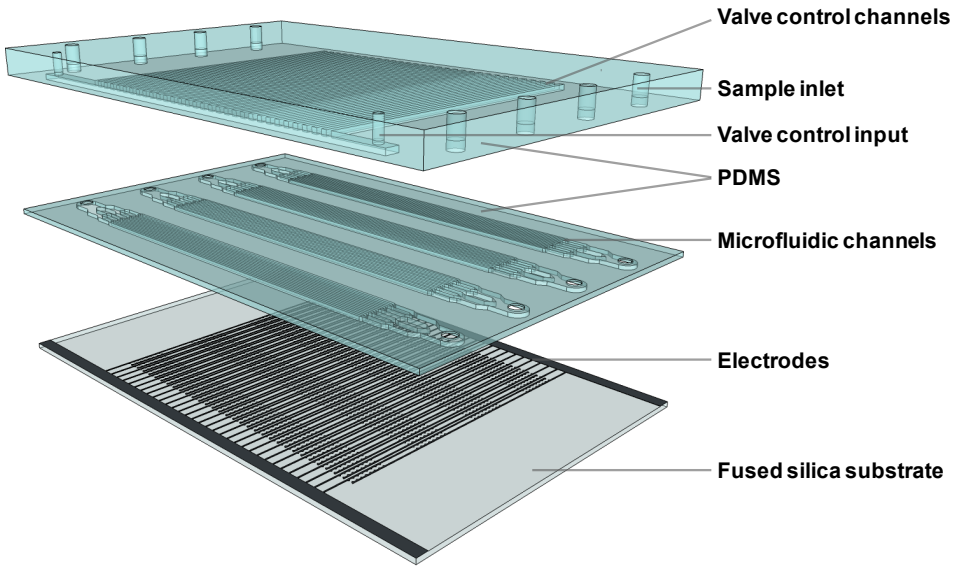

Figure 2-2. Layout of the microfluidic device. PDMS fluidic and valve control channel layers are assembled atop microfabricated electrodes.

Device Integration

The final device, as depicted in Figure 2-2, consists of the glass substrate with the microfabricated pDEP electrodes and the PDMS fluidic and valve control channels. To bond the PDMS fluidic channel and valve control layers to the electrode substrate, the two were first exposed for 3 minutes in an UV ozone plasma cleaner. The two were then aligned to one another and bonded together by curing at 80 °C for 1 hour. Fluid connections were made by stainless-steel metal tubes (New England Small Tube, 0.032 OD x 0.025 ID, 0.500" length, type 304, cut, deburred, passivated) inserted into the pre-punched holes in the PDMS. Perfluoroalkoxy (PFA) tubing (0.03 ID x 0.0625 OD, Upchurch Scientific) was slipped onto these metal tubes. Solution delivery and valve control was performed by pressure-driven flow and an in-line valve and regulator (AirTrol, Inc.). Electrical connections to the pDEP electrodes were made using wires soldered to copper tape placed on the fabricated bus bars.

Cell Culture

Jurkat T-lymphocytes (E6.1, Sigma-Aldrich Co.) were maintained in standard culture conditions (37 °C and 5% CO_2) in RPMI 1640 medium (Mediatech, Inc.) supplemented with 10% fetal bovine serum (Mediatech, Inc.) and 1% penicillin/streptomycin (MP Biomedicals). For experiments using fluorescent detection, the cells were stained with a green fluorescent membrane dye, Vybrant DiO (Invitrogen, Inc.), according to the manufacturer's protocols. The cells were then exchanged into a low salt isotonic buffer (0.01x PBS with 300 mM sucrose, 150 μS/cm) at ~1-5 x 10^5 cells/mL for loading into the microfluidic device.

Cell Capture and Lysis

The cell capture procedure is illustrated in Figure 2-3. The microfluidic device was mounted on a stage adaptor onto an inverted epifluorescence microscope (Axiovert 200M, Carl Zeiss, Inc.). Cells suspended in the low salt isotonic buffer were loaded into the microfluidic channels by pressure-driven flow at 0.3-0.7 psi while an AC sine at 10 V_{pp} and 10 MHz was applied using an Agilent 32220 function generator to the electrodes to capture the cells. After the cells were captured by pDEP, one on each electrode pair, the air pressure to the cell loading lines was shut off and re-directed to the PDMS valve control lines. The PDMS valves were then actuated by increasing the pressure to ~10 psi to compartmentalize the cells. Cell lysis was then performed by increasing the voltage to the electrode pairs to 20 V_{pp} and decreasing the frequency from 10 MHz to 10 kHz. Bright-field and fluorescence images were captured using a 10x/0.3 NA Plan-NeoFluar objective (Carl Zeiss), a 1-megapixel EMCCD camera (iXon plus 885, Andor

Technology, PLC) and a fast wavelength-switching light source with a 300 W xenon arc lamp (Lambda DG-5, Sutter Instrument Co.). The green fluorescence of the Vybrant DiO was imaged in the FITC channel using Solis software (Andor Technology, PLC).

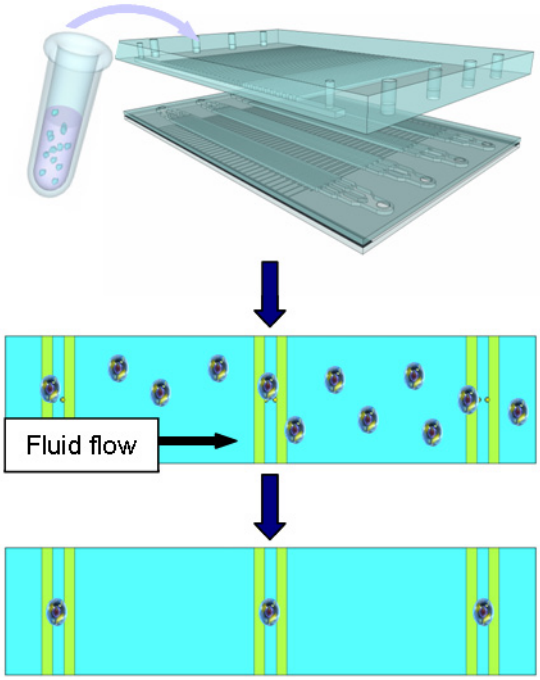

Figure 2-3. Capture of single cells by pDEP in a microfluidic device. Cells are loaded into the microfluidic channels and captured at the electrodes by positive dielectrophoresis. After the excess cells were washed away, the PDMS valves are actuated to compartmentalize the individual cells.

2.3.3 Results and Discussion

Electrode design considerations

In designing the capture electrodes, we chose to use pDEP, as opposed to nDEP, for cell capture. Initially, we attempted an nDEP electrode format similar to that used by Mittal *et al*[5]. We found that the nDEP holding forces were too weak to hold the cells effectively during washing. In addition, cell lysis requires the presence of very high field strengths more compatible with a pDEP design. Our pDEP electrodes consist of pairs of

inter-digitated, 25 μm wide electrodes with triangular tips 10 μm apart from one another (Figure 2-1). These triangular tips provide regions of high field strength for pDEP to be more effective. To ensure that the dielectrophoretic field is exposed only at the tips, the electrodes are overlaid with an insulating layer of silicon dioxide and 10 μm holes are etched directly over the triangular electrode tips. The dielectric insulation layer prevents the cells from being attracted to the electrode across the entire length of the electrode in the fluidic channel and allows for each cell to be trapped in a small area large enough for only one cell. The silicon dioxide layer also prevents the cell from directly contacting the gold electrodes where it could be damaged or lysed during the cell capture process. Moreover, the silicon dioxide serves as a uniform surface to which the PDMS fluid and valve channel layers can be strongly and easily bonded.

Our current design, although capable of capturing, isolating, and lysing single cells, can be improved. The 250 μm wide channels are considerably larger than a typical mammalian cell in suspension, which are only tens of micrometers in diameter. The electrodes for cell capture are centered in the channel, leaving much of the channel open. This results in inefficient cell capture since the cells are distributed across the channel width and only those passing directly over the capture electrodes can be trapped. In addition, the surface of the substrate is prone to non-specific binding of the cells. Improvement could be made by focusing the cells towards the capture electrodes, possibly by electric fields, sheath flow, or physical mechanisms. The non-specific binding of cells to the channel surfaces can be mitigated by chemical modification of the substrate surface or by applying repulsive electric fields.

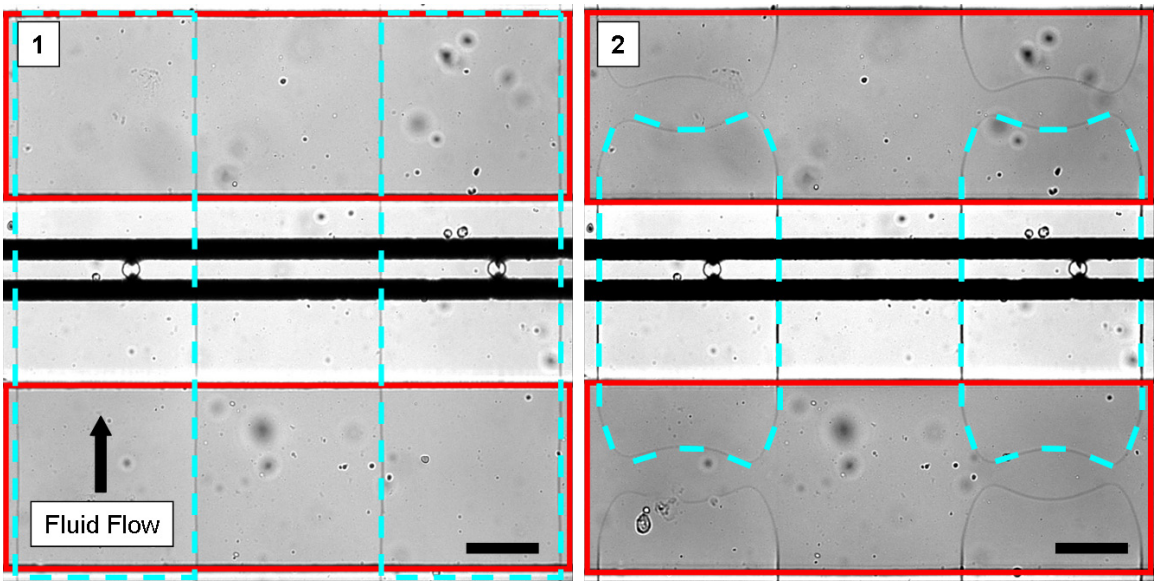

Figure 2-4. Bright-field images of the pDEP electrodes aligned and compartmentalized between two PDMS valves. (1) The PDMS valve control lines (red) are orthogonal to the fluid channels (blue) and the pDEP capture electrodes are aligned between two valve control lines. (2) The pDEP capture electrode regions are isolated into compartments by closing the valves at pressures of 10-15 psi. Scale bars are 50 µm.

Compartmentalization by PDMS valves

Our channel and valve design is based on that described by Unger *et al.*[26]. In brief, it consists of a two-layer PDMS structure with the top layer comprised of valve control channels orthogonal to the fluidic channels patterned into the bottom layer. Figure 2-4 shows a bright-field image of the fluidic and valve control channels on an assembled device. Actuation of the upper valve control layer causes the membrane of PDMS between the layers to expand and pinch down, thereby closing off the fluid channels (Figure 2-4.2). Thus, the valves are only located at the intersection of the valve control lines and the fluidic channels. The fluid channel height of 25 µm was designed to give ample room to accommodate a single Jurkat cell used in our experiments. To maintain the necessary 10:1 aspect ratio for proper valve closure, the width of the channels is 250

μm. The valve control lines are designed at the same pitch as the pDEP electrodes, 500 μm, so that each pair of pDEP capture electrodes can be valved off into isolated compartments. When a pressure of 10-15 psi was applied to the fluid filled valve control lines the fluidic channels could visibly be seen to pinch off (Figure 2-4.2) and the pDEP capture electrodes were isolated into individual compartments. The fluidic channels were patterned to be ~30 mm in length, with 60 capture compartments of ~1 nL volume along the length of each channel. Each compartment's volume can be decreased if the valve and electrode pitch is decreased or the fluidic channel is made narrower. A smaller volume in the compartment results in a higher concentration of intracellular molecules upon cell lysis, enabling more efficient *in situ* analyses of these molecules. Additionally, decreasing the pitch of the electrodes and valves or higher density channels will greatly improve the throughput capabilities of the device.

Single cell capture and lysis

As shown in Figure 2-5, we have demonstrated the ability to capture single cells by pDEP using an AC sine wave at 10 V_{pp} and 10 MHz. The cells were captured from a fluid suspension driven through the channels with a pressure of 0.3-0.7 psi. Since the exposed triangular tips of each electrode pair are only 10 μm apart, only one cell can be captured by each electrode pair. After the cells were captured and compartmentalized, they were lysed using an electric field by increasing the voltage to 20 V_{pp} across the electrode pair. The resultant electric field has a maximum strength of 2 MV/m at the tips of the electrodes.

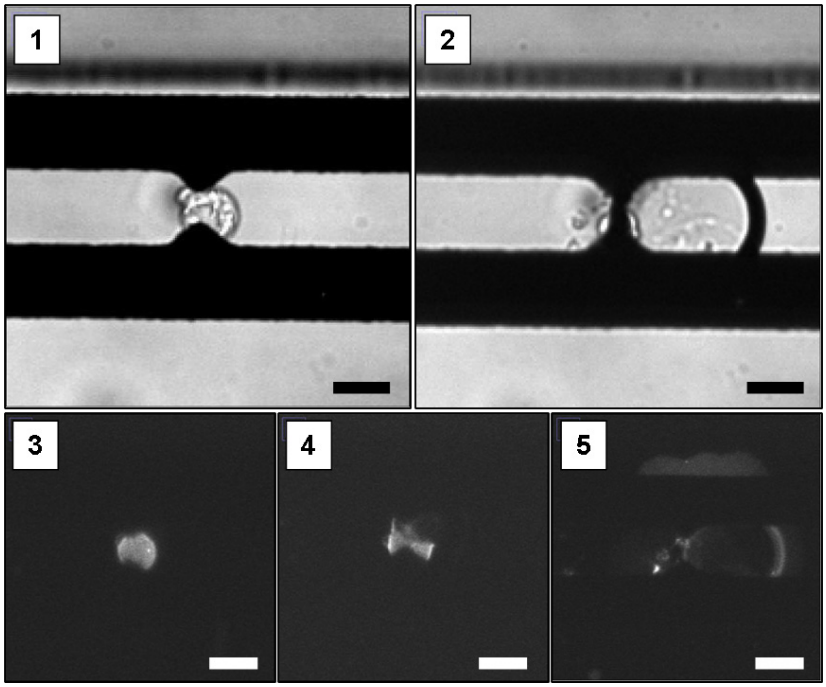

Figure 2-5. Capture and lysis of a single Jurkat cell. (1) Bright field image of the capture of a single Jurkat cell by pDEP using an AC sine wave with 10 V_{pp} at 10 MHz. (2) Bright field image of the same compartment after lysis of the cell. A bubble is seen due to hydrolysis at 1 kHz and 20 V_{pp}. (3) Fluorescent image in the FITC channel corresponding to the same cell in panel 1. (4) A single cell being lysed by applying an AC field with 20 V_{pp} at10 kHz. (5) Fluorescent image of the compartment corresponding to panel 2 after cell lysis. All scale bars are 20 μm.

To visualize the deformation of the cellular membrane during this process, the cells were pre-stained with a fluorescent membrane dye. It could clearly be observed that the membrane deformed when the frequency of the applied AC sine wave was reduced to 10 kHz. The reduction of the frequency to 1 kHz or below, however, resulted in visible hydrolysis and bubble formation, which may be detrimental to the device and the cellular components, such as nucleic acids and proteins. In addition, the formation of the bubbles could compromise the sealing of the valves and Joule heating could undesirably raise the temperature of the fluid. Future optimization of the conditions for cell capture and lysis conditions will be required to avoid these effects.

2.3.4 Summary

We have developed a microfluidic device which incorporates electrodes for single cell capture and lysis by electric field and PDMS channels and valves for the isolation and compartmentalization of the individual captured cells. We have shown that single cells suspended in a low salt isotonic buffer can be captured by pDEP with the triangular-tipped electrode pairs 10 μm apart using an AC sine wave of 10 V_{pp} at 10 MHz. After the individual captured cells were isolated by using pressure-actuated PDMS valves, the cells were subsequently lysed open by increasing the AC field to 20 V_{pp} and decreasing the frequency to 10 kHz. The compartmentalization will allow for downstream molecular analysis of cellular components within each cell without interference from other cells. By incorporating *in situ* analysis techniques, such as pre-fabricated antibody arrays within each compartment, this device may enable single cell proteomic or gene expression studies. This device provides a platform for parallel capture, isolation and molecular analysis of thousands of cells in a highly parallel manner directly within a single integrated microfluidic device.

2.4 Hydrodynamic Cell Capture Devices

2.4.1 Introduction

Single-cell dielectrophoretic trapping methods were successful, but not without their limitations. DEP is a relatively weak force and efficient cell capture from the cell suspension was a challenge. More specifically, the electrodes were designed to trap only a single cell and thus it was required that they were fabricated close to one another, only

10 μm apart, to ensure that multiple cells could not be captured. The channel width was 250 μm wide, about 10 times the capture region, making the probability of capturing randomly dispersed cells more challenging. Designs used to constrict the channel to help focus the cells over the trap sites also increase the flow velocity and make it even more difficult to trap and hold a cell in the flow. Additionally, the low conductivity solutions needed for efficient pDEP capture of the cells is not the ideal buffer for cells. In efforts to develop a more efficient means of cell capture I turned to the design and development of hydrodynamic cell capture devices.

Hydrodynamic trapping of cells has been successfully integrated into many microfluidic platforms[10-13, 31-34]. This type of trapping uses the geometry of the microfluidic channels to direct the fluid flow and therefore guide single cells into specific trapping sites. Because the flow in microfluidic devices is laminar, the flow is predictable and can be easily manipulated by altering channel dimensions. Hydrodynamic trapping allows for extremely efficient cell capture because the flow path is explicitly defined by the channel geometry. This allows for extremely rapid cell capture with high efficiency. The principles of the hydrodynamic single-cell traps are illustrated in Figure 2-6[32].

As seen in Figure 2-6A, the hydrodynamic traps work on the principle of relative fluidic resistance in the channels. Each trapping compartment has two fluid paths, path 1 and path 2, with a trap site located in path 1. Each path has a specific fluidic resistance, R1 and R2, which are functions of the channel dimensions. As the bulk flow enters it will split into two, Q1 and Q2. At an empty trap site, as seen in Figure 2-6B, $R1 < R2$ which means more of the flow will enter into path 1 and a cell is more likely to be carried into the trap site. Once the trap site is occupied, as in Figure 2-6C, the resistance R1 increases

because the cell blocks the fluid and subsequently the path of least resistance changes to path 2. The bulk of the flow now directs around the longer path 2 and extra cells will divert to this path where they can proceed to the next trap in series.

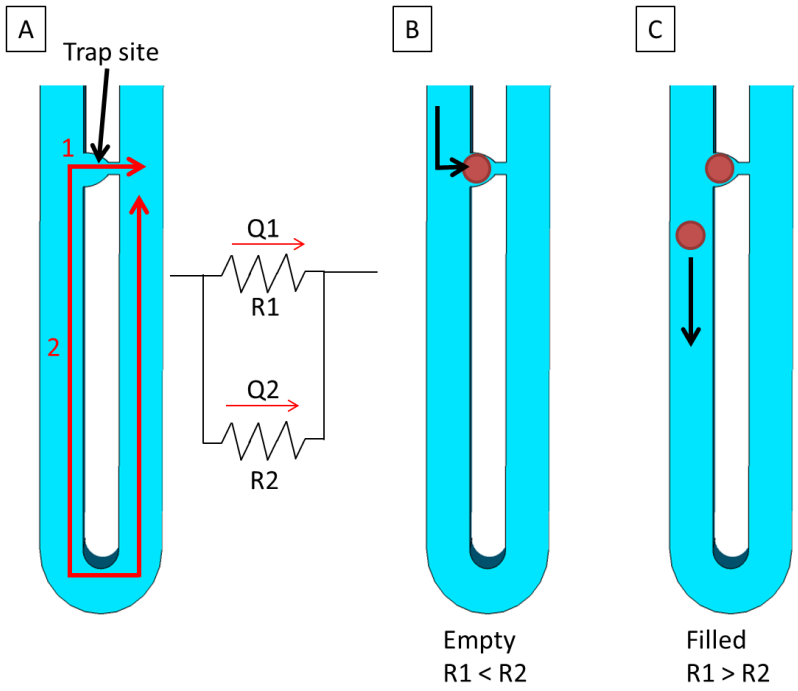

Figure 2-6. Principle of the hydrodynamic cell trap. (A) The hydrodynamic cell trap consists of two possible flow paths, path 1 and path 2. Path 1 is a small and narrow and directs to the cell trap site. Path 2 is a long and wide path meant for redirection of extra cells. The channels function on the principle of relative fluidic resistance with the principal flow being split into two flows, Q1 and Q2. (B) When the resistance through path 1, R1, is smaller than the resistance through path 2, R2, such as when the trap site is empty, then Q1 > Q2 and a single cell flows into the trap site. (C) A trapped cell blocks flow and increases R1 greater than R2 such that subsequent cells redirect to path 2 and move to the next trap in series.

In this chapter I will present the design, fabrication, and application of the single-cell hydrodynamic traps. Contrary to other current devices for hydrodynamic cell capture, I present the integration of the PDMS valves for full isolation of each trapped cell along a series of hydrodynamic traps. Additionally, I discuss variations in design which can be used to successfully trap cells and further show integration with either electric-field or

chemical lysis. Ultimately, I present a complex single-cell trapping and analysis design which is capable of trapping and lysing many single cells while incorporating area for integration of downstream *in situ* analysis techniques.

2.4.2 Experimental Methods

Finite element modeling of flow in fluidic channels and channel designs

Fluidic channel designs were created using a computer-assisted drawing (AutoCAD, Autodesk) tool. Finite element method (FEM) modeling of the fluidic channel designs was then performed in COMSOL Multiphysics (COMSOL AB) using either 2D or 3D mode incorporating laminar flow physics. Channel walls were defined as solid boundaries with selected walls indicated as inlets or outlets. Outlets were defined to have a pressure of zero, while inlet conditions were set to a fixed flow velocity. All boundaries were set with a no-slip condition. The internal channel domain was set to the properties of water and had a zero-velocity initial value. Trapped cells were drawn as circles (2D) or spheres (3D) which were subtracted from the water domain. Images were generated showing the fluid velocity and flow streamlines in each model.

PDMS channel layer mold fabrication

For the PDMS fluidic channel molds, fabrication requires a two-step method, as outlined in Figure 2-7. The valve features are patterned first and need to be rounded; thus they are fabricated with a positive photoresist, SPR 220-7.0. This is followed by patterning of the remaining fluidic features using a negative photoresist, SU 8-2025. The

following methods ensure proper compatibility between the two types of photoresist processing steps.

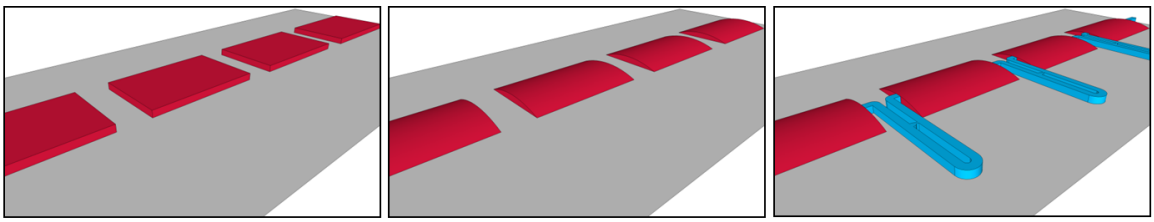

Figure 2-7. Fabrication protocol for PDMS fluidic channel molds. (1) The channel layer mold requires first patterning the valve features in a positive-tone photoresist, SPR 220-7.0. (2) Following, a reflow and hard-bake step is performed to round the valve features as well as make the photoresist resistant to the solvents used in SU8 negative-tone photoresist processing. (3) The final channel features are then aligned and patterned in SU 8-2025.

First, 100 mm silicon wafers (University Wafer, test grade) were cleaned. This was done either by: 1) immersing in Piranha solution at 85 °C for 10 minutes, followed by rinsing in dH_2O and a one minute immersion in buffered oxide etch (6:1 of 40% NH_4F: 49% HF) followed by another rinse in dH_2O, or 2) rinsing in acetone, methanol, and then isopropanol before drying by nitrogen air. The wafer was then dehydrated by baking at 120 °C for 15 minutes. The wafer was then primed with HMDS by spin-coating at 4000 rpm. A positive photoresist, Shipley Microposit SPR 220-7.0 (Rohm & Haas Electronic Materials, LLC), was spin-coated onto the wafers at 500 rpm for 10 seconds, then at 625 rpm for 45 seconds, and finally at 5000 rpm for 0.3 seconds at maximum acceleration to help remove edge-bead. The wafer was let to sit for 3 minutes; if the wafer is transferred to the hotplate for soft-bake too quickly then the photoresist will retract from the wafer edges resulting in non-uniform thickness. The photoresist was then soft-baked at 115 °C for 7 minutes and removed slowly off of the hotplate to reduce the chance of fractures forming in the cooling photoresist. The wafer was then allowed to sit at room temperature

for at least one hour. Next, the photoresist was exposed using a transparency photomask (FineLine Imaging) on a Karl Suss MA6 contact aligner for 130 seconds at 11 mW/cm^2 in hard contact mode. The photomask for the flow channel layer included feature dimensions that were expanded to 100.42% to accommodate for PDMS shrinking during curing. The wafers were then stored overnight at ambient conditions. The photoresist was developed in MF-24A (Microposit) for 5-10 minutes until clean, rinsed thoroughly in dH_2O, and dried with nitrogen gas. To achieve rounded features needed for the valving regions, the photoresist was reflowed by heating at 200 °C for 120 minutes. This served also to hard-bake the SPR photoresist making it resistant to solvents and compatible with the remaining processing steps.

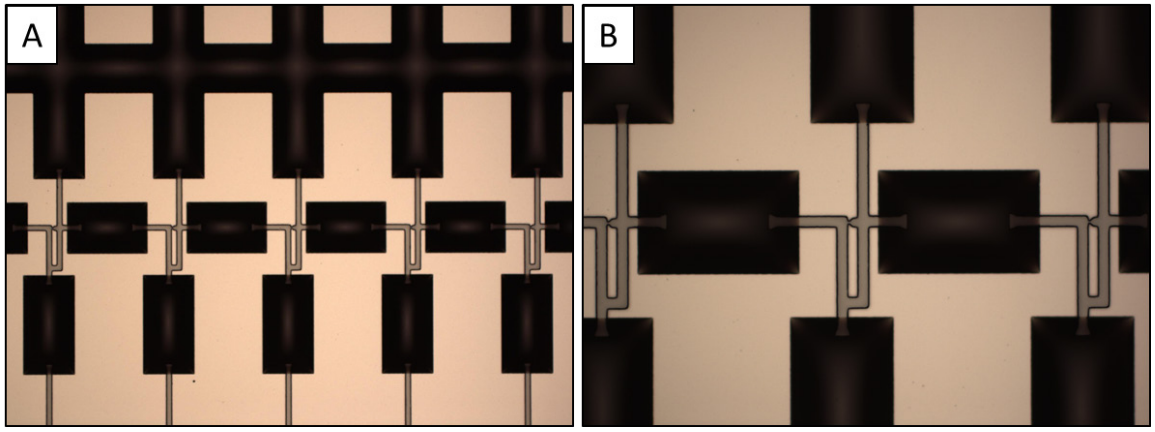

Figure 2-8. Photoresist mold for a single-cell hydrodynamic trapping and analysis device. Molds are fabricated using a SPR-220 positive-tone photoresist (black) and a SU-8 negative-tone photoresist (grey) aligned to one another. Micrographs shown at (A) 5x and (B) 10x magnification depict the narrow SU-8 features for cell capture and the wide SPR-220 features for valving.

The remaining fluidic features were patterned as follows. SU 8-2025 (MicroChem Corp.) was spin-coated at 3100 rpm onto the wafers and then soft-baked at 65 °C for 3 minutes and 95 °C for 5 minutes. The photoresist was patterned with a transparency

photomask on a Karl Suss MA6 for 13 seconds at 11 mW/cm^2. The photoresist was then post-exposure baked at 65 °C for 2 minutes and 95 °C for 5 minutes, and developed in SU-8 developer (MicroChem Corp.) for 4 minutes. The wafer was rinsed in isopropyl alcohol and dried with nitrogen gas. Finally, the photoresist was hard-baked at 150 °C for 10 minutes to enhance the mold strength and durability. An example of the final mold features on a wafer is shown in Figure 2-8.

Mold height and profile measurements were performed with a Dektak 150 surface profilometer (Veeco Instruments, Inc.) using 5 mg of force and a 12.5 μm diameter probe tip to verify the proper feature heights. Images of the molds were acquired using a Zeiss Axio Imager upright microscope.

PDMS valve layer mold fabrication

For the valve control channel molds, a negative tone photoresist, SU 8-2050 (MicroChem Corp.), was spin-coated onto clean, dehydrated wafers at 4000 rpm. The photoresist was then soft-baked at 65 °C for 3 minutes and 95 °C for 6 minutes. The wafer was then exposed to the valve pattern using a transparency photomask on a Karl Suss MA6 contact aligner for 15 seconds. The photomask for the valve control layers included features that were expanded to 101.67% to accommodate for PDMS shrinking during curing. The photoresist was post-exposure baked at 65 °C for 1 minute and 95 °C for 6 minutes, and then developed in SU-8 developer (MicroChem Corp.) for 4 minutes. Next, the wafer was rinsed in isopropyl alcohol and dried with nitrogen gas. Finally, the photoresist was hard-baked at 150 °C for 10 minutes to enhance the mold strength and durability.

Mold height and profile measurements were performed with a Dektak 150 surface profilometer (Veeco Instruments, Inc.) using 5 mg of force and a 12.5 μm diameter probe tip to verify the proper feature heights. Images of the molds were acquired using a Zeiss Axio Imager upright microscope.

Fabrication of electrodes on glass coverslips for electric-field cell lysis

Electrodes were fabricated using standard photolithography and metal lift-off techniques on 50 x 50 mm, #1.5 thickness glass coverslips (Fisher). The glass coverslips were first cleaned by immersion in a 2% Micro-90 (Cole Parmer) detergent solution for 15 minutes in an ultrasonic water bath. Following a rinse in dH_2O, the coverslips were further cleaned by immersion in a 1:1:5 mixture of dH_2O: 30% NH_4OH: 30% H_2O_2 (RCA1), and then in a 3:1 mixture of 98% H_2SO_4: 30% H_2O_2 (Piranha) for 1 hour in each solution at 80 °C. (Caution: Piranha solution is extremely dangerous and should be handled with care.) The glass substrates were thoroughly rinsed with dH_2O and stored in dH_2O until use.

Following a dehydration bake at 120 °C for 10 minutes, the cleaned glass was coated with NR9-1500 negative photoresist (Futurrex, Inc.) by spin-coating at 4000 rpm. The photoresist was then soft-baked at 150 °C for 1 minute. The coverslip was then exposed on a Karl Suss MA6 mask aligner in hard contact mode for 81.8 seconds at 11 mW/cm^2 through a transparency mask. Following exposure, a post-bake was performed at 100 °C for 1 minute. The photoresist was then developed in RD6 Developer (Futurrex, Inc.) by immersion for 6 seconds, rinsed in dH_2O and dried with nitrogen gas. A photoresist descum was performed using a Technics PEII-B with O_2 plasma at 300 mTorr

and 100 W power for 3 minutes. Films of titanium, gold, and titanium were subsequently deposited onto the patterned photoresist by sputter coating in a Denton Discovery 18 sputter system. Titanium was deposited at 150 W for 1 minute, followed by gold at 200 W for 4 minutes, and titanium again at 150 W for 30 seconds at 3.0×10^{-3} Torr Ar at 36-38 sccm. Metal liftoff was then performed by immersing the coverslips in Resist Remover RR2 (Futurrex, Inc.) remover with ultrasonication in a 70 °C water bath for 30 minutes. The coverslips were rinsed with dH_2O and dried with nitrogen gas.

Silicon dioxide was then deposited onto the patterned electrodes in an Oxford Plasmalab plasma-enhanced chemical vapor deposition (PECVD) system to a height of ~600 nm. Deposition was conducted at 350 °C and 20 W RF using 710 sccm N_2O and 170 sccm SiH_4 at 1 Torr. The silicon dioxide layer was then coated with a layer of HMDS by spin-coating at 4000 rpm and then with a layer of positive photoresist, Shipley S1813 (Rohm & Haas Electronic Materials, LLC), by spin-coating at 5000 rpm. Following a soft-bake at 115 °C for 60 seconds, the wafer was exposed on a MA6 mask aligner in hard contact mode for 34.1 seconds at 11 mW/cm^2 using a transparency mask (FineLine Imaging). The photoresist was then developed in MF-321 developer (Rohm & Haas Electronic Materials, LLC) for 70 seconds. The coverslip was then rinsed in dH_2O and dried with nitrogen gas. Finally, the pattern was etched through the silicon dioxide to expose the underlying electrodes by reactive-ion etching (RIE) in an Oxford P80 system using the SiO_2 etch recipe. Briefly, this used Ar and CHF_3 gas at 200 W power and 35 mTorr pressure for 15 minutes. Following, a brief O_2 plasma-etch was performed as recommended at 200 W and 100 mTorr for 30 seconds. The photoresist was then stripped

by immersing the wafer in 1165 remover. Finally, the coverslip was rinsed with dH_2O and dried with nitrogen gas.

PDMS device fabrication and assembly

Prior to use, the molds for the fluidic channel and valve control layer were passivated with tridecafluoro-1, 1, 2, 2-tetrahydrooctyl-1-trichlorosilane (Pfaltz and Bauer) by vapor deposition. The wafer-molds were placed for 1 hr in a vacuum chamber containing 15 μL of the fluorosilane solution in a small aluminum dish. 10 g of a 20:1 mixture (part A: part B = 20:1) of Sylgard 184 (Dow Corning) and 40 g of a 5:1 mixture were prepared and degassed in a vacuum chamber. The 5:1 PDMS mixture was poured onto the valve control channels mold in a polycarbonate dish and degassed again in a vacuum dessicator. The 20:1 PDMS mixture was poured onto the flow channel mold and degassed, then spin-coated at 1150 rpm for 1 minute. Both PDMS layers were then allowed to cure at 65˚C for 30 minutes. The PDMS valve control layer was then peeled off its mold and holes were punched for fluidic connections with a 0.75 mm diameter punch (Ted Pella, Inc.). The PDMS valve control layer was aligned to the fluidic channel layer using a custom alignment system and the two were bonded together by heating at 75 °C for a minimum of 1 hour. The two layers were then peeled off the fluidic channel mold together and holes were punched for the fluidic channel inlets and outlets.

For devices without electrodes, the bottom substrate of the device was a cleaned 50 x 50 mm, #1.5 thickness glass coverslip (Fisher). The coverslip was cleaned by rinsing with a 2% solution of Micro-90 detergent and then sonicating for 5 minutes each in a solution of acetone and methanol. Finally, the slides were rinsed thoroughly in dH_2O and

dried with an argon air gun. The glass coverslip and the PDMS channels and valves were then activated by exposing to oxygen-plasma in a UV-ozone (UVO) cleaner (Jelight Company, Inc.) for 4 minutes. The PDMS was then quickly placed onto the glass coverslip while carefully avoiding trapping of bubbles. The PDMS was then permanently bonded to the glass coverslip by curing in a convection oven at 75-80 °C for a minimum of 2 hours.

For devices with fabricated electrodes, the PDMS channels and valves piece was carefully aligned to the patterned alignment marks on the glass substrate surface following UVO activation. Coarse alignment was done with a 1-3 mm gap using a 10x magnification on a custom alignment device. A few drops of methanol were then placed onto the glass substrate and the PDMS brought into contact. The methanol serves as a lubrication layer so that the PDMS may be manipulated on the glass substrate without bonding. This allowed for fine alignment using 50x magnification. Once features were aligned the methanol was let to evaporate and then the device moved into a convection oven at 75-80 ˚C for a minimum of 2 hours to complete the bonding.

Cell culture and preparation

Human HeLa cells were maintained in standard culture conditions (37 °C and 5% CO_2) in Dulbecco's Modified Eagle's Medium (DMEM; Mediatech, Inc.) supplemented with 10% fetal bovine serum (Mediatech, Inc.) and 1% penicillin/streptomycin (MP Biomedicals). Cells were passaged as needed. In preparation for experiments, cells were detached from culture flask surfaces using 0.25% trypsin/EDTA (Mediatech, Inc.) and re-suspended in full DMEM. Cells were then centrifuged at 1000 rpm for 6 minutes and

exchanged into phosphate-buffered saline (PBS) without calcium or magnesium ions (Mediatech, Inc.). The lack of divalent cations helped prevent cell aggregation. Cells used in experiments were diluted to a concentration of 0.5-1 million cells per mL.

Device preparation

Before performing experiments, the PDMS microfluidic device required preparation. Devices with electrodes were wired by affixing conductive copper tape to fabricated gold bus lines on the substrates. Wires were soldered to the copper tape on one end and to mini-banana plugs on the other which interfaced with an Agilent 32220 function generator.

The valve lines were filled with a food coloring solution to allow visual confirmation of valve control channel filling. Because PDMS is gas permeable, a fluid must be used to fill these lines. Food coloring solution was loaded into perfluoroalkoxyalkane (PFA) Teflon tubing (ID: 0.03”, OD: 1/16”, Idex Health and Science) using a syringe. The tubing was then interfaced to the PDMS valve control channel inlets using small stainless steel tubing (OD: 0.032”, type 304 WD, stainless steel, New England Small Tube) that inserts snuggly into the PFA tubing on one end and into the pre-punched inlet in the PDMS on the other end. This was done for each of the valve control lines on the device. The PFA tubing was removed from the syringe and the device was mounted onto the microscope stage where it was interfaced to a custom built system of solenoid valves and regulators. The valve control lines were filled by applying 1.5-2 psi of pressure. Figure 2-9 shows an example of an assembled device, but with the fluidic channel lines also filled with a red-dye solution to allow for ease of visualization.

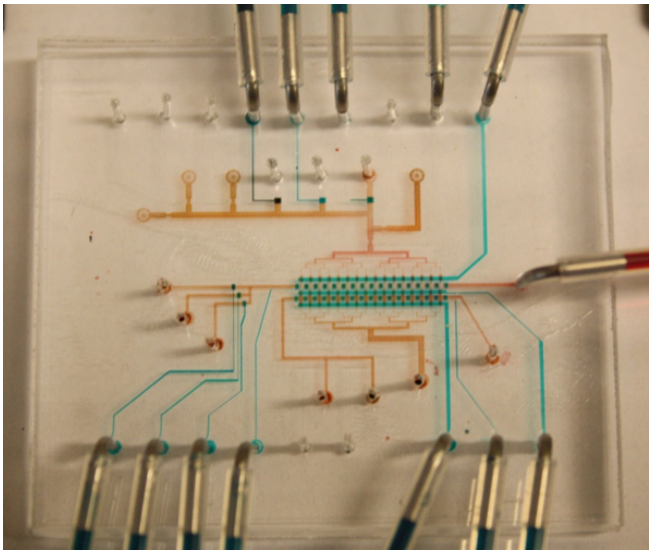

Figure 2-9. Assembled PDMS single-cell trapping and analysis device. A PDMS device consisting of the valve control layer and fluidic channel layer bonded to a glass substrate. Valve control lines are filled with blue food coloring solution. The fluidic channel lines are filled with a red food coloring solution for visual effect. The device shown has dimensions of 36 mm x 32 mm.

After valve control lines are fully filled, the main cell capture channel is blocked with a protein-free blocking buffer (PBS-T20, Pierce-Thermo Fisher Scientific). Devices with secondary compartments and side channels had all side channel valves and inter-secondary compartments closed. First, to prevent blocking buffer from entering any side channel inlets that are on the device, valves to these channels are closed by applying 5-10 psi of pressure. The blocking buffer is loaded into a syringe and connected to a fluid channel inlet using PFA tubing and a steel pin. The blocking buffer is then continuously injected using an infusion syringe pump (Chemyx) at a flow rate of 15-25 μL/hr for 30-60 minutes to block the channel surfaces and minimize non-specific cell adhesion.

Cell capture and lysis

Just prior to cell capture experiments, the main fluidic channel was flushed with PBS to wash away the blocking buffer. Cells were then loaded into a 1 mL glass syringe (Hamilton) and injected into the device at 1-10 μL per hour using an infusion syringe pump. The cells were observed to monitor flow rate and cell capture. After cells had been captured the cell infusion was stopped and the inter-compartment valve line was pressurized to fully seal off each individual trap compartment. This was done by manually increasing the pressure slowly from 1 psi up to 12-15 psi when valve closure was visually confirmed.

For devices with electrodes for electrical cell lysis, cell lysis was performed by applying an AC sine wave to the electrode pairs at 20 V_{pp} and 10 MHz and decreasing the frequency to 10 kHz. In devices incorporating secondary compartments and side channels, the side inlet channel was filled with lysis buffer (500 mM LiCl, 1% LiDS, 10 mM EDTA, 5 mM DTT, 100 mM Tris-HCl pH 7.5; derived from Dynal mRNA Direct kit, Invitrogen) using 1 psi of air pressure. Side channel valves were then opened around the main capture compartment to allow the lysis buffer to flow in and push the cell into the secondary compartments. All inter-trap valves remained closed to ensure no mixing between compartments. During the cell capture and lysis procedures, bright-field images were acquired using a 10x/0.3 NA Plan-NeoFluar objective (Carl Zeiss) and a 1-megapixel EMCCD camera (iXon plus 885, Andor Technology, PLC) using Andor Solis software.

2.4.3 Results and Discussion

Modeling results and calculations

To aid in the design of the single-cell hydrodynamic traps, initial calculations were performed and FEM models generated. As stated earlier, in order to ensure trapping of the single-cells, the empty trap requires the flow Q1 to be greater than the flow Q2; that is the volumetric flow through the empty trap site should be greater than the volumetric flow around path 2. This ratio of Q1/Q2 is defined as:

$$\frac{Q1}{Q2} = \left(\frac{C_2(\alpha_2)}{C_1(\alpha_1)}\right) * \left(\frac{L_2}{L_1}\right) * \left(\frac{P_2}{P_1}\right)^2 * \left(\frac{A_1}{A_2}\right)^3$$

$$C(\alpha) = 96(1 - 1.3553\alpha + 1.9467\alpha^2 - 1.7012\alpha^3 + 0.9564\alpha^4 - 0.2537\alpha^5);\ \alpha = W/H$$

L = length; A = cross-sectional area = (W*H); P = perimeter = 2(W+H)

This equation shows that there is no velocity or pressure gradient term. This indicates that the flow distribution is purely a function of the channel dimensions and is independent of the inlet flow rate.

In designing the channels, a limiting factor regarding the dimensions was the size of a cell. Using HeLa cells with a mean diameter of about 15-20 μm, the channel height and width was set to 25 μm. Additionally, the path 1 dimensions were made to be L1 = 8 μm and W1 = 8 μm such that the captured cell would not be able to easily squeeze through the trap. Given this set of dimensions, a calculation of Q1/Q2 along with the capture efficiency, defined by Q1/(Q1+Q2) was calculated and results are shown in Figure 2-10.

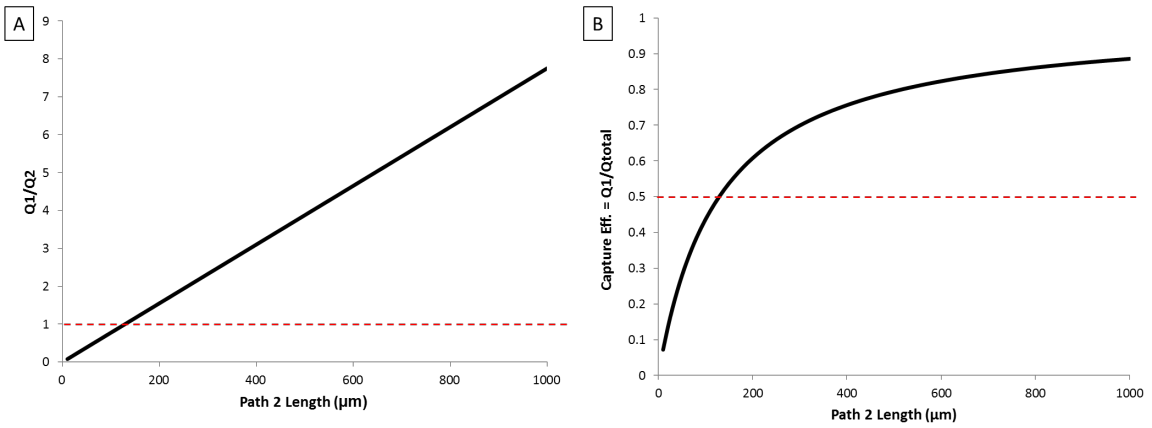

Figure 2-10. Plot of relative volumetric flows Q1/Q2 in the hydrodynamic traps relative to path 2 length. Data is generated with L1 = 8 µm, W1 = W2 = 25 µm, H = 25 µm, and L2 varied. (A) Plot showing the ratio of Q1/Q2. For trapping to occur, Q1/Q2 > 1; this cutoff is indicated by the red dashed-line. This occurs with L2 at a minimum of 130 µm. (B) Plot of capture efficiency as defined by the ratio of Q1/(Q1+Q2). For capture, greater than 50% of the flow must go to Q1; this cutoff occurs at L2 of 130 µm.

As seen in Figure 2-10A, with the dimensions for path 1 and the width and height of path 2 set, Q1/Q2 follows a linear relationship as L2 increases in length. A Q1/Q2 ratio greater than 1 is required to capture cells and this is seen when the length of path 2 surpasses 130 µm in length. Similarly, Figure 2-10B shows the capture efficiency as defined by the relative proportion of volumetric flow directed to path 1. A cut-off of 0.5 is required to achieve single-cell capture and this occurs when L2 is 130 µm in length. The calculations show that in order for the hydrodynamic traps to work, the length of path 2 must be at least 130 µm in length. The efficiency of the trap increases as the length of path 2 increases as well. But to achieve even 90% efficiency, path 2 would need to be 1 mm in length. This is not practical in microfluidic platforms for downstream analysis where it is advantageous to have smaller compartment volumes which require a shorter path 2 length. From previous works, it was determined that a Q1/Q2 ratio of 2-3 is sufficient for efficient capture and trap filling[12, 32]. This would require my designs to have

a path 2 length of at least 260 µm, which would still keep the overall compartment volume small. Final devices were designed to have a Q1/Q2 ratio of about 3.

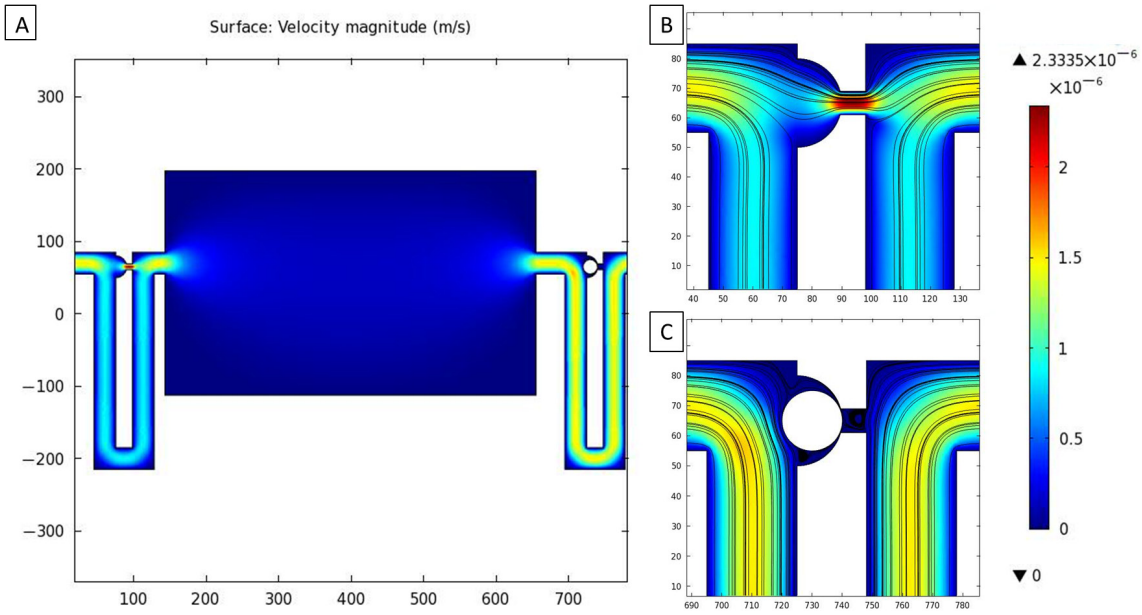

Figure 2-11. 2D-FEM model of fluid flow in basic hydrodynamic traps. Plots show fluid velocity magnitude and velocity streamlines. (A) Velocity profile is shown through two trap sites and a valve region between. (B) With a closer look at an empty trap site, many streamlines are directed into the trap site resulting in a lower velocity through path 2. (C) When a cell is trapped, these streamlines redirect to path 2. Inlet velocity was set at 1 µm/s. In this design W1 = L1 = 8 µm, W2 = H = 30 µm, L2 = 578 µm, resulting in a Q1/Q2 = 2.65 and an expected capture efficiency of 72.6%.

FEM modeling was performed using COMSOL to visualize and validate various channel designs. Figure 2-11 shows the results of a 2D model of a pair of hydrodynamic traps, one empty and one with a trapped cell. Figure 2-11A clearly shows the difference in flow velocity through each of the trap sites, with a much higher fluid velocity around path 2 when a trap is occupied. This is seen in Figure 2-11B and C as well. An in-close view shows fluid streamlines directed into the trap site at an empty trap. When the trap is filled with a cell, these streamlines redirect to path 2 and the flow velocity increases in path 2 indicating that the volumetric flow has now increased in path 2.

A similar 2D model is generated for a different, more complex channel design, as shown in Figure 2-12. In this design side-channels are added to each compartment. These side-channels provide orthogonal fluid flow of buffers or reagents to each cell after inter-compartment valves are closed. During cell capture the side-channels are closed off such that in the model they can be simplified as solid boundaries. Despite these changes in geometry the 2D model still shows the same fluid flow velocity profiles, as seen in Figure 2-12A. Additionally, Figure 2-12B and C show the same diversion of streamlines from path 1 to path 2 once a cell is captured in the trap site.

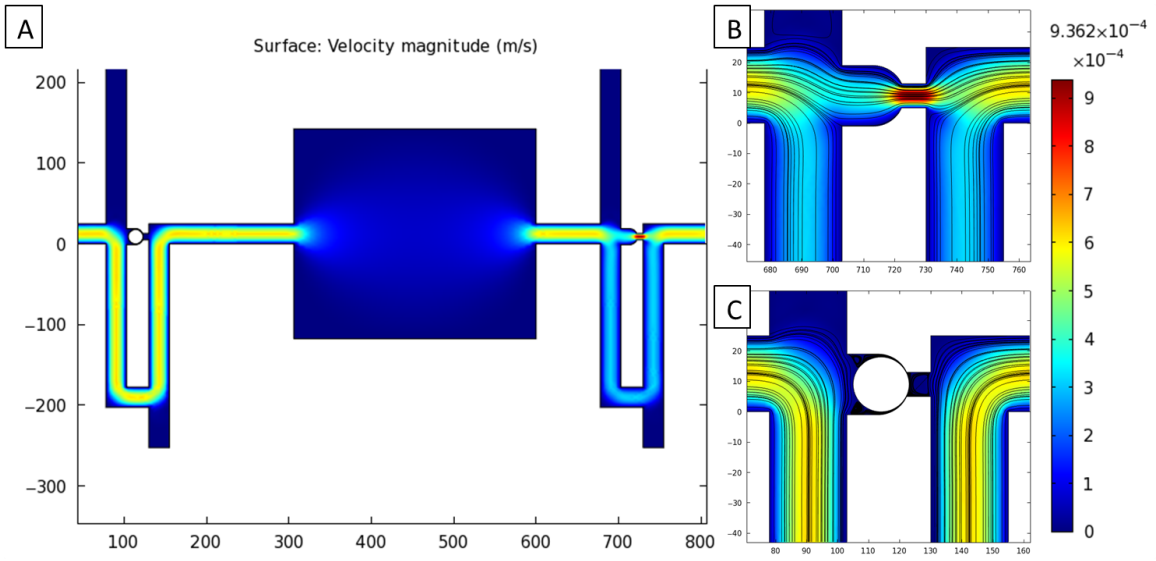

Figure 2-12. 2D-FEM model of fluid flow in hydrodynamic traps with side-channels. Plots show fluid velocity magnitude and velocity streamlines. (A) Velocity profile is shown through two trap sites and a valve region between. (B) With a closer look at an empty trap site, many streamlines are directed into the trap site resulting in a lower velocity through path 2. (C) When a cell is trapped, these streamlines redirect to path 2. Models were generated with laminar flow properties. Inlet velocity was set at 440 µm/s (1 µL/hr flow rate). In this design L2 = 430 µm, resulting in a Q1/Q2 = 3.33 and an expected capture efficiency of 77%.

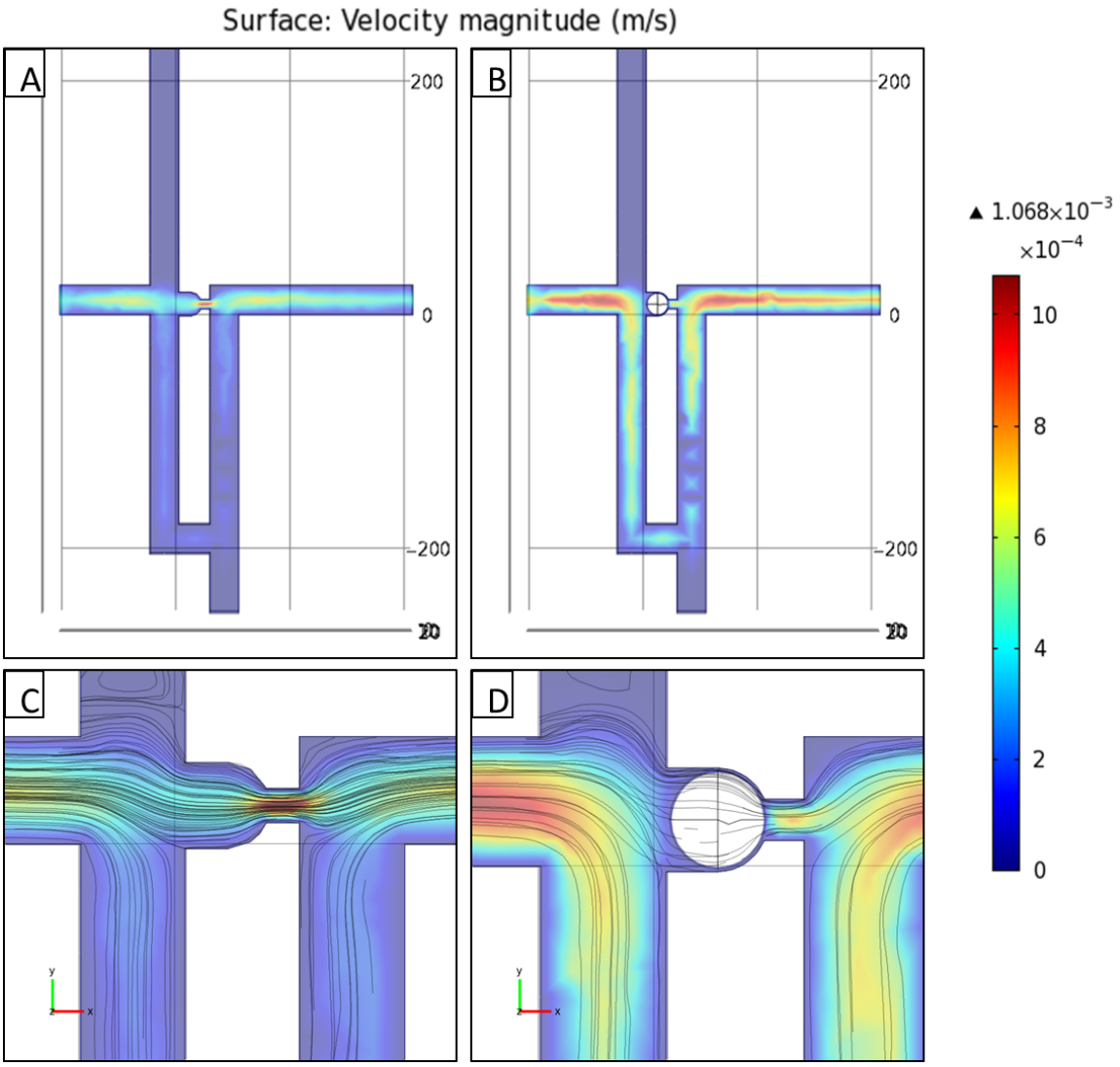

Figure 2-13. 3D-FEM model of fluid flow in hydrodynamic traps. (A) Velocity profile is shown at an empty trap site. The bulk fluid flow goes through path 1 and the trap site. (B) Flow velocity seen at an occupied trap site. The flow velocity, and bulk flow, is now higher through path 2. (C) A closer look at an empty trap site shows the majority of velocity streamlines entering the trap site. (D) A closer look at an occupied site shows increased flow to path 2 and redirection of many of the streamlines. Some fluid does go around the cell through path 1 because the cell does not occupy the entire site in the z-dimension. Inlet velocity was set at 440 µm/s (1 µL/hr flow rate). In this design cells are 20 µm in diameter and L2 = 430 µm, resulting in a Q1/Q2 = 3.33 with an expected capture efficiency of 77%. Images are taken at a z-slice 12 µm from the channel floor (H = 25 µm).

A 3D model of this channel geometry was generated and shown in Figure 2-13. The 3D model shows a more accurate depiction of what the fluid flow looks like in the

real device. Figure 2-13A and B show the fluid velocity at both an empty trap compartment and one with a trapped cell. While it is still clear that the fluid velocity increases to path 2 when a cell is trapped, this effect is less pronounced than with a 2D model. A closer look at Figure 2-13C and D show that the fluid streamlines do not all redirect to path 2 once a cell is captured. This is due to the fact that the channel height is 25 μm, but the cell is only 20 μm in diameter. This means that some amount of fluid is still able to pass around the trapped cell and go through path 1. However, it is still evident that the bulk of the flow is redirected to path 2 and this should still enable effective single-cell capture in the real devices.

In addition to modeling the fluid flow for cell capture, models were generated to investigate the side-channel fluid flow. As previously stated, these side channels are intended to bring in buffers, such as a lysis buffer, and move the captured cell to a secondary compartment after the inter-compartment valves are closed off. Figure 2-14 shows the fluid flow velocities and streamlines from a side-channel inlet flow. As shown in Figure 2-14A (2D) and B (3D), the bulk of the fluid flow flows to the left of the trap site whether a cell is captured or not. Thus, the cell needs only to be pushed out of the trap site and it will easily flow with the bulk flow to the secondary compartments. Figure 2-14C shows a 3D model indicating that even with a cell trapped there is fluid flow coming through path 1 which will aid in dislodging the cell. This is due to the presences of a pressure gradient, as shown in Figure 2-14D, across the trap site. This pressure gradient is sufficient to force fluid through the backside of the trap and dislodge the cell into the main flow.

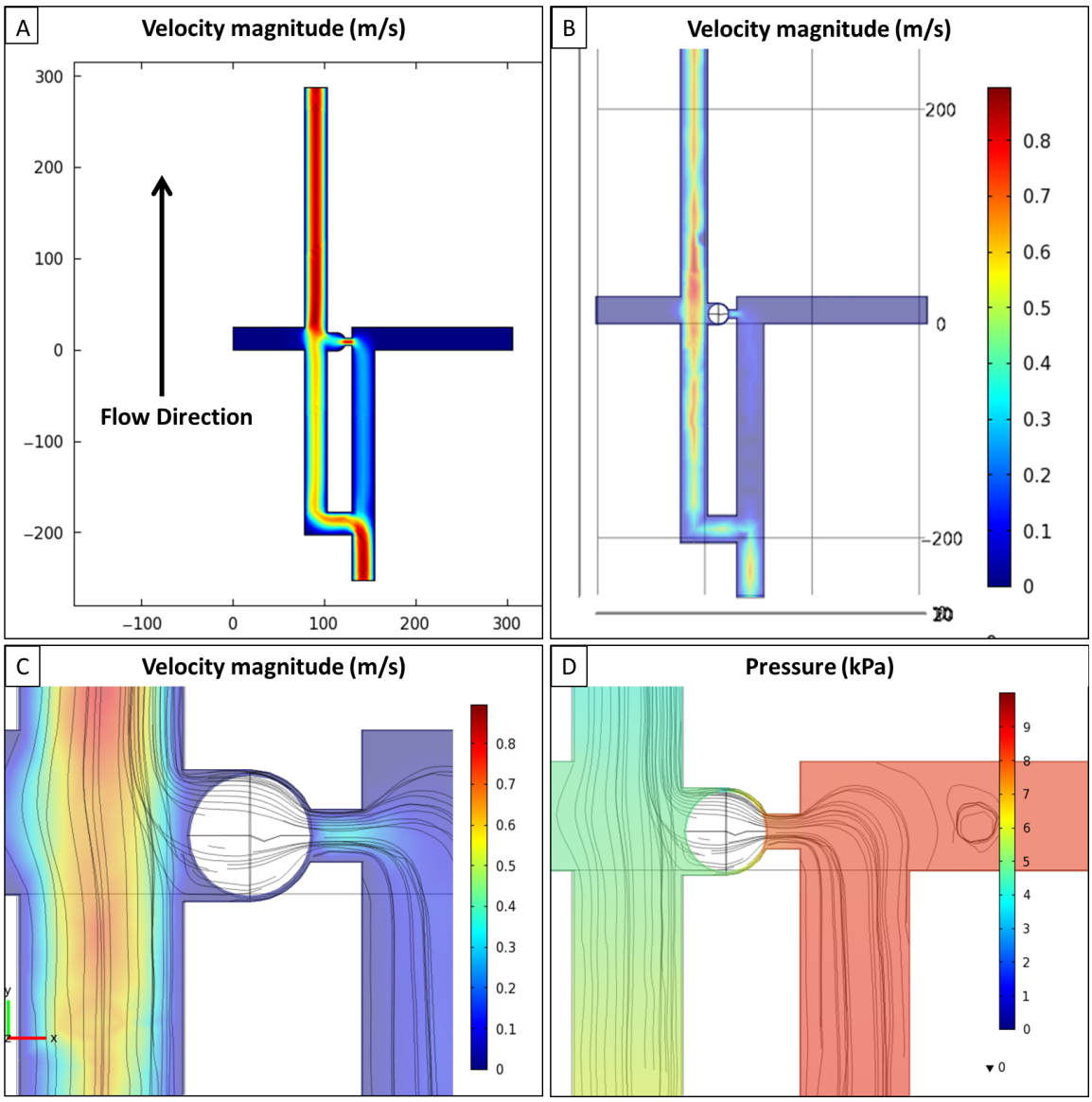

Figure 2-14. FEM models of fluid flow from side-channels. (A) 2D model showing fluid velocity from side-channel. (B) 3D model showing flow velocity with a cell in the trap site. (C) A closer look at the trap site, in 3D, shows the bulk flow to the left of the cell, but with some streamlines on the right that aid in pushing the cell out of the trap. (D) A plot of the pressure in 3D shows that there is a pressure gradient across the trap site with higher pressure on the small side of the trap. This pressure gradient forces fluid through the trap site to dislodge the cell. Models were generated with laminar flow properties. Side-channel inlet pressure was set to 10 kPa and side-outlet to 0 kPa. Images are taken at a z-slice 12 µm from the channel floor (H = 25 µm).

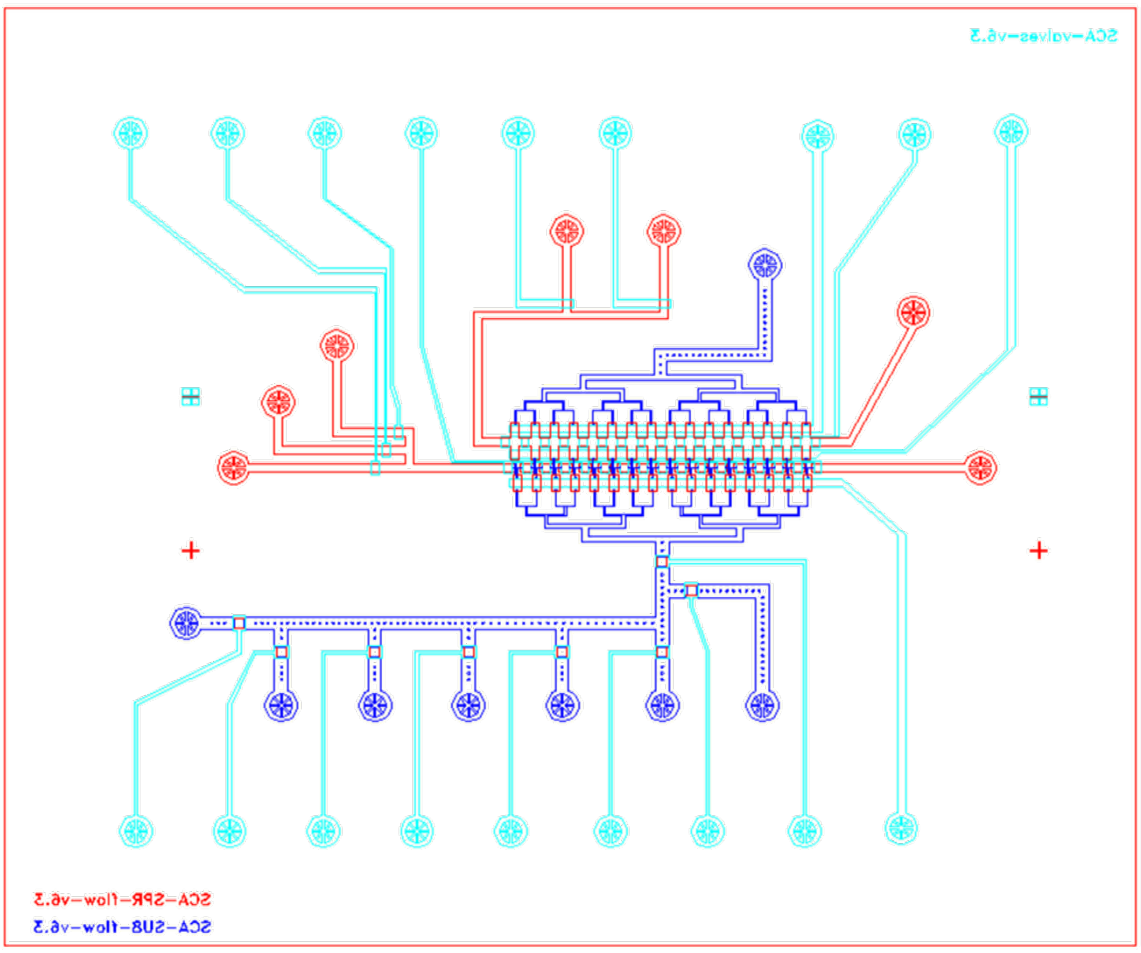

Figure 2-15. CAD design of a single-cell trapping and analysis device. Three layers are overlaid which include the valve control layer (cyan), SPR-220 defined channel regions (red), and the SU-8 defined channel regions (blue). Each layer incorporates alignment marks for precise alignment during device assembly. This design incorporates 16 trapping sites, each with a dedicated secondary channel, along with numerous main channel and side-channel inlets and outlets.

Based off of these types of finite element models, various trap structures could be designed and then fabricated. As long as the fundamentals of the hydrodynamic trap structure were designed appropriately, then other additional geometries would not affect the effectiveness of the traps. Ultimately, a device like the one shown in Figure 2-15 could be designed that incorporates multiple channel inlets, secondary compartments, and

side-channels all built around a series of 16 hydrodynamic traps. The entire device is about 30 mm by 35 mm in dimension, but most of the area required is for the various inlet and outlet holes. The trap sites themselves are at a 600 μm pitch and could possibly be placed closer to one another.

Hydrodynamic capture of single-cells

Various hydrodynamic trap geometries were designed, fabricated, and tested with HeLa cells. Figure 2-16 shows the results of many experiments in various trap geometries, all of which have successfully captured single cells from solution. In each device the fundamental design of the hydrodynamic trap remains constant. There is a narrow path 1 at the trap site and a longer path 2 for which extra cells can flow through to the next trap site. Some of the designs show symmetric trap geometry where there is a single trap site and two bypass paths. These operate on the same principle, but are less effective because the volumetric flow through path 1 is less than the combined volumetric flow through the two alternate paths. Nonetheless, a portion of the fluid flow still enters the empty trap site and cells can be captured. The most effective traps are those that have only a single path 2 and, as described earlier, the efficiency of capture increase with increased path 2 length. Generally though, because there are so many cells in solution, it is easy to achieve a 100% filling rate after flowing for just one minute. Therefore even though the capture efficiency, the proportion of flow to the trap site versus to path 2, may be only around 60-70%, a 100% filling rate can still be achieved if enough cells are flowed through the device. In cases where extremely rare cells should be captured, the cell flow could be recycled through the device to increase the probability of capture.

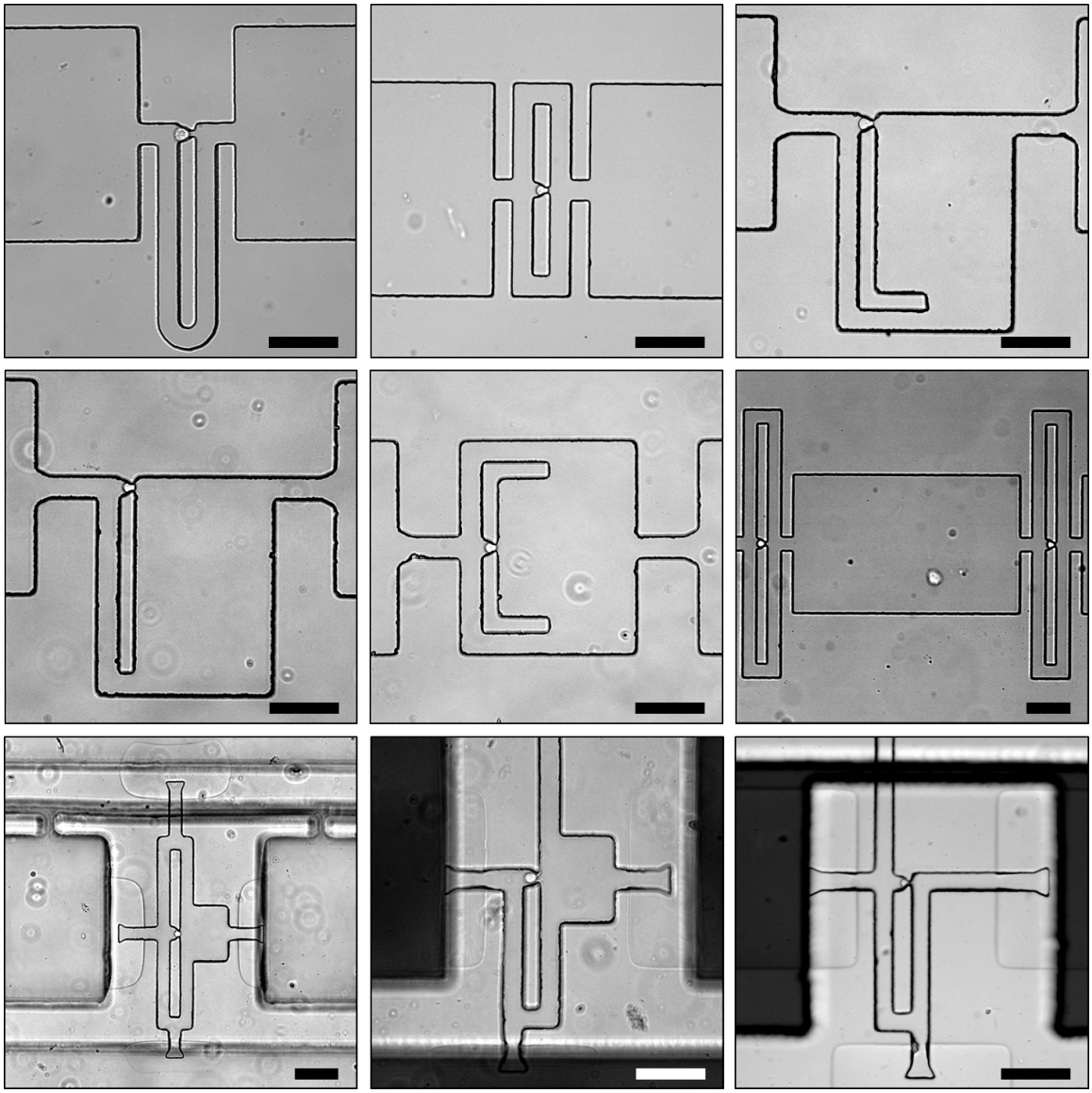

Figure 2-16. Capture of single cells in various hydrodynamic trap designs. Single HeLa cells are trapped by hydrodynamic flow in various device designs. Each design retains the same fundamental geometry. So long as the channels are designed appropriately single cells can be trapped and the rest of the compartment design can be varied. Scale bars correspond to 100 μm in each image.

Another key feature that is seen from Figure 2-16 is the design of larger compartments. As long as there is a defined channel geometry that initially limits Q2 relative to Q1, the rest of the compartment can be freely designed. Thus, larger

compartment space could be added behind the trapped cell which would be useful in downstream analysis applications. The large surface area provides space where molecules could be attached to capture protein or mRNA from lysed cells.

Capture of the single cells was relatively efficient and used low flow rates (around 1 μL/hr). If the flow rates were too fast it was common that the trapped cells could deform enough to squeeze through the trap site. A flow rate of 1 μL/hr correspond to a velocity of about 440 μm/s, which means that cells are traveling at quite a high velocity in the channels. Flow rates over 10 μL/hr, which correspond to about 4 mm/s velocity, easily forced smaller cells through the trap sites. This could be mitigated somewhat by designing smaller path 1 dimensions. If this is done, then path 2 lengths would need to be increased to compensate for the increase in resistance through path 1. Additionally, because these traps use physical confinement, there is bias towards the size of the cell. Smaller cells can much more easily slip through the trap site than larger cells. Future designs could incorporate a series of traps with different dimensions so that cells of various sizes can be captured. This may be helpful with mixed cell samples as such as blood where there are many types of cells with different sizes. Of course, if one wishes to separate or enrich cells by size, these traps would provide a mechanism in which larger cells can be retained and smaller ones flushed away.

Isolation of trapped cells by PDMS valves

Following successful cell capture the individually trapped cells are fully isolated from one another using PDMS valves. Figure 2-17 shows the functionality of the valves and their location relative to the trapping compartments. In Figure 2-17A and B, a

fluorescent microbead solution is injected into the channels. When the valves are open fluorescence signal is seen throughout the channel. When the valves are closed by applying 12 psi of pressure, the microbeads are displaced where the valves contact the substrate surface and there is loss of fluorescence in these areas. Figure 2-17C shows four valves placed around a single trap compartment. The valves are closed with 15 psi of pressure and they are clearly seen to pinch off the channel, as highlighted by the dashed red box. In this design, the left and right valves separate the trap compartment from neighboring traps in series. The top and bottom valves are for the side-channel fluid flow. This shows that integration of complex series of PDMS valves is simple to do and is an effective means to create fully isolated single-cell trap compartments.

The hydrodynamic traps require a very specific geometry in order to effectively capture single cells. Similarly, the PDMS valve regions require a rounded geometry and a 10:1 width to height aspect ratio to function. Because each portion of the channel requires a precise geometry, the mold fabrication required two types of photoresist as outlined in the Experimental Methods. The valve regions of the mold were fabricated first and reflowed to generate the rounded shape. The photoresist also had to be hard-baked to ensure it was compatible with the solvents used in SU-8 processing during fabrication of the trap features. It was also important to design an overlap of the photoresist features. Because the valve portions are rounded, the channel height decreases near the feature edges. To ensure that a cell does not become trapped by the down-sloping ceiling, the SU-8 is patterned to overlap the SPR-220 photoresist by about 70 μm. With careful attention to these details during design and fabrication, the valves are easily integrated with the hydrodynamic traps for compartmentalization of single cells.

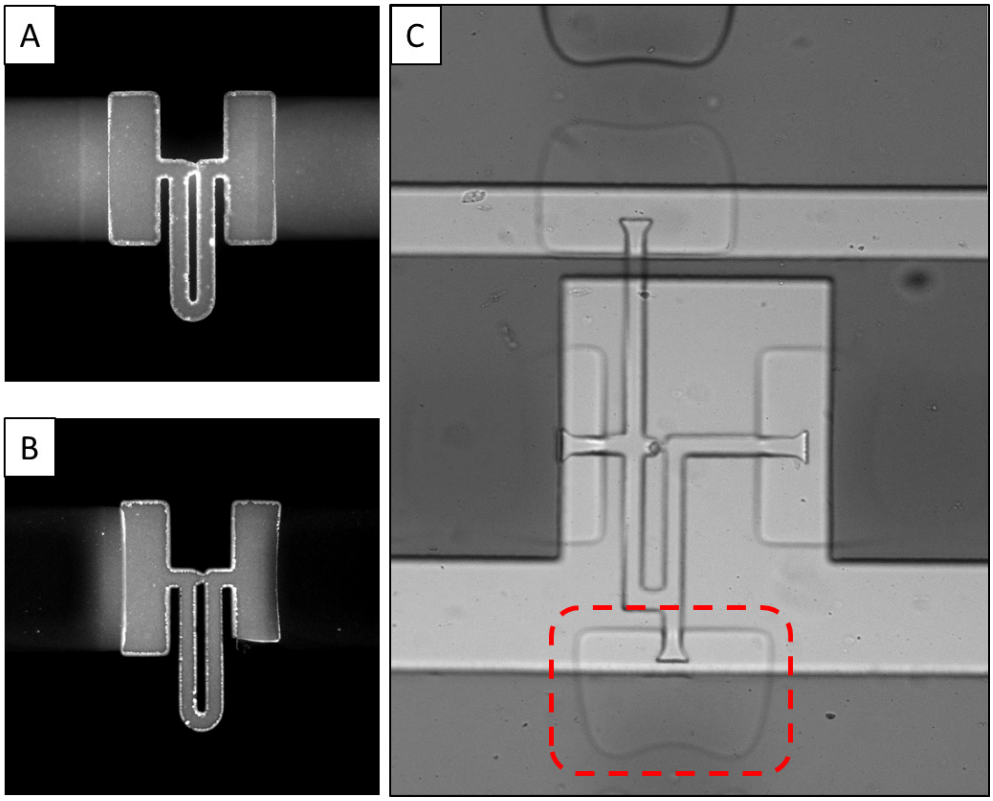

Figure 2-17. Isolation of single-cell trap compartments with PDMS valves. (A) Fluorescent micrograph of a trap compartment filled with a 0.05% solution of 40 nm yellow/green Fluospheres. (B) The compartment is sealed off when the valves are closed by applying 12 psi pressure. (C) Four valves around a single trap compartment are closed with 15 psi of pressure to fully isolate a captured cell. One closed valve is highlighted in the red-dashed box.

Electric-field cell lysis devices

Some of the hydrodynamic cell capture devices were fabricated to include the function of cell-lysis by electric fields. This required the fabrication of gold electrodes onto the glass substrate surface on which the PDMS channels and valves were bonded to. Examples of some these devices are shown in Figure 2-18. For these sets of devices there are no secondary compartments or side-channels because the cell is lysed directly in the primary capture chamber. Molecular capture and analysis would also occur in the capture compartment, therefore designing a larger surface area in the compartment, such as seen

in Figure 2-18C, provides for a region in which detection chemistry can be attached to the surface. As shown in Figure 2-18, it is imperative that the gold electrodes be carefully aligned to the cell trap site. Incorporating alignment features and the alignment process itself is relatively simple; however, difficulties lie in the shrinking of the PDMS after curing. While the shrinking ratio can be determined empirically, the amount of shrinkage was not always consistent. The shrinking ratio is highly dependent on the curing temperature as well as the relative ratio of PDMS base to curing agent. Therefore, as stated in the Experimental Methods, the expansion ratio of the photomasks for the valve and channel layers was different. Care must be taken during the casting and molding process, as well as during the alignment process, because the channel width is relatively small. Any small misalignment or miscalculation of shrinkage ratio could leave one or both of the electrodes outside of the compartment and thereby rendered inoperable.

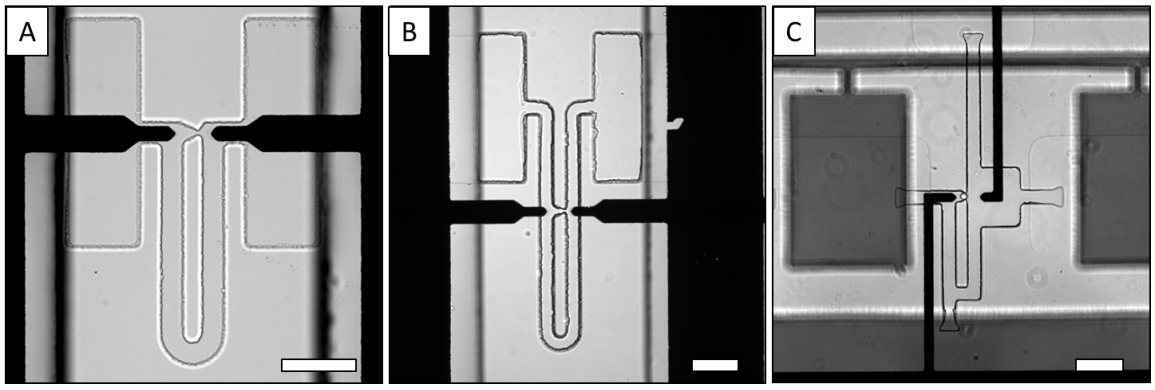

Figure 2-18. PDMS devices aligned to gold electrodes for electric-field cell lysis. (A) and (B) show single cell traps aligned to gold electrode tips with the capture site centered between the two tips. Electrode bus lines run directly under the valving regions. (C) A single cell is captured at a trap site aligned between two electrodes. In this design, the electrode bus lines run parallel to the channels. All scale bars correspond to 100 μm in each image.

After cell capture, the cell can be lysed using an electric-field as described in section 2.3 of this chapter. Figure 2-19 shows an example of the lysis of a captured cell in

the hydrodynamic trap. After cell capture, the inter-compartment valves were closed to fully isolate each cell. Then, an AC sine wave at 20 V_{pp} and 10 MHz is applied. The cell lyses when the frequency is changed to 10 kHz, as shown in Figure 2-19B. The distinct round morphology seen in Figure 2-19A is lost after cell lysis. Electric-field mediated cell lysis is a rapid way to lyse the cells and does not denature proteins like heat or certain chemical lysis reagents may. Thus, this may be a preferred method of lysis for downstream protein analysis.

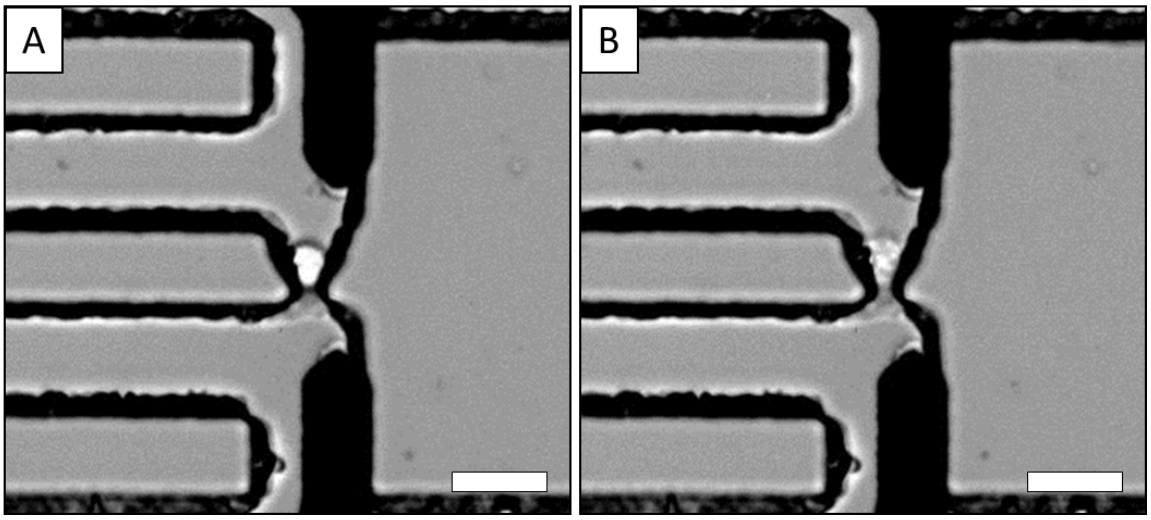

Figure 2-19. Cell lysis by electric field in hydrodynamic traps. (A) A single HeLa cell is captured by hydrodynamic trapping at a trap site aligned to fabricated gold electrodes. (B) The cell is lysed when a 20 V_{pp}, 10 MHz AC sine is applied and suddenly decreased to 10 kHz. Distinct loss of cell morphology is seen. Scale bars correspond to 25 μm.

Chemical lysis in secondary compartments

In other applications, such as mRNA or DNA analysis, it may be advantageous to fully solubilize the proteins and lipids. Thus, chemical lysis methods may be favored over electric-field cell lysis. With electric-field cell lysis there are still remnants or pieces of the original cell. In contrast, chemical lysis is extremely effective at fully lysing and

solubilizing the intracellular contents. Devices incorporating chemical lysis by detergents were designed and involved a more complex system of channels and valves.

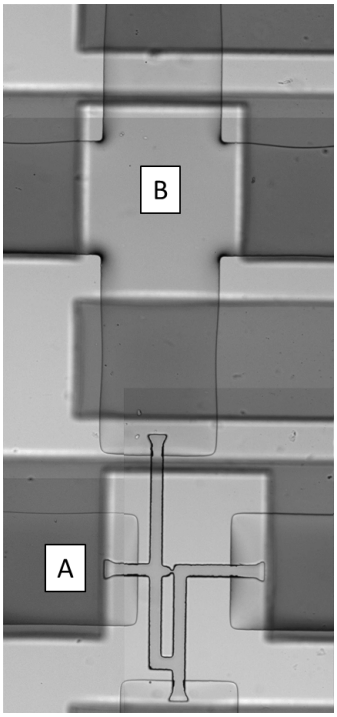

Figure 2-20. Single unit of a single-cell capture and analysis device with side channels. (A) The primary cell capture channel (left to right) where the cell suspension is injected and cells are captured along a series of hydrodynamic traps. (B) The dedicated secondary compartment to the single-cell capture compartment. Following capture, cells are moved into this compartment for lysis and analysis. The primary cell capture compartment channels are 25 μm in width.

In order to incorporate chemical lysis a new device was designed and a single trap unit is shown in Figure 2-20. The hydrodynamic traps are still placed in series with the main cell flow channel shown as Figure 2-20A. Thus, the cell trapping operates in the same manner as before along a linear series of trap compartments. However, because lysis buffer must be injected into the device to lyse the cells, a set of orthogonal channels is designed for each trap compartment. If lysis buffer were injected through the main channel, the cells near the inlet would begin to lyse and their cell contents may wash into

downstream compartments or even out of the device. To prevent this from happening, the new design allows for the lysis buffer to be delivered to each compartment in parallel from side-channels. Figure 2-20B shows the dedicated secondary compartment attached to each trap compartment with a valve in between. Each secondary compartment has valves on each of its 4 sides; 2 to the side-channel inlet and outlet and 2 (left and right) act as inter-compartment valves.

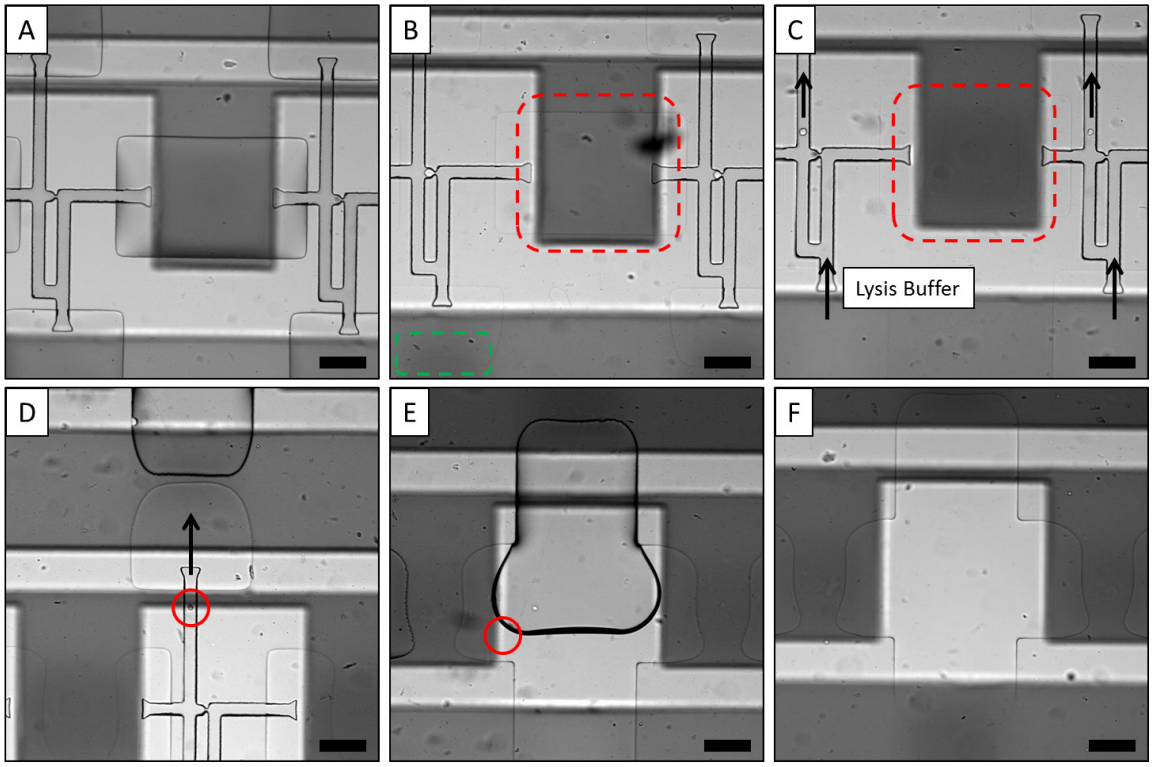

Figure 2-21. Single-cell capture and chemical lysis in secondary compartments. (A) Bright-field micrograph of an empty device showing two neighboring trapping compartments. (B) Single cells have been captured in each of the two trap sites. The inter-compartment valve (red) is open during the cell trapping step, while the side-channel valves (green) are closed. (C) Following cell capture the inter-compartment valves (red) are closed and the side-channel valves opened. Lysis buffer injected from the side-channel dislodges the cells out of the trap sites and directs them towards the secondary compartments. (D) A single cell (red circle) is seen flowing towards the secondary compartment as the side-channel valve is opened. (E) The cell and lysis buffer solution enter the secondary compartment and displace the air. The cell (red circle) loses morphology as it is lysed. (F) The secondary compartment is filled completely with lysis buffer and the cell is no longer visible after it is fully lysed. All four secondary compartment valves are closed and molecular capture and analysis can occur in the closed compartment. All scale bars correspond to 100 µm in each image.

The function of this new device design is shown in Figure 2-21. As seen in Figure 2-21A, the trap compartments are designed as previously mentioned with a valve region in between. Before cells are captured, the side-channel valves are closed off so that the cell suspension can only flow along the main channel and through the series of traps. Cell capture is shown in Figure 2-21B. Both of the trap sites shown have captured single HeLa cells from the suspension. The side-channel valves (green dashed box) remain closed during this process while the inter-compartment valves (red dashed box) are opened. After successful cell capture the inter-compartment valves are closed by pressurizing the valve control lines to 15 psi, as shown in Figure 2-21C. The side-channel is now opened and lysis buffer is flowed in with 1-2 psi of pressure. Just as predicted in the models, this side-channel inflow dislodges the cells from the trap sites and moves the cells towards the secondary compartments, as seen in Figure 2-21D. The cell, along with the lysis buffer, enters into the secondary compartment, as seen in Figure 2-21E. The outlet side valves and the two inter-compartment valves surrounding the secondary compartment remain closed during this loading process. The secondary compartments are initially filled with air. Because PDMS is permeable to air, as the lysis buffer solution enters the compartment, the air is displaced and the compartment filled with solution. This method of moving the cell to an air-filled compartment allows precise transport of the cell in defined volumes. If an open channel is used there is a high-risk of losing the cell completely. The secondary compartment fills fully with the lysis buffer as all the air is displaced, as seen in Figure 2-21F. At this point the secondary compartment valve to the trap compartment can be closed off and cell lysis and molecule release occurs in the ~3 nL secondary compartments. Lysis occurs on the order of minutes, which is slower than

electric-field lysis but is extremely effective at solubilizing the cell contents. As seen in Figure 2-21E, the cell morphology is completely lost after lysis is complete.

The secondary compartments and side-channels are particularly useful additions to the new device designs. The side-channels provide dedicated buffer inlet and outlet to each trap compartment. This ensures each compartment receives the same volume of buffer while also further preventing any cross-contamination between cell compartments. The secondary compartments provide a defined volume for which the cells can be moved into and lysed in. These small volume secondary compartments, about 3 nL, allow for the intracellular molecules to be at a high concentration after lysis, which is advantageous for downstream molecular capture and analysis. This design also avoids the issues of alignment that are associated with the electric-field mediated lysis devices.

2.4.4 Summary

Microfluidic devices incorporating hydrodynamic single-cell capture compartments were designed and fabricated. The devices focus on a series of single-cell traps that operate on the fundamentals of fluidic resistance and are able to efficiently capture many cells in series from the solution flow. Once cells are captured, a system of PDMS valves is used to fully isolate each cell into individual capture compartments. Devices incorporating electric-field cell lysis were designed and involved careful alignment of each trap site to a pair of electrodes. Cells could be efficiently lysed by electric-field directly in the capture compartment. Additionally, devices for chemical cell lysis were designed and involved a more complex system of channels and valves. Each

trap compartment is connected to a dedicated secondary compartment and has side-channels integrated for buffer injection to every trap in parallel. Lysis buffer is injected through the side-channels and transports each cell to dedicated secondary compartments where lysis and downstream analysis can occur. The devices fulfill all the functions of single-cell capture, isolation, and lysis while providing area for downstream molecular analysis.

2.5 Summary and Future Directions

The fundamentals of a single-cell analysis device lie in its ability to capture and isolate individual cells from a sample. In this chapter, I have presented multiple microfluidic device designs capable of capturing single cells from a cell suspension, fully isolating the captured cells using PDMS valves, and then lysing each cell in small nanoliter-sized compartments.

Initial devices captured cells using pDEP in straight 250 μm wide channels and used the same sets of electrodes for electric-field cell lysis. Subsequent devices incorporated well-defined channel geometry for hydrodynamic capture of single-cells based on the principle of relative fluidic resistance in alternate channel paths. The device can capture cells within a minute with a high filling rate. After isolation by PDMS valves, some devices lysed cells by electric-field using fabricated electrodes aligned to cell trap sites. Others incorporated dedicated secondary compartments and side-channels so that lysis buffer, and other downstream analysis reagents, could be independently flowed into each compartment in parallel. Cells were lysed chemically after they were moved from

the primary capture compartments to the secondary compartments. Each of these device designs address the significant challenges associated with capturing single cells and each provides a mechanism for which the cells can be lysed in full isolation from neighboring cells in nanoliter volume compartments.

Future work will include increasing the number of capture sites per device to increase total throughput. This could be done by increasing the number of traps in series along the main channel or by introducing parallel capture channels. Parallel capture channels would be relatively simple to incorporate into electric-field cell lysis devices but would be much more complex in the chemical cell lysis devices that require side-channels. Additionally, the device can be made even more compact if some of the many inlets and outlets are removed from the device and solution switching is done off-chip. Inter-compartment spacing could also be decreased to allow a higher density of trap sites. Finally, another key area would focus on incorporating various sized traps so that cells from a heterogeneous mixture could be captured. On the other hand, a defined trap size could be used to enrich or select specific cells from a heterogeneous mix. Front end cell sorting could also be incorporated to pre-select cell types.

2.6 Acknowledgements

I would like to acknowledge Larry Grissom, Dr. Bernd Fruhberger, and Ryan Anderson at the Nano3 cleanroom facility at Cal(IT)^2 at the University of California, San Diego for support and training. I also thank Dr. Jennifer Y. Marciniak, Dr. Ana B. Sanchez, and Sergio Sandoval at the UCSD Moore's Cancer Center for aid in

troubleshooting cell culture issues. Part of this work was supported by the National Science Foundation under a CAREER award to X. H. (BES-0547193) and grants from the National Human Genome Research Institute (HG004804 and HG004130).

I would also like to acknowledge Ho Suk Lee for assistance in setting up air control lines and solenoid valves. Also, his assistance, along with that of Ximin Chen, in tissue culture and cell maintenance is much appreciated.

Chapter 2, in part, is a reprint of the material as it appears in: Hsiao, A.P., Barbee, K.D. and Huang, X. Microfluidic Device for the Capture and Isolation of Single Cells. *Proc. of SPIE,* 7759, 77590W, doi: 10.1117/12.861563, (2010). The dissertation author was the primary investigator and author of this publication.

2.7 References

1. N. Bontoux, L. Dauphinot, T. Vitalis, V. Studer, Y. Chen, J. Rossier and M. C. Potier, "Integrating whole transcriptome assays on a lab-on-a-chip for single cell gene profiling," *Lab Chip*, vol. 8, no. 3, pp. 443-50 (2008)

2. L. Cai, N. Friedman and X. S. Xie, "Stochastic protein expression in individual cells at the single molecule level," *Nature*, vol. 440, no. 7082, pp. 358-62 (2006)

3. D. Irimia, R. G. Tompkins and M. Toner, "Single-cell chemical lysis in picoliter-scale closed volumes using a microfabricated device," *Analytical Chemistry*, vol. 76, no. 20, pp. 6137-43 (2004)

4. J. S. Marcus, W. F. Anderson and S. R. Quake, "Microfluidic single-cell mRNA isolation and analysis," *Anal Chem*, vol. 78, no. 9, pp. 3084-9 (2006)

5. N. Mittal, A. Rosenthal and J. Voldman, "nDEP microwells for single-cell patterning in physiological media," *Lab Chip*, vol. 7, no. 9, pp. 1146-53 (2007)

6. J. Ryley and O. M. Pereira-Smith, "Microfluidics device for single cell gene expression analysis in *Saccharomyces cerevisiae*," *Yeast*, vol. 23, no. 14-15, pp. 1065-1073 (2006)

7. H. Sedgwick, F. Caron, P. B. Monaghan, W. Kolch and J. M. Cooper, "Lab-on-a-chip technologies for proteomic analysis from isolated cells," *J R Soc Interface*, vol. 5 Suppl 2, no. pp. S123-30 (2008)

8. J. F. Zhong, Y. Chen, J. S. Marcus, A. Scherer, S. R. Quake, C. R. Taylor and L. P. Weiner, "A microfluidic processor for gene expression profiling of single human embryonic stem cells," *Lab Chip*, vol. 8, no. 1, pp. 68-74 (2008)

9. H. C. Fan, J. Wang, A. Potanina and S. R. Quake, "Whole-genome molecular haplotyping of single cells," *Nat Biotechnol*, vol. 29, no. 1, pp. 51-7 (2011)

10. D. Di Carlo, L. Y. Wu and L. P. Lee, "Dynamic single cell culture array," *Lab Chip*, vol. 6, no. 11, pp. 1445-9 (2006)

11. J. Chung, Y. J. Kim and E. Yoon, "Highly-efficient single-cell capture in microfluidic array chips using differential hydrodynamic guiding structures," *Appl Phys Lett*, vol. 98, no. 12, pp. 123701 (2011)

12. S. Kobel, A. Valero, J. Latt, P. Renaud and M. Lutolf, "Optimization of microfluidic single cell trapping for long-term on-chip culture," *Lab Chip*, vol. 10, no. 7, pp. 857-63 (2010)

13. A. K. White, M. VanInsberghe, O. I. Petriv, M. Hamidi, D. Sikorski, M. A. Marra, J. Piret, S. Aparicio and C. L. Hansen, "High-throughput microfluidic single-cell RT-qPCR," *Proceedings of the National Academy of Sciences of the United States of America*, vol. 108, no. 34, pp. 13999-14004 (2011)

14. Y. Kuang, I. Biran and D. R. Walt, "Simultaneously monitoring gene expression kinetics and genetic noise in single cells by optical well arrays," *Anal Chem*, vol. 76, no. 21, pp. 6282-6 (2004)

15. K. Leong, A. K. Boardman, H. Ma and A. K. Jen, "Single-cell patterning and adhesion on chemically engineered poly(dimethylsiloxane) surface," *Langmuir*, vol. 25, no. 8, pp. 4615-20 (2009)

16. J. M. Levsky and R. H. Singer, "Gene expression and the myth of the average cell," *Trends Cell Biol*, vol. 13, no. 1, pp. 4-6 (2003)

17. Y. Gong, A. O. Ogunniyi and J. C. Love, "Massively parallel detection of gene expression in single cells using subnanolitre wells," *Lab Chip*, vol. 10, no. 18, pp. 2334-7 (2010)

18. M. Frénéa, S. P. Faure, B. Le Pioufle, Coquet and H. Fujita, "Positioning living cells on a high-density electrode array by negative dielectrophoresis," *Materials Science and Engineering: C*, vol. 23, no. 5, pp. 597-603 (2003)

19. R. S. Thomas, H. Morgan and N. G. Green, "Negative DEP traps for single cell immobilisation," *Lab Chip*, vol. 9, no. 11, pp. 1534-40 (2009)

20. J. Voldman, M. L. Gray, M. Toner and M. A. Schmidt, "A microfabrication-based dynamic array cytometer," *Analytical Chemistry*, vol. 74, no. 16, pp. 3984-90 (2002)

21. E. Brouzes, M. Medkova, N. Savenelli, D. Marran, M. Twardowski, J. B. Hutchison, J. M. Rothberg, D. R. Link, N. Perrimon and M. L. Samuels, "Droplet microfluidic technology for single-cell high-throughput screening," *Proc Natl Acad Sci U S A*, vol. 106, no. 34, pp. 14195-200 (2009)

22. M. Chabert and J. L. Viovy, "Microfluidic high-throughput encapsulation and hydrodynamic self-sorting of single cells," *Proc Natl Acad Sci U S A*, vol. 105, no. 9, pp. 3191-6 (2008)

23. S. Koster, F. E. Angile, H. Duan, J. J. Agresti, A. Wintner, C. Schmitz, A. C. Rowat, C. A. Merten, D. Pisignano, A. D. Griffiths and D. A. Weitz, "Drop-based microfluidic devices for encapsulation of single cells," *Lab Chip*, vol. 8, no. 7, pp. 1110-5 (2008)

24. Y. Zeng, R. Novak, J. Shuga, M. T. Smith and R. A. Mathies, "High-performance single cell genetic analysis using microfluidic emulsion generator arrays," *Analytical Chemistry*, vol. 82, no. 8, pp. 3183-90 (2010)

25. H. A. Pohl and J. S. Crane, "Dielectrophoresis of cells," vol. 11, no. 9, pp. 711-727 (1971)

26. M. A. Unger, H. P. Chou, T. Thorsen, A. Scherer and S. R. Quake, "Monolithic microfabricated valves and pumps by multilayer soft lithography," *Science*, vol. 288, no. 5463, pp. 113-6 (2000)

27. B. Huang, H. Wu, D. Bhaya, A. Grossman, S. Granier, B. K. Kobilka and R. N. Zare, "Counting low-copy number proteins in a single cell," *Science*, vol. 315, no. 5808, pp. 81-4 (2007)

28. H. Wu, A. Wheeler and R. N. Zare, "Chemical cytometry on a picoliter-scale integrated microfluidic chip," *Proc Natl Acad Sci U S A*, vol. 101, no. 35, pp. 12809-13 (2004)

29. H. Lu, M. A. Schmidt and K. F. Jensen, "A microfluidic electroporation device for cell lysis," *Lab Chip*, vol. 5, no. 1, pp. 23-9 (2005)

30. F. Ozsolak, A. R. Platt, D. R. Jones, J. G. Reifenberger, L. E. Sass, P. McInerney, J. F. Thompson, J. Bowers, M. Jarosz and P. M. Milos, "Direct RNA sequencing," *Nature*, vol. 461, no. 7265, pp. 814-8 (2009)

31. T. Arakawa, M. Noguchi, K. Sumitomo, Y. Yamaguchi and S. Shoji, "High-throughput single-cell manipulation system for a large number of target cells," *Biomicrofluidics*, vol. 5, no. 1, pp. 14114 (2011)

32. W. H. Tan and S. Takeuchi, "A trap-and-release integrated microfluidic system for dynamic microarray applications," *Proc Natl Acad Sci U S A*, vol. 104, no. 4, pp. 1146-51 (2007)

33. A. R. Wheeler, W. R. Throndset, R. J. Whelan, A. M. Leach, R. N. Zare, Y. H. Liao, K. Farrell, I. D. Manger and A. Daridon, "Microfluidic device for single-cell analysis," *Analytical Chemistry*, vol. 75, no. 14, pp. 3581-6 (2003)

34. D. Wlodkowic, S. Faley, M. Zagnoni, J. P. Wikswo and J. M. Cooper, "Microfluidic single-cell array cytometry for the analysis of tumor apoptosis," *Analytical Chemistry*, vol. 81, no. 13, pp. 5517-23 (2009)

3 METHODS FOR SINGLE-CELL PROTEOME ANALYSIS

3.1 Abstract

Uncovering the protein expression profile of single cells is significant in elucidating the phenotypic heterogeneity seen amongst cells in a population. Entire proteome analysis is a daunting task using current methods and the integration of such technologies into microfluidic devices can be significantly more challenging. In this chapter, I present methods and technologies for analyzing the entire proteome of single cells using pre-fabricated antibody-conjugated microbead arrays directly on-chip. High-density antibody-conjugated microbead arrays are fabricated using standard microfabrication techniques in combination with electric-field directed assembly. Additionally, these arrays show picomolar sensitivity using a model antibody-antigen system. Following similar fabrication techniques, antibody-conjugated microspheres are assembled into the individual cell capture compartments using magnetic assembly. Also, I present methods of surface functionalization for microbead patterning and assembly which are compatible with standard PDMS microfluidic device fabrication. Together, these methods have the ability to enable analysis of an entire proteome from single cells within the confines of each compartment of the single-cell analysis microfluidic device.

3.2 Introduction

Analysis of the proteins from a cell allows for understanding of molecular processes and pathways crucial to its function, differentiation, and development. It is well established that cells within the same population have unique protein expression[1-4]. Such differences may point to unique subpopulations of cells that are not detectable using ensemble, bulk measurements. These subpopulations of cells may provide great insight into understanding disease progression, drug resistance, cell differentiation, and molecular pathways. Thus, recent efforts to uncover single-cell protein expression have increasingly grown.

Typical methods of analyzing proteins at the single-cell level include fluorescence-assisted cell sorting (FACS) using flow cytometry, direct *in situ* labeling, and mass spectrometry[5-8]. While some of these methods, such as flow cytometry, offer great throughput in cell number, they often require cumbersome preparation of samples and are limited in their sensitivity of low copy number proteins as well as in the number of analytes they can interrogate at a time. Accordingly, in efforts to increase sensitivity by decreasing sample volumes, as well as integrate sample preparation methods, microfluidic approaches have been developed. These include flow cytometry methods, mass spectrometry, and affinity capture of proteins on pre-functionalized substrates[9-14]. These technologies are not without their limitations as well. Thus far, they are only capable of interrogating a few number of cells at a time and do not have the ability to effectively analyze thousands of proteins simultaneously. Moreover, integration with PDMS microfluidics is non-trivial.

In fact, surface functionalization and patterning within PDMS devices poses a significant challenge in itself due to the fact that the surface chemistry may be destroyed during oxygen plasma activation and thermal bonding[15, 16]. Some have circumvented this restriction by using mild PDMS bonding, such as clamping or adhesives, but these also can pose risks to the substrates and surface molecules. Additionally, weak bonding is not optimal for integrated PDMS devices that require a large number of reagent flows and substantial flow pressures. This could limit the ability to effectively use microfluidic devices to capture and analyze proteins directly from single cells. Applications using photolithography to mask and protect pre-functionalized surfaces has been used with PDMS assembly methods and shown to be successful in patterning cells[17]. Similar methods could potentially be used to assemble antibody-conjugated microbeads.

In this chapter I present methods to enable interrogation of the entire proteome from single-cells using microfabricated antibody-bead arrays assembled into the PDMS single-cell analysis devices. First, high-density antibody-conjugated microbead arrays are presented that will allow for multiplexed analysis of hundreds to thousands of proteins simultaneously on a small area. Second, I discuss methods of surface functionalization and incorporation of protective patterning for array assembly into the microfluidic devices that are compatible with standard, permanent PDMS bonding techniques. Together, these methods will enable single-cell proteome profiling from captured cells on pre-fabricated antibody arrays all within the PDMS microfluidic device. This not only reduces potential sample loss, but it allows for reduced reagent use and increased sensitivity due to smaller reaction volumes. Ultimately, it also provides for a simple device capable of the entire range of single cell capture to analysis.

3.3 High-density Antibody-conjugated Microbead Arrays

3.3.1 Introduction

The ability to interrogate proteins in a sensitive, quantitative, multiplexed and high-throughput manner has many applications in proteomic analysis[18-20], cancer research[21, 22], diagnostics[23] and drug discovery[24]. Although established methods such as western blots [25] and enzyme-linked immunosorbent assays[26] (ELISA) can be used for sensitive and reliable protein detection and quantification, they are labor-intensive and require large sample volumes. Furthermore, they allow for the analysis of only a small number of samples and proteins at a time. Alternatively, the use of spotted protein and antibody microarrays enable greater multiplexing and significantly reduced sample volumes[27-35]. Other groups have demonstrated the potential advantages of assays that employ protein- and antibody-conjugated microbeads, which allow for even greater multiplexing and scalability than those performed in microtiter plates or on spotted arrays[36-43]. The majority of these microbead-based immunoassays are typically performed in solution[36, 37] or on-chip[38-43]. The solution-based formats are fast and sensitive but they require specialized flow cytometry equipment for sample analysis. In contrast, chip-based formats are well suited for analysis via epifluorescence microscopy and allow for the integration of additional lab-on-a-chip processes such as nucleic acid extraction and genetic profiling from single cells or whole blood[44, 45].

Methods for assembling or capturing antibody-conjugated microbeads on chip-based platforms include micromanipulation[38], microfluidic trapping[39, 40], evaporation of microbead suspensions on etched silicon[41] or fiber-optic bundles[42], and electrostatic self-

assembly on chemically-modified substrates[43]. Many of these platforms enable multiplexed analysis by using a mixed population of encoded microbeads or by physically isolating each population in separate microfluidic channels. In this work, we report the development of a new approach for fabricating and assembling microbead arrays. We utilize an electric field to direct the assembly of antibody-conjugated microbeads onto a microfabricated array of wells. The process takes place within a microfluidic device and arrays of micron to sub-micron beads can be assembled in 15-45 seconds. Moreover, we have demonstrated that antibody-conjugated microbead arrays can be assembled and used for sensitive, multiplexed protein detection in many samples in parallel. In contrast to previously reported methods, our approach enables much faster and more scalable array assembly. The array format provides the order and spatial separation necessary for packing a large number of microbeads into an extremely small footprint. For instance, nearly 7000 sub-micron beads can be rapidly assembled on an array just 100 μm x 100 μm in size. This small footprint may enable the analysis of entire proteomes at the single cell level[1, 4]. In addition, our device may provide a means for electrophoretically accelerating the transport of antigens to decrease assay times and to enhance sensitivity[46-48].

Another key advantage of our approach is the ability to assemble arrays in a controlled, stepwise fashion. By introducing and assembling a small number of microbeads from a single population at a time, we can record their physical locations on the array[49]. This spatial encoding method enables a large range of multiplexing capabilities without the need for fluorescence encoding[50, 51] or other more complex strategies[52, 53]. In this study, we demonstrate the feasibility of a combined encoding

approach by assembling two different fluorescence microbead populations per round. This combination of both fluorescence and spatial encoding schemes gives us even greater multiplexing potential.

The method and device described here also encompass significant improvements over those previously reported for rapid electric-field directed assembly of streptavidin-conjugated microbead arrays[54]. In our previous work, the high-density array of wells was patterned in an epoxy-based photoresist on a gold-coated silicon wafer. The gold served as the working electrode, whereas the counter electrode consisted of an indium-tin oxide (ITO) film on a glass coverslip. In this study, the microwells are fabricated in a silicon dioxide film and the counter electrode consists of a series of thin gold lines on a glass coverslip. The use of a silicon dioxide layer results in a more robust platform and enables more precise control of the microwell geometry. The use of the gold lines as counter electrodes results in better light transmission and eliminates the problems associated with the degradation of ITO from the by-products of electrolysis[55].

3.3.2 Experimental Methods

Fabrication of arrays of microwells in an oxide on gold

Figure 1A illustrates the general procedure for the fabrication of an array of microwells in a silicon dioxide film on a gold-coated wafer. First, 150 mm diameter silicon wafers were cleaned and then coated with silicon dioxide as described previously[54]. Films of titanium, gold and titanium were sequentially deposited on the oxide-coated wafer using a Denton Discovery 18 sputter system. The deposition chamber

was typically evacuated to a base pressure of 9 $\times 10^{-7}$ Torr or less and the films were deposited at 150-200 W DC in 3.0 $\times$ 10^{-3} Torr Ar flowing at a rate of 36 sccm. The two titanium layers, which serve as adhesion layers between the oxide and gold films, were approximately 10 nm thick. The thickness of the gold film was ~300 nm. Following metallization, another 100-300 nm of silicon dioxide was deposited via PECVD as described previously[54]. A Filmetrics F20 measurement system was used to determine the oxide film thickness.

To fabricate the microwell arrays, the wafers were first coated with a bottom anti-reflective coating (BARC) (ARC 29A-8, Brewer Science) by spin-coating at 2250 rpm for 30 s. After baking the BARC at 220 °C for 60 s, a 250 nm-thick film of deep UV photoresist (ARF AR1682J-15, JSR Micro) was applied via spin-coating at 1000 rpm for 40 s. Edge bead was removed from the front and back sides of the wafers with propylene glycol monomethyl ether acetate (Baker BTS-220, J. T. Baker). All coating, baking and edge bead removal steps were performed on a SVG 90-SE coat track. The resist was baked at 110 °C for 90 s and then exposed on a PAS 5500/950B Step and Scan System (ASML) equipped with a 10 W, 193 nm ArF excimer laser (ELS-6610A, Cymer). Arrays of posts were patterned on the substrates using a quartz reticle containing chrome contacts on a clear background. Typical doses ranged from 12-24 mJ/cm^2. The exposed wafers were baked at 110 °C for 60 s, developed in MF-319 (Rohm & Haas Electronic Materials) for 60 s and rinsed with dH_2O in a quick dump rinser. The wafers were then rinsed and dried in a spin-rinse-dry tool (PSC-101, Semitool). To remove the BARC, the wafers were exposed to an oxygen-based plasma for 75 s at 50 W RF at 8 sccm and 4.0 $\times$ 10^{-2} Torr in a RIE system (System VII, Plasma-Therm).

Next, the patterned wafers were coated with 30 nm of nickel via a Temescal BJD 1800 electron-beam evaporation system. The chambers were typically evacuated to base pressures of 7×10^{-7} Torr or less and nickel films were deposited at 1.0-2.0 Å/s. The resist and unwanted metal was removed using Shipley Microposit Remover 1165 (Rohm & Haas Electronic Materials) at 70 °C with ultrasonic agitation for ~6 hr. After rinsing in dH_2O and drying with nitrogen, the exposed oxide was etched in a Panasonic FP-EA01A ICP etcher using 40 sccm CHF_3 at 0.5 Pa with 900 W forward RF power and 200 W reverse RF power. The substrates were cooled via backside helium flow at 15 sccm and 700 mTorr. Under these conditions, the average etch rate for PECVD-grown silicon dioxide was ~0.20 μm/min. However, etch times were extended by as much as 50% to ensure that the upper layer of titanium was also completely removed to fully expose the underlying gold film.

Following the etching process, the wafers were coated with a thick layer of Shipley Megaposit SPR220-3.0 (Rohm & Haas Electronic Materials) photoresist by spin-coating at 2000 rpm for 30 s and then baking at ~100 °C for 5 min. Holes for fluidic connections were then drilled in the wafers using a 1.0 mm diamond-coated drill bit (Cat. # MD16, C. R. Laurence Co.) and a high speed rotary tool (38481 IB/E, Proxxon) mounted to a CNC milling machine (PCNC-1100, Tormach). The wafers were secured in a custom-built jig and flooded with a dilute coolant solution (Formula #77, Kool Mist) while drilling. The wafers were then diced with a dicing saw (DAD3220, Disco). The resist was stripped by soaking in acetone for 3 min and then in isopropanol for 1 min. After drying with nitrogen, the nickel layer was stripped for 10 min at room temperature

in a nickel etchant (Type TFB, Transene Co.). The wafers were then rinsed with dH_2O and dried with nitrogen.

Fabrication of counter electrode lines on glass coverslips

Figure 1B illustrates the general procedure for the fabrication of the counter electrode lines on a glass coverslip. Using a custom-built PTFE rack, 50 mm × 75 mm × 0.170 mm (Erie Scientific Co.) glass coverslips were cleaned as described previously[54]. Prior to fabrication, the coverslips were blown dry with nitrogen and then baked on a hotplate at ~200 °C for 5 min to remove any remaining moisture. After cooling, HMDS was applied and allowed to sit for 30 s before spin-drying at 4000 rpm for 30 s. A layer of Shipley Megaposit SPR220-3.0 was then applied by spin-coating at 3500 rpm for 30 s. The resist was baked at 115 °C for 90 s and then exposed to 365-405 nm light on a Quintel contact aligner using a photomask printed on a transparency film. An exposure time of 18 s at ~10 mW/cm^2 was typically used to print 25 μm wide lines at a pitch of 320 μm. After baking the exposed coverslip at 115 °C for 90 s, the resist was developed for 90 s in MF-24A developer (Rohm & Haas Electronic Materials), rinsed with dH_2O, and dried with nitrogen.

After a 3 min oxygen plasma treatment in a Technics PEII-B plasma system at 100 W RF and 3.0×10^{-1} Torr O_2, a Denton Discovery 18 sputter system was used to deposit a 10 nm-thick titanium film followed by a 300 nm-thick Au film. Sputtering was performed at 150 W with 3.0×10^{-3} Torr Ar at 36-38 sccm. The resist and unwanted metal was then removed by soaking the substrate in Shipley Microposit Remover 1165 at 70 °C in an ultrasonic bath for up to 1 hr. The coverslip was then washed with acetone,

rinsed with dH_2O and dried with nitrogen. Line height measurements were obtained with a Dektak 150 surface profiler (Veeco Instruments).

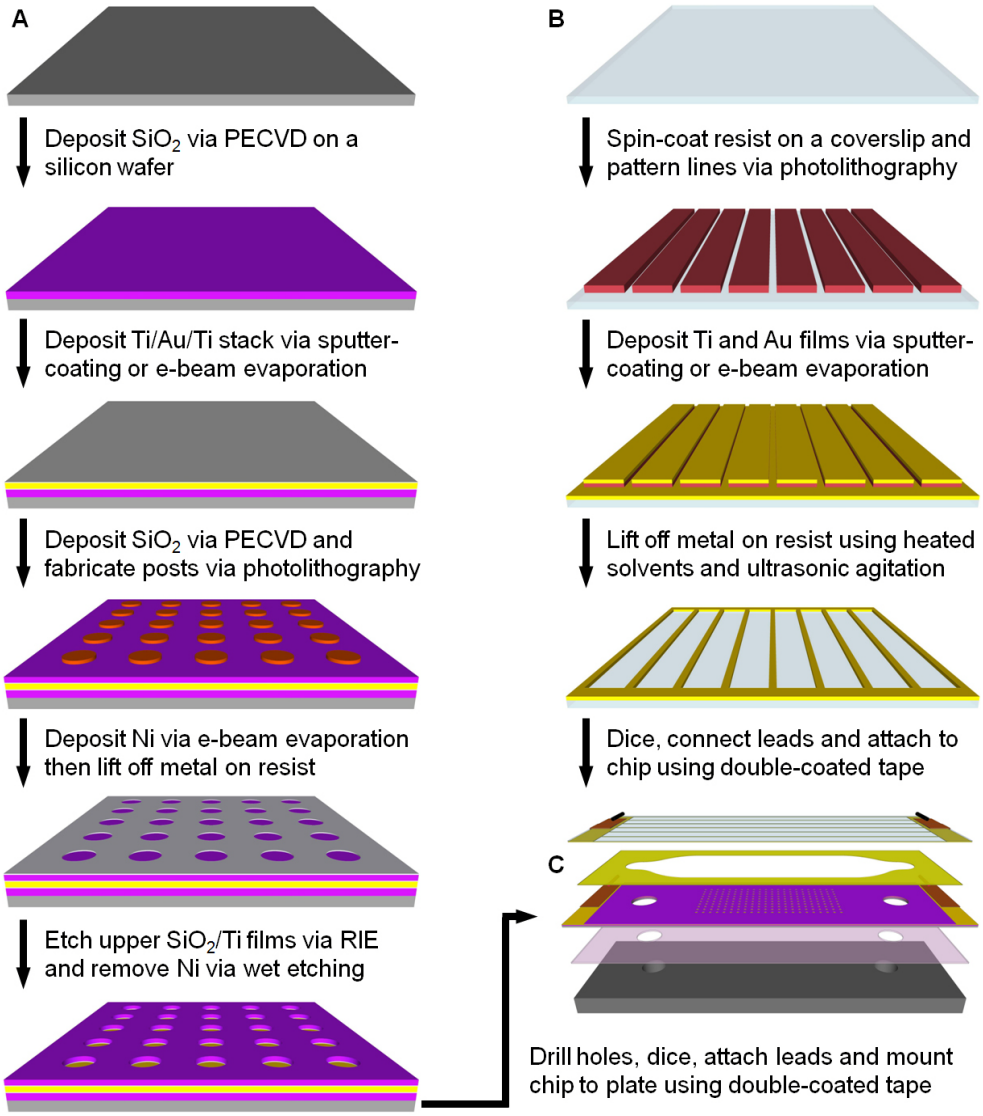

Figure 3-1. Fabrication and assembly of the electrophoretic device. (A) Fabrication of an array of microwells in silicon dioxide on a titanium-gold-titanium stack on a silicon wafer. (B) Fabrication of gold counter electrode lines on a glass coverslip via a lift-off process. The gold lines serve as counter electrodes in the assembled chamber and are only 25 µm wide with a pitch of 320 µm to allow for imaging of the microbead arrays. (C) Assembly of the device and mounting to a custom-built aluminium plate with tapped ports for fluidic connections. Drawings are not to scale.

Device assembly

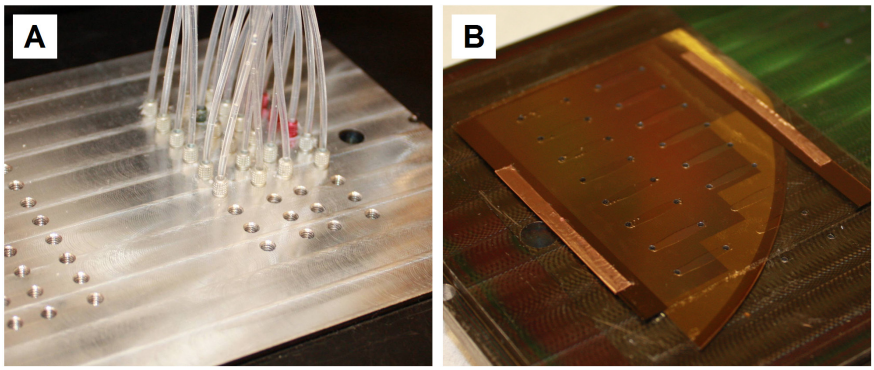

Figure 3-2. Photographs of the assembled electrophoretic fluidic device. (A) Top view of the custom-built aluminium plate through which the fluidic connections are made to each channel in the device. (B) Bottom view of the plate and an assembled device containing 14 separate channels. The bottom side of the aluminium plate has been coated with titanium and silicon dioxide films to aid in the adhesion of the double-coated tape.

An exploded view of the electrophoretic device is shown in Figure 3-1C. The general method for assembly of this device has been described elsewhere [54]. Briefly, each chip was cleaned by exposing it to oxygen-based plasma at 100 W RF and 3 $\times 10^{-1}$ Torr O_2 for 3 min in a Technics PEII-B plasma system. After rinsing with dH_2O and drying with compressed air, the chip was mounted to a custom-built aluminium plate using a double-coated adhesive tape. The flow cell was then formed by attaching the coverslip with the counter electrodes to the chip via a second double-coated adhesive tape containing cut-outs of the fluidic channels. Channel dimensions were 2 mm wide by 10 mm long with a height of ~110 μm. Electrical connections were made to the gold film on the chip and the counter electrode lines using copper tape. Fluidic connections were made via ports in the aluminium plate (Figure 3-2).

Antibody conjugation to microbeads

Biotinylated antibodies (biotin-XX goat anti-mouse IgG (H+L), Cat. # B2763 and biotin-XX F(ab')$_2$ fragment of goat anti-rabbit IgG (H+L), Cat. # B21078, Invitrogen) were conjugated to 0.4 or 1 μm streptavidin-coated green (ex. 480/em. 520) and red (ex. 660/em. 690) fluorescent polystyrene beads (Cat. # CP01F/8682, CP01F/7678 and CP01F/8963, Bangs Laboratories) by adding drop-wise a 0.2% microbead suspension to a solution containing one of the biotinylated antibody species. Each conjugation was performed in phosphate buffered saline (PBS, 137 mM sodium chloride, 2.7 mM potassium chloride, 10 mM sodium phosphate dibasic and 2 mM potassium phosphate monobasic, pH 7.4) at an antibody concentration corresponding to five to ten times the amount required to cover the surface of all microbeads in the suspension. A 4 μL drop of the microbead suspension was delivered to the antibody solution every 5 s using a syringe pump (Cavro XR Rocket Pump, Tecan Group) and the mixture was vortexed throughout the mixing process. After the addition of the entire microbead suspension, the mixture was shaken at room temperature for 1 hr. The microbeads were then washed four times with PBS and stored at 4 °C until use.

Microbead array assembly

Antibody-conjugated microbeads were assembled using optimized parameters as described elsewhere[54]. Briefly, the microbeads were exchanged into a low conductance buffer (LCB, 4.5 mM tris(hydroxymethyl) aminomethane, 4.5 mM boric acid and 0.02% Triton X-100, pH 8.6, 60 μS/cm conductivity) and introduced into the flow cell at a concentration of 0.02% to 0.2% solids. The microbeads were assembled by applying 3.0

V DC pulses at 1 Hz and a 10% duty cycle for 15-45 s in 15 s intervals with a 1-2 min pause between each interval. The microbeads were pulled into the wells via electrophoresis and were permanently bound to the gold surface through electrochemically-induced interactions. Excess microbeads were then washed away using a syringe pump.

Spatial and fluorescence encoding of microbeads

A mixture of two populations of antibody-conjugated microbeads, one with green fluorescence and one with red fluorescence, were introduced into the flow cell and then subjected to exactly four electrical pulses. Microbeads that were not captured were washed away and then the array was imaged using a DM LFSA epifluorescence microscope (Leica Microsystems) equipped with a 40x/0.55 NA objective, a Cascade 650 CCD camera (Photometrics) and a fast wavelength-switching light source with a 300 W xenon arc lamp (Lambda DG-5, Sutter Instrument Co.). Array scanning was achieved via a BioPrecision 2 XY microscope stage and a MAC 5000 controller system (Ludl Electronic Products). This process was repeated a total of ten times to demonstrate the principle of combining both fluorescence and spatial encoding schemes to record the positions of 20 different microbead populations. The images were aligned and combined using custom macros in ImageJ[56] to produce a spatial map of the array.

Sandwich immunoassays

Two antibody-conjugated microbead populations (goat anti-mouse IgG microbeads and goat anti-rabbit IgG microbeads) were combined at a 1:1 ratio and

diluted to ~0.02% for each species. The microbeads were assembled into an array using 5-15 pulses then washed with PBS with 0.05% Tween-20 (PBS-5T). A blocking solution (SuperBlock blocking buffer in Tris-buffered saline, pH 7.4, Cat. # 37545, Pierce Biotechnology) with 0.05% Tween-20 (SB-5T) was then introduced into the chamber. After a 30 min incubation, the chamber was washed with PBS-5T. A solution containing the antigens diluted to specified concentrations using PBS-5T with 10% SB-5T was then loaded. After a 90 min incubation, the chamber was washed with PBS-5T and a solution containing both detection antibodies was introduced into the chamber. After a 30 min incubation, the chamber was washed with PBS-5T and the array was imaged on a fluorescence microscope. The test antigens were mouse and rabbit immunoglobulin proteins (Mouse IgG, Cat. # 2-6502; Rabbit IgG, Cat. # 2-6102, Invitrogen) and the detection antibodies were fluorescently labelled antibodies (Alexa Fluor 568 goat anti-rabbit IgG (H+L), Cat. # A11036; Alexa Fluor 568 goat anti-mouse IgG (H+L), Cat. # A11031, Invitrogen). To generate standard curves, 10 μL of the antigen solutions were introduced at concentrations ranging from 6 to 625 pM (100 ng/mL). Experiments were repeated 3 times at each antigen concentration. Negative controls were also conducted using an identical procedure but without antigen in the solution. After a 90 min incubation, the chamber was washed with PBS-5T. A solution containing a mixture of the detection antibodies diluted with PBS-5T to a concentration of 4 μg/mL each was then introduced into the chamber. After a 30 min incubation, the chamber was washed with PBS-5T and then imaged with an automated epifluorescence microscopy system. The microbead assembly and sandwich immunoassay process is illustrated in Figure 3-3.

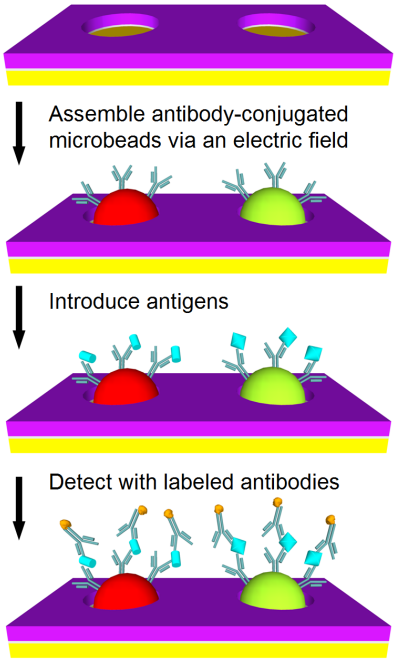

Figure 3-3. Sandwich immunoassay on antibody-conjugated microbeads assembled via electrophoretic deposition. Antibody-conjugated microbeads are assembled on the microfabricated arrays via the application of a pulsed electric field. Multiplexed protein detection is then performed within the same microfluidic channel using a sandwich immunoassay. Drawings are not to scale.

Fluorescence imaging

Quantitative fluorescence imaging of the antibody arrays was performed on an Axio Observer.Z1 epifluorescence microscope (Carl Zeiss) equipped with a 40x/1.3 NA oil objective, a 1-megapixel EMCCD camera (iXon+ 885, Andor Technology) and a Lambda DG-5 light source. Imaging on the Axio Observer.Z1 was fully-automated using custom software. Auto focusing was performed with a Definite Focus System (Carl Zeiss) and array scanning was controlled via a BioPrecision 2 XY microscope stage and a MAC 5000 controller system. For each antibody array, multiple fields of view were acquired along the length of the channel. For each field of view, images were taken in three fluorescence channels using the appropriate filter cubes (FITC-3540B, TXRED-4040B,

and Cy5.5-A, Semrock). To image the microbeads in the FITC channel, a neutral density filter (ND 2.0 A, Chroma Technology) was used to reduce the output from the light source.

Image analysis

The data from the sandwich immunoassays was analyzed in ImageJ using a custom macro. Briefly, the program generated a mask of the anti-rabbit and anti-mouse microbeads for each field of view using the images taken in the FITC and Cy5.5 channels, respectively. After locating the center of each microbead, the program identified the pixels associated with the microbead and calculated the mean pixel intensity in the corresponding Alexa 568 detection channel. The mean background pixel intensity for each microbead type was obtained from negative control experiments in which no antigen was added. A microbead was considered to have detected a given antigen if its mean fluorescence intensity in the corresponding channel was greater than three times the standard deviation of the mean background intensity of the microbeads in the same channel[57]. A standard curve was then generated for each microbead type by plotting their mean, background subtracted intensities as a function of antigen concentration. Results were gathered from the analysis of multiple images and each image contained ~150 microbeads.

SEM imaging

Scanning electron microscopy (SEM) was performed on a Phillips XL30 ESEM or FEI Sirion operating in high-vacuum mode. Prior to imaging with the XL30, the samples were coated with iridium using an Emitech K575X desktop sputtering system.

ITO transmission and resistivity measurements

The effects of electrophoretic assembly conditions on the optical transparency and resistivity of ITO films were studied using a modified chamber design. To enable easy disassembly, each ITO-coated glass slide (Cat. # CG-511N-S115, Delta Technologies) was positioned over a gold-coated slide outfitted with a PEEK gasket (Cat. # 5804K42, McMaster-Carr Co.) and held in place with binder clips. The gap between the two substrates was filled with LCB via capillary action. The chip was then subjected to a 3 V DC potential in 1 min intervals. The device was disassembled after each interval and the optical transmittance of the ITO film was recorded with a Lambda 20 UV-Vis spectrometer (Perkin Elmer). The resistance across the ITO film was also measured after each interval using a digital multimeter (Model # 2010, Keithley Instruments).

Finite element analysis

The variation in the electric field strength within the device was modelled using COMSOL Multiphysics v3.4 (COMSOL AB) and MATLAB 7.7.0 (Mathworks). A cross-section of the chamber, which included ~830 microwells across a span of 2 mm, was drawn to scale and the conductive media DC application was used to plot the electric field strength in the media using different counter electrode configurations. In the first

study, the chamber height was fixed at 110 μm and the pitch between the counter electrode lines was varied from 160 μm to 640 μm. In a second study, the counter electrode line pitch was fixed at 320 μm and the chamber height was varied from 55 μm to 220 μm. In both studies, the height of the counter electrode lines was 0.3 μm and the wells were 0.25 μm deep by 1.2 μm wide at a 2.4 μm pitch. The media was assigned a conductivity of 60 μS/cm, which corresponds to the conductivity of the LCB used during microbead assembly. The bottom of each well was set to 3.0 V DC while the counter electrode lines were set to ground. All other entities were electrically insulating. Horizontal line plots were generated for each counter electrode line configuration at a height of 5 μm above the surface of the array and spanned between the centers of two adjacent counter electrode lines.

3.3.3 Results and Discussion

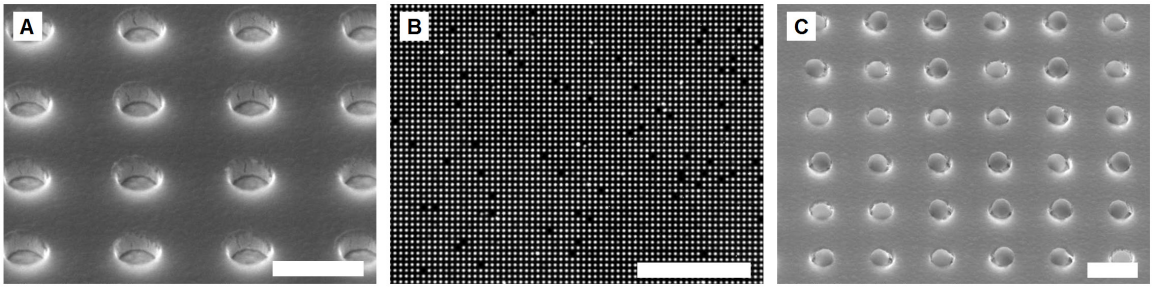

Figure 3-4. Arrays of microwells and antibody-conjugated microbeads. (A) SEM image of a small portion of an array of ~0.5 μm wells at a 1.2 μm pitch etched in a silicon dioxide film that was deposited on a gold-coated wafer. (B) Raw fluorescence image of a small portion of an assembled array of 0.4 μm antibody-conjugated beads at a 1.2 μm pitch. (C) SEM image of a small portion of an assembled array of 0.4 μm antibody-conjugated beads at a 1.2 μm pitch. The scale bars in (A) and (C) are 1 μm. The scale bar in (B) is 24 μm.

We have developed a microfabricated electrophoretic device comprised of a high-density array of wells in silicon dioxide on a gold-coated silicon chip and a glass coverslip containing a series of thin gold lines. A typical SEM image of an array of microwells fabricated in silicon dioxide on a gold film is shown in Figure 3-4A. By applying a pulsed electric field across the device, we have demonstrated that 0.4 and 1 μm antibody-conjugated microbeads can be rapidly assembled into high-density arrays with excellent filling efficiencies and near perfect order. A sample fluorescence micrograph and SEM image of a small portion of an array of antibody-conjugated microbeads assembled within the oxide wells are shown in Figures 3-4B and 3-4C, respectively.

Spatial and fluorescence microbead encoding

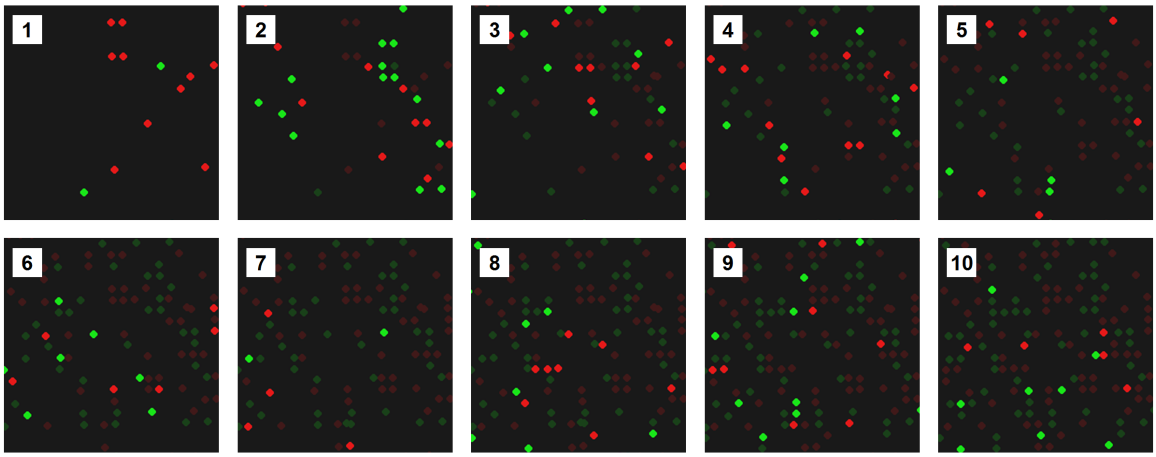

Figure 3-5. Spatial and fluorescence encoding of antibody-conjugated microbead arrays. Fluorescent micrographs of a small portion of an antibody-conjugated microbead array assembled in a stepwise fashion over the course of ten rounds using two different fluorescent microbeads (Panels 1-10). In panels 2-10, the brightness of the previously assembled microbeads has been reduced to emphasize the newly assembled microbeads.

To perform multiplexed immunoassays, we utilize both fluorescence and spatial encoding schemes to enable the identification of each microbead after it has been assembled on the array. An example of a combined encoding scheme is shown in Figure 3-5. In this instance, a mixture of two populations of microbeads with either red or green fluorescence were introduced into the flow cell and then subjected to exactly four electrical pulses. Microbeads that were not captured were then washed away and the array was imaged via epifluorescence microscopy, thus recording the exact location of each microbead. This process, which only takes a few seconds per round, was repeated multiple times to demonstrate the gradual filling of the array and our ability to map each microbead type following each assembly round. The number of microbeads assembled in each round can be controlled by varying the microbead concentrations as well as the number of pulses applied during each round. Additionally, if more fluorescent barcodes are used, many more populations of antibody-conjugated microbeads can be assembled simultaneously during each round, resulting in much greater multiplexing capabilities.

Immunoassays

Sandwich immunoassays were conducted to demonstrate that our platform could support sensitive, quantitative and multiplexed protein detection. For each immunoassay, a mixture of two populations of antibody-conjugated microbeads were assembled onto an array via an electric-field and then treated with a blocking solution prior to being exposed to a solution containing the antigens. The microbeads were then probed with fluorescently labeled detection antibodies and subsequently imaged via automated epifluorescence microscopy. With each type of capture antibody conjugated to a different

fluorescently-labeled microbead, we were able to detect simultaneously two different antigens. The fluorescent signal from each microbead was measured in the detection channel (Alexa 568) and an antigen was considered present if the mean intensity in its corresponding channel was at least three times the standard deviation of the mean microbead background intensity in the same channel[57]. Standard curves were generated using antigen concentrations ranging from 0 to 625 pM and our detection limit was determined to be ~40 pM (6 ng/mL) (Figure 3-6), which is similar to the sensitivities of other microbead-based immunoassays[42, 43]. The variation in our mean intensities can be attributed to non-uniformity in the microbead populations and slight focusing inconsistencies in fluorescence imaging.

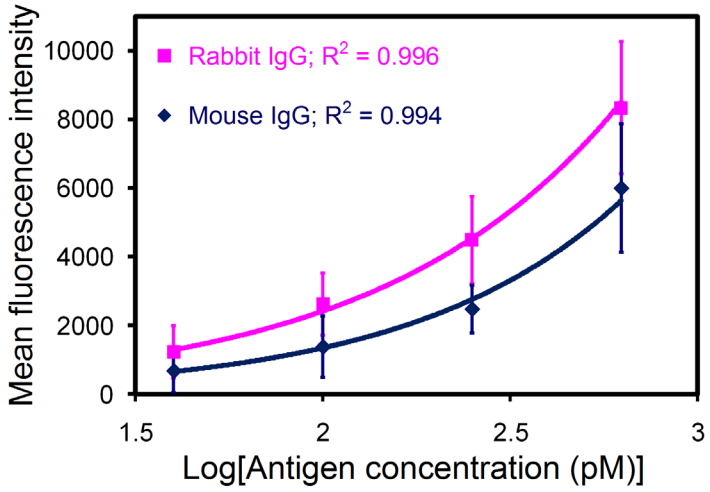

Figure 3-6. Standard curves for the sandwich immunoassays performed on antibody-conjugated microbead arrays. Graph of the mean fluorescence intensity from 1 µm antibody-conjugated microbeads as a function of the $\log_{10}$ of the antigen concentration. Our detection limit was determined to be ~40 pM (6 ng/mL) for both antigens.

Optimization of parameters such as surface chemistry[58, 59], incubation times and the number of a given type of antibody-conjugated microbead assembled on the array may help bring the sensitivity of this approach closer to that of ELISA but without

enzymatic signal amplification. The latter of these factors may be of importance at low antigen concentrations due to the small number of antigens available per microbead. Therefore, it may be beneficial to limit the number of microbeads of a given type to the minimum necessary to give statistically significant data. Other potential improvements include fluid oscillation, optimization of the incubation temperature and the application of an electric-field to direct the antigens toward the electrode-bound microbeads[46-48]. These approaches may enhance the diffusion-limited process of capturing antigens, thereby increasing the sensitivity of the assay and reducing the total assay time. Furthermore, the sensitivity of our immunoassays may also be improved through the use of quantum dot-labeled detection antibodies[60] or an immunoRCA strategy[61].

Silicon dioxide wells

The use of silicon dioxide as a dielectric for the electrophoretic assembly of colloidal crystals has been demonstrated elsewhere[62]. We have utilized this material in our device because it offers numerous advantages over the epoxy-based photoresist used in previous work[54]. Although the fabrication process is simpler when using epoxy-based photoresist, the wells are partially destroyed during the plasma cleaning of the gold electrodes. In addition, the photoresist is more susceptible to chemical damage from the by-products of electrolysis during the microbead assembly process. In contrast, silicon dioxide can withstand harsh environments and processes and may enable the use of various chip bonding techniques such as anodic and thermal bonding. It is also well-suited for direct bonding to PDMS. The use of silicon dioxide also enables more control over the geometric properties of the wells. For instance, precise depths and vertical wall

profiles are easily produced. In addition, the use of a silicon dioxide layer facilitates the use of higher resolution microfabrication processes such as DUV lithography and RIE/ICP. Once the array of microwells have been fabricated, the surface properties of the oxide can be modified using silane-based chemistry, which would allow, for example, the passivation of the oxide with polyethylene glycol (PEG) to prevent non-specific binding of microbeads and biomolecules[58].

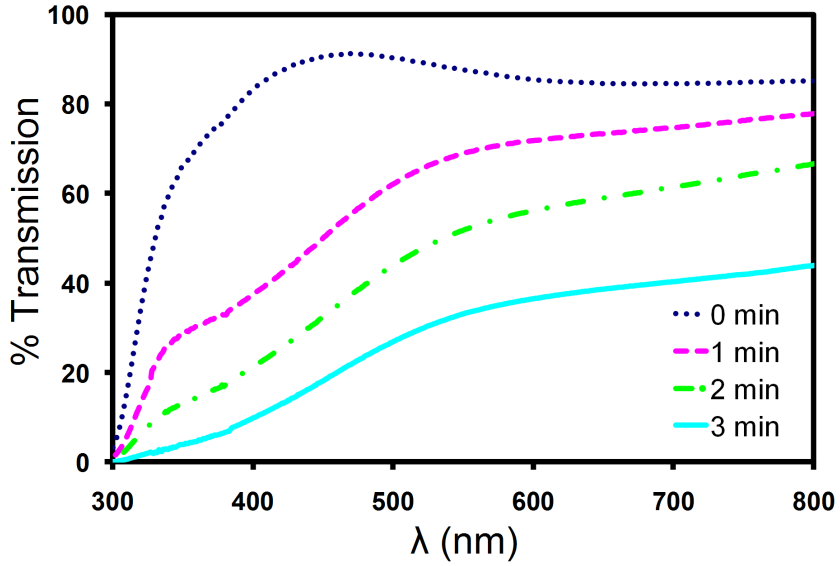

Figure 3-7. Light transmission through an ITO film subjected to electrophoretic conditions. Plot of the percentage of light transmittance through an ITO-based electrophoretic device as a function of total exposure time to electrophoretic conditions.

Counter electrode lines

The use of a counter electrode that consists of a series of gold lines fabricated on a glass coverslip offers several advantages over the use of an ITO-coated coverslip. First, there is no loss of light when imaging between the gold lines. In contrast, ITO films are typically only 80-90% transparent to light in the visible spectrum, which could effectively reduce the sensitivity of epifluorescence-based assays. Second, the gold lines can be fabricated using a relatively simple lift-off process whereas the deposition of high-

quality ITO films requires the optimization of multiple parameters. Third, the gold lines are also very durable compared to ITO films, which tend to degrade when subjected to high electrical currents or the by-products of electrolysis that are produced under electrophoretic conditions. While a small number of 3.0 V DC electrical pulses may not have a significant effect, continuous exposure to these electrophoretic conditions for just one minute can result in a significant reduction in the transmission of visible light through the film. To demonstrate this phenomenon, we measured this transmittance of an ITO film after subjecting it to a continuous 3.0 V DC potential (Figure 3-7). The experimental results indicate that the drop in transmittance is wavelength dependent, but is greater than 90% in the lower end of the visible spectrum after just three minutes. This decay would significantly affect the imaging sensitivity of a system using ITO as a counter electrode. The electrical properties of the ITO film were also affected to some degree as evidenced by a doubling of the sheet resistance after three minutes.

Although the use of gold lines as counter electrodes may produce non-uniform electric fields within the chamber, microbead assembly was still rapid and uniform across the entire array when 25 μm counter electrode lines at a pitch of 320 μm were used. However, our attempts to assemble similar arrays using lines at a 640 μm pitch were unsuccessful. We developed a 2-D finite element model of the device to examine the electric field distribution within the chamber for varying counter electrode line pitches and chamber heights. A cross-sectional view of a section of the chamber is illustrated in Figure 3-8A. A screenshot of a portion of a solved model is shown in Figure 3-8B. For each device configuration studied, a horizontal line plot between adjacent counter electrode line centers was generated at a height of 5 μm above the surface of the array. In

Figure 3-8C, the chamber height was held at 110 µm while the counter electrode line pitch was varied from 160 µm to 640 µm. At this chamber height, the drop in field strength from a position directly underneath the center of an electrode line to the midpoint between adjacent electrode lines varied from 10% at a pitch of 160 µm to 96% at a pitch of 640 µm. At a pitch of 320 µm, this drop was 60%, and yet we were still able to achieve uniform assembly with this configuration. However, observations made using electrode lines at a 640 µm pitch confirmed that there is a threshold below which assembly cannot be performed.

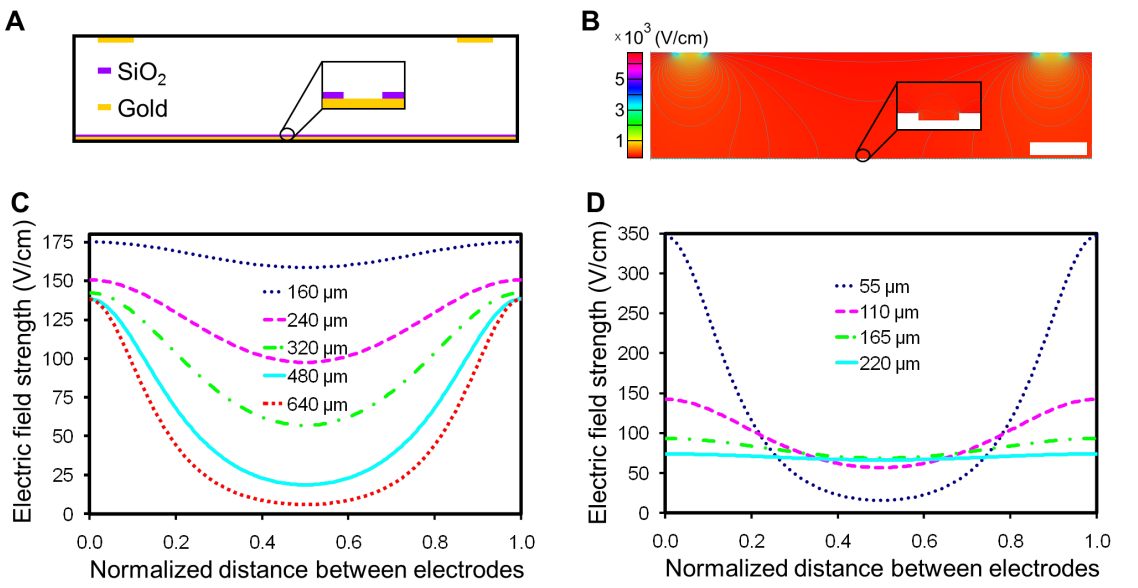

Figure 3-8. Finite element analysis of the electric-field distribution within the microfabricated electrophoretic device. (A) An illustrative cross-section of a portion of the device. (B) Surface and contour plot of the y-component of the electric-field strength, Ey, in a scaled COMSOL model of the device. In this particular model, the counter electrode lines are 25 µm wide at a pitch of 320 µm. The chamber is 110 µm high by 2 mm wide and the wells are 0.25 µm deep by 1.2 µm wide with a pitch of 2.4 µm. The inset shows the electric field distribution within a single well. The scale bar is 50 µm. (C) A plot of Ey as a function of the horizontal position between neighboring counter electrode line centers for varying counter electrode line pitches. The channel height was held at 110 µm. (D) A plot of Ey as a function of the horizontal position between neighboring counter electrode line centers for varying chamber heights. The counter electrode line pitch was held at 320 µm. The line plots in (C) and (D) were generated at a fixed height of 5 µm above the surface of the array and the applied potential across the chamber was 3.0 V DC.

In Figure 3-8D, the pitch was held at 320 μm while the chamber height was varied from 55 μm to 220 μm. At this pitch, the drop in field strength from a position directly underneath the center of an electrode line to the midpoint between adjacent electrode lines varied from 10% at a height of 220 μm to 95% at a height of 55 μm. This indicates that a uniform electric field could be attained by simply changing the height of the chamber. However, a significant increase in height will prohibit the use of microscope objectives with short working distances and may require a higher voltage for assembly. In our particular model, we do not take into account electrohydrodynamic and convective flow, but future models that include these factors may allow us to optimize further the electrode configurations, device geometry, and electrophoretic conditions[63, 64].

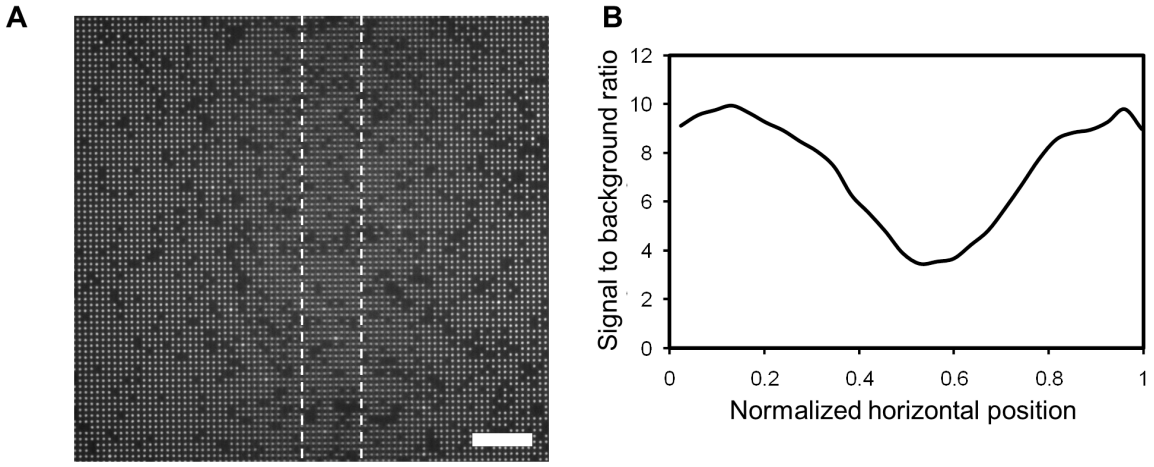

Figure 3-9. Imaging of microbeads under and near a gold counter electrode line. (A) Fluorescent micrograph of 1 μm antibody-conjugated, fluorescent polystyrene beads assembled near and under a 25 μm gold counter electrode line. The approximate location of the electrode line is given by the dashed lines and is 110 μm above the focal plane in this image. (B) A corresponding profile of the signal to background ratio across the entire 200 μm wide image. The scale bar in (A) is 24 μm.

We found that 25 μm-wide lines at a pitch of 320 μm allow for excellent microbead assembly as well as unobstructed imaging between them when imaged with a

40x objective and an EMCCD camera with 1004 × 1002 pixels (8 μm × 8 μm pixels). Lines that were too close together lead to the presence of shadows in the images. As shown in Figure 3-9, these shadows diminish the signal from the microbeads up to a distance of ~50 μm from the line. The image was acquired in the FITC channel in a region of the chip where 1 μm antibody-conjugated beads were located directly underneath a 25 μm-wide counter electrode line. Even though the counter electrode lines need to be spaced such that imaging can be performed far enough from the lines to avoid their shadows, this approach offers greater durability and better light transmission than ITO while still providing the means for uniform, efficient assembly of the antibody-conjugated microbeads.

3.3.4 Summary

We have demonstrated that high-density, antibody-conjugated microbead arrays can be assembled via electrophoretic deposition on microfabricated arrays of wells in silicon dioxide on gold-coated silicon chips. In addition, thin gold lines fabricated on glass coverslips were used as counter electrodes to provide a more robust platform for assembly and enable greater imaging sensitivity than possible with ITO-coated coverslips. Assembly of the antibody-conjugated microbeads was rapid and resulted in high-density arrays with minimal defects. We have demonstrated the feasibility of a spatial encoding scheme and have also shown that the assembled antibody arrays could be used to detect test antigens at concentrations as low as 40 pM (6 ng/mL) using sandwich immunoassays. Our microfabricated electrophoretic device and methods will be useful for rapid assembly

of encoded antibody arrays for multiplexed detection of proteins. Furthermore, our ability to assemble antibody-conjugated microbeads may be extended to a multitude of other types of protein-conjugated microbeads for other applications such as the analysis of protein-protein interactions.

3.4 Integration of Microbead Arrays into PDMS Devices

3.4.1 Introduction

The integration of the high-density antibody-conjugated microbead arrays into the PDMS microfluidic device poses many technical challenges. Firstly, with thick PDMS atop a glass substrate making sensitive imaging from the top impossible, it is imperative that any epifluorescence imaging be done through the glass substrate itself. This means that having a non-transparent gold electrode upon which the high-density microbead array is assembled is not an option. Alternatively, by using a magnetic assembly approach the glass substrate's transparency could be preserved. Our lab has previously shown the ability to assemble high-density arrays of magnetic microbeads[65]. However, by selecting a magnetic assembly approach it is required that the substrate surface be chemically modified to allow for the antibody-conjugated microbeads to bind to the surface. As stated in this chapter's introduction, integrating chemical surface modification with PDMS assembly is a significant challenge because modified surfaces are susceptible to damage during standard PDMS bonding processes.

In this section, I present methods to overcome these challenges by combining chemical surface modification with photolithographic patterning to protect the surface

molecules. I show how these methods are compatible with standard PDMS device assembly techniques and how they are applied in conjunction with magnetic assembly to assemble antibody-conjugated microbeads directly into single-cell capture compartments. Altogether, these techniques provide a mechanism for which high-density antibody-conjugated microbead arrays can be fabricated into PDMS microfluidic devices for single-cell proteome analysis.

3.4.2 Experimental Methods

Biotin functionalization of glass substrates

Coverglass substrates (50x50 mm, #1.5 thickness, Fisher), either stock or post-electrode fabrication, were first cleaned by rinsing briefly in a 2% Micro-90 detergent solution. The substrates were then immersed in acetone and placed into an ultrasonic water bath for 15 minutes. The solution was exchanged with methanol and the substrates sonicated for an additional 15 minutes before a final rinse with dH_2O. The substrate surfaces were activated by immersing in a 14% solution of nitric acid for a minimum of 1 hour. The substrates were subsequently rinsed with dH_2O and dried with an argon air gun. A 3-aminopropyltriethoxysilane (APTES, Fisher) in 95% ethanol was prepared and let to sit for 5 minutes before the glass substrates were immersed into the solution for 5 minutes. The substrates were then washed with acetone before drying in a 110 ºC oven for 10 minutes. A 1 mM biotin-PEG-SCA (MW 5000, Laysan Bio) solution was prepared in dimethylformamide (DMF) with 1 mM triethylamine. A small volume of about 200 μL was then pipetted onto one glass substrate and a second substrate was sandwiched onto

the first. This allowed functionalization of two substrates simultaneously. The substrates were placed into a humid dish and the functionalization reaction occurred at room temperature overnight. Finally, the substrates were taken apart and each rinsed in acetone and dried with an argon air gun. Biotin-functionalized substrates were stored in a vacuum desiccator until use.

Photolithographic patterning of assembly regions

Photomasks were designed in AutoCAD (Autodesk, Inc.) and plotted on transparencies at a minimum of 20,000 dpi (FineLine Imaging). Transparency masks were mounted onto 5" x 5" borosilicate glass for use in the Karl Suss MA6 aligner. Biotin-functionalized substrates were spin-coated with Shipley S1813 positive photoresist at 5000 rpm for 30 seconds followed by soft-baking at 80 ºC for 2 minutes. The patterns were then aligned to the substrates and exposed to UV light for 30 seconds on the MA6 under hard contact mode at a light intensity of 11 mW/cm^2. The photoresist was then developed away using Microposit MF-321 developer by immersion for 70 seconds followed by rinsing in dH_2O and drying by nitrogen air gun.

Surface activation and PDMS channel bonding

PDMS channels were prepared without the valve control layer using similar methods to those outlined in Chapter 2. In brief, a 10:1 PDMS mix was used and about 35-40 g was poured onto the flow channel mold, degassed, and then cured at 75 ºC in a convection oven for a minimum of 2 hours. The PDMS and the photoresist-patterned biotin-functionalized glass substrates were then exposed to oxygen plasma in a UVO

cleaner (Jelight) for 4 minutes. The glass-substrates were then soaked in Microposit 1165 remover and placed into an ultrasonic water bath for 5 minutes to remove the patterned photoresist. The substrates were rinsed with dH_2O and dried by argon air gun. The PDMS was then aligned to the glass substrates using a custom built alignment system with x, y, z, and theta control. First, rough alignment was done with the PDMS a few mm away from the substrate surface. Then, a few drops of methanol were spotted onto the substrate and the PDMS lowered to make contact with the substrate surface. The methanol served as a lubrication layer so that the PDMS can be moved atop the substrate surface during fine alignment. After aligning, the PDMS remained pressed to the substrate surface until the methanol evaporated allowing for contact between the PDMS and the glass surface. The device was then moved to an oven at 75 ºC for a minimum of 2 hours for permanent bonding.

Antibody conjugation to magnetic microbeads

First, 20 µL of stock 1 µm-diameter streptavidin-coated Dynal microbeads (Dynal MyOne-SA, Invitrogen) were diluted into 80 µL of a 0.1% bovine-serum albumin (BSA) solution in PBS (BSA-PBS). The microbeads were washed 3 times by pelleting the beads with a magnet and exchanging the supernatant with fresh BSA-PBS. In a separate tube, 8 µL of stock 2 mg/mL biotin-XX-rabbit-anti-goat IgG (H+L) (Invitrogen) was diluted into 92 µL of BSA-PBS. The antibody solution was then delivered to the microbead suspension drop-wise; 4 µL of solution was delivered every 5 seconds using a Cavro XR Rocket Pump (Tecan Group) syringe pump while the mix was constantly vortexed. After transferring all of the antibody solution to the microbeads, the mixture was placed on a

rotating mixer (MACsMix) and incubated overnight at 4 ºC. Finally, the antibody-conjugated microbeads were washed 4 times into PBS with 0.02% Tween-20 (PBS-T) at a final microbead concentration of 0.1%. Antibody-conjugated microbeads were stored at 4 ºC until use.

Verification of surface by microbead assembly in glass and tape microchannels

Channels with dimensions of 30 mm x 3 mm at a 10 mm pitch were cut in Scapa 702 double-sided tape on a CAMM-1 Servo cutter plotter (Roland). One side of the tape was affixed to the pre-functionalized and post-patterned coverslips. A 50 mm x 75 mm glass slide pre-drilled with inlet and outlet ports was aligned and affixed to the other side of the double-sided tape. This formed sealed channels defined by the tape, coverslip, and glass slide. Protein-free blocking buffer was then pipetted into each channel and allowed to incubate at room temperature for 1 hour. The blocking buffer was flushed out with PBS-T by pipetting 100 μL of buffer a total of three times. For initial tests, a 0.1% solution of streptavidin-conjugated magnetic microspheres (Dynal-MyOne) was pipetted in and the microbeads were pulled down to the surface with a magnet. Excess beads were flushed away by pipetting 50 μL of PBS-T buffer through each channel. The microbeads assembled on the surface were then imaged using bright-field microscopy on an inverted microscope (Zeiss AxioObserver). For antibody-conjugated microbead tests, just after flushing the channels clean of the blocking buffer, a 113 μM solution of streptavidin in PBS-T was injected into the channels and allowed to incubate at room temperature for at least 30 minutes. The streptavidin solution was then washed out with PBS-T and a 0.1% solution of rabbit-anti-goat IgG-conjugated microbeads was loaded into the channels. The

microbeads were pulled to the surface using a magnet and excess microbeads were flushed out with PBS-T buffer. The assembled microbeads were imaged using bright-field microscopy on an inverted microscope (Zeiss).

Antibody-conjugated microbead assembly in PDMS microfluidic channels

The PDMS microfluidic channels were first loaded with a protein-free blocking buffer (Pierce) for 30 minutes to reduce non-specific binding of the antibody-conjugated microspheres. All solutions were loaded using an infusion syringe pump (Chemyx). The blocking buffer was then washed out with PBS-T and the channels loaded with a 113 μM solution of streptavidin (Pierce) in PBS. The streptavidin solution was allowed to incubate in the channels at room temperature for 1 hour. The channels were then washed with PBS-T. A 0.1% solution of rabbit-anti-goat IgG-conjugated microbeads was loaded into the PDMS microfluidic channels. A magnet was swiped across the bottom glass substrate a few times to attract the magnetic microbeads to the glass substrate surface. Any unbound microbeads were then washed out of the channels by flowing PBS-T through the channels at a flow rate of 100 μL/hr. Images of the bound microbeads were then acquired by bright-field microscopy on an inverted Zeiss epifluorescent microscope using an Andor iXon EMCCD camera.

3.4.3 Results and Discussion

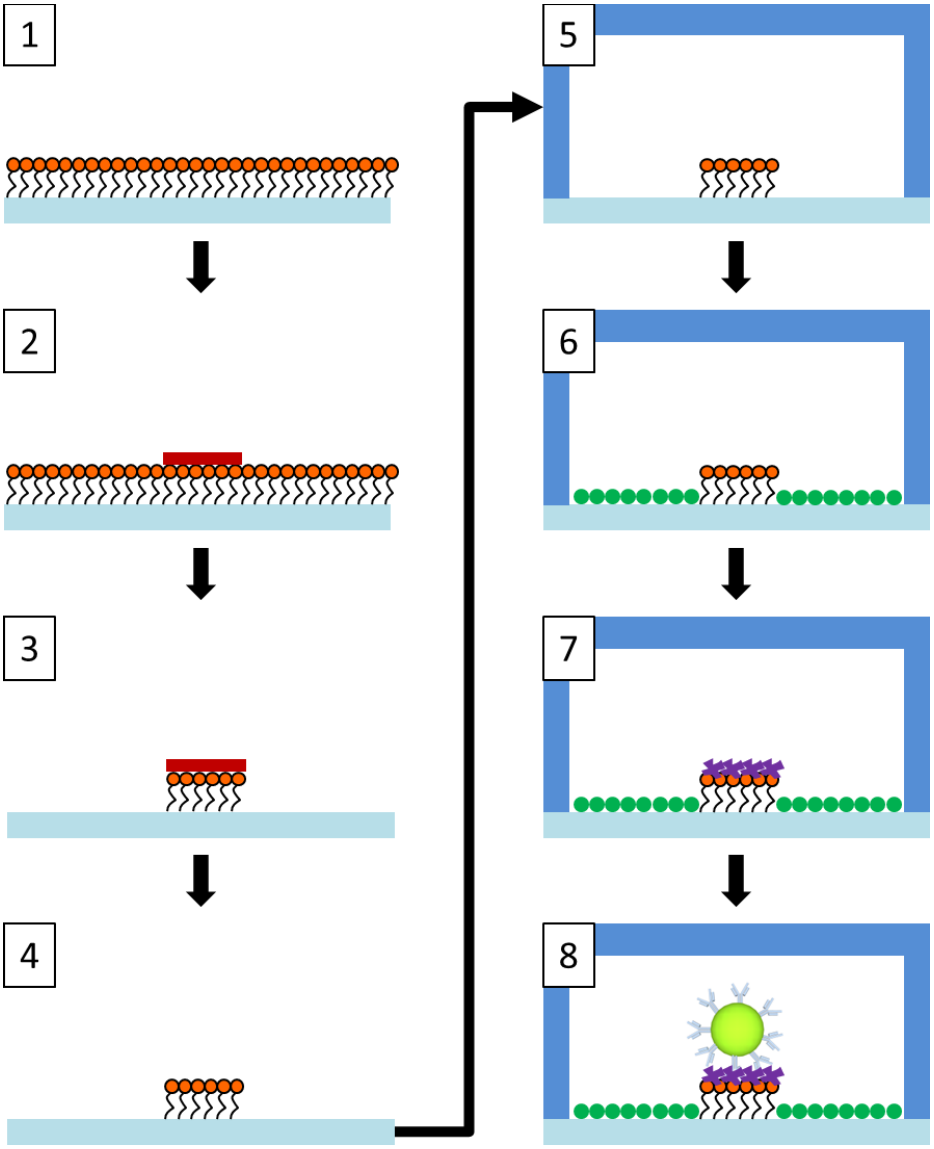

Figure 3-10. Substrate preparation and antibody-conjugated microbead assembly in the PDMS microfluidic devices. (1) The glass substrate is functionalized with biotin-PEG (orange). (2) The microbead binding areas are then photolithographically patterned with a positive photoresist (red). (3) The substrate is exposed to oxygen plasma which serves to destroy any unprotected surface chemistry as well as activate the surface for bonding to PDMS. (4) The patterned photoresist is stripped off the substrate. (5) The PDMS microfluidic channels are aligned and bonded to the substrate. (6) The channel surface is blocked with a protein-free blocking buffer (green circles). (7) A streptavidin (purple) solution is incubated in the channel and binds to the biotin-PEG. (8) Antibody-conjugated microbeads bind to the patterned streptavidin via the extra biotin available on the antibodies.

Strategy for antibody-conjugated microbead assembly

Integration of the high-density antibody-conjugated microbead arrays into the microfluidic device was non-trivial. First and foremost, the use of an electric field for assembly of the array was not optimal and instead a magnetic assembly method was employed. With thick PDMS atop the glass substrate making sensitive imaging from the top impossible, it was imperative that any epifluorescence imaging be done through the glass substrate itself. This meant that having a non-transparent gold electrode upon which the array could be assembled was not an option. While indium-tin oxide (ITO) could possibly be used instead, ITO could degrade and reduce the imaging efficiency and the detection sensitivity. Additionally, by having PDMS as the top substrate meant that counter-electrodes could not be easily fabricated on the fluidic channel ceiling. Alternatively, by using a magnetic assembly approach the glass substrate's transparency could be preserved. However, by selecting a magnetic assembly approach it is required that the substrate surface be chemically modified to allow for the antibody-conjugated microbeads to bind to the surface.

The biggest issue with chemically modified surfaces is the challenge in preserving the surface chemistry while using standard PDMS device assembly methods. The oxygen plasma used to activate the surface damages any exposed molecules and destroys their functionality. To protect the modified surface we use a method of protective patterning as depicted in Figure 3-10. This method is derived from our lab's previous work on destructive patterning[66]. In this method, the glass coverslip surface is functionalized using standard silane chemistry. The surface is activated using a dilute HNO_3 solution and APTES is functionalized on the surface. The free amines on the surfaces are then reacted

with NHS-PEG-biotin molecules. This creates a surface that is densely covered in biotin. In order to protect the biotin from the harmful UV, ozone, and oxygen plasma used to activate the glass and PDMS surfaces, the surface was coated with a positive photoresist and patterned on the areas I wished to have protected (Figure 3-10.3). The only change in the photoresist processing procedure is a lowering of the soft-bake temperature. Generally, the Shipley S1800 series photoresists are soft-baked at 115 ºC for 1 minute, but in order to prevent exposure of the surface chemistry to elevated temperatures the soft-bake step is changed to a 2 minute soft-bake at 80 ºC. However, even with this lowered soft-bake temperature, one must consider the processing temperatures and solutions with regards to surface chemistries involving sensitive molecules such as proteins. Here it is shown that biotin and PEG molecules are compatible with this process.

These methods overcome significant obstacles in producing functionalized surfaces in PDMS microchannels. Others who have functionalized microchannels post-assembly risk the global functionalization of the entire microchannel, including both the substrate surface and the PDMS walls and ceiling. This means that upon loading of a sample, the analytes of interest may bind everywhere. Moreover, if specific patterning is desired it would then require some form of cumbersome patterning within the assembled device. Using the method of protective patterning described here, these problems are avoided because only the glass substrate is functionalized and protected in precise regions. The remaining channel surfaces can be blocked using standard blocking buffers and the analytes of interest will only bind to the patterned regions. This significantly improves the ability to capture and subsequently analyze the molecules of interest.

Altogether these methods show that a thin layer of patterned photoresist is sufficient to protect the underlying pre-functionalized biotin molecules during the UVO activation. The photoresist is then easily removed with 1165 remover to re-expose the surface chemistry. Moreover, the unprotected regions of the substrate have been activated by the oxygen plasma and the PDMS microchannels can be aligned and permanently bonded to the substrate surface.

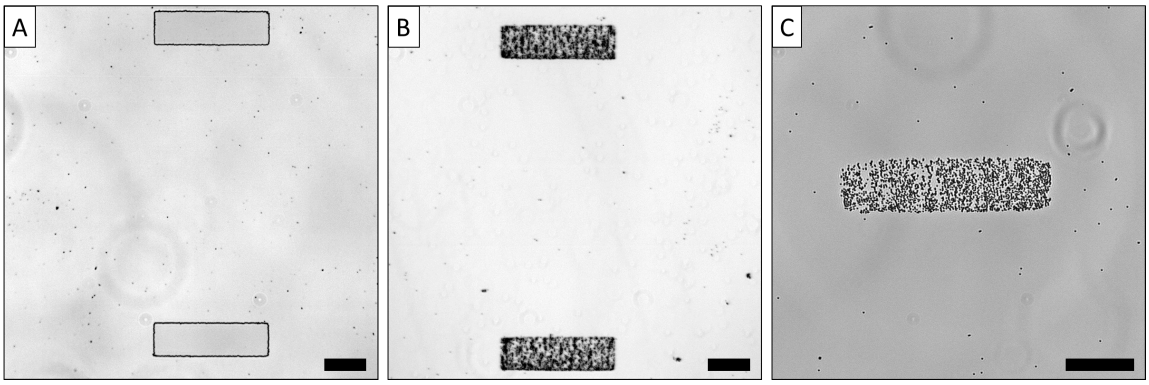

Figure 3-11. Protective patterning of functionalized surfaces and magnetic bead assembly. (A) Image of positive photoresist rectangles patterned atop a carboxyl functionalized glass coverslip. (B) Image of streptavidin-conjugated magnetic microbeads assembled atop a protectively patterned biotin surface. (C) Image of antibody-conjugated microbeads assembled atop a protectively patterned streptavidin surface. Scale bars in each image correspond to 100 μm.

Verification of protective patterning strategy

To verify the effectiveness of the protective patterning strategy coverslips functionalized with biotin were coated with photoresist and patterned as seen in Figure 3-11A. The areas covered by the photoresist are protected during the harmful exposure to UV and oxygen plasma. For these initial tests, channels were formed using double-sided tape and pre-drilled glass slides. To verify that the biotin remained functional, streptavidin-conjugated microbeads were assembled onto the substrate surface as seen in Figure 3-11B. The microbeads assemble directly onto the patterned regions where biotin

remains on the surface. It was crucial to first use a blocking buffer to coat the channel and substrate surface. Any unprotected substrate areas had their chemical functionalities destroyed and the surface was susceptible to non-specific binding of the microbeads if not first blocked.

Additionally, antibody-conjugated microbeads were successfully assembled onto the protectively patterned surfaces as seen in Figure 3-11C. Again, it is clearly evident that the microbeads assemble very well onto the patterned rectangular region with minimal non-specific binding to the remaining substrate. A key step in this process, in addition to blocking the substrate surface, was the incubation of streptavidin in the channel. The streptavidin bound to the biotin functionalized on the substrate surface and essentially created a streptavidin patterned surface. The biotin-labeled antibodies were conjugated to the microbeads by biotin-streptavidin interactions. The antibodies themselves have excess biotin conjugated to them, thereby allowing the antibody-conjugated microspheres to bind to a streptavidin functionalized surface. It is important to reinforce that blocking buffer was used before incubation of the channel with streptavidin. This was to prevent any non-specific binding of the streptavidin protein on the substrate surface. Altogether, these methods allowed for proper assembly of antibody-conjugated microbeads onto the protectively patterned functionalized substrate.

Assembly of antibody-conjugated microbeads in PDMS channels

Following verification of the protective patterning strategy in glass microchannels, antibody-conjugated microbeads were assembled into PDMS microchannels as shown in Figure 3-12. One key step in assembling the PDMS microfluidic channels is ensuring

there is proper alignment such that the protectively patterned areas are positioned into the individual cell capture compartments, as shown in Figure 3-12A. Because the photoresist is removed by sonication in 1165 remover just prior to aligning, one must ensure that there is a set of permanent alignment marks that can be used, such as pre-patterned metal alignment marks. Just as careful consideration of the PDMS shrinkage ratio was important to consider in aligning the metal electrodes, it is also critical to consider when aligning the protectively patterned regions or else they may fall outside of the defined PDMS compartments. While it may seem easier to leave the photoresist on the substrate surface during alignment and bonding and simply remove the photoresist afterwards, this method proved to be ineffectual. As shown in Figure 3-12B, when photoresist was left on the substrate surface during alignment and bonding, 1165 remover which was flowed through the PDMS microchannels failed to fully dissolve and flush away the photoresist even after 6 hours of continuous flushing. Thus, it was determined that complete removal of the photoresist before alignment and bonding was necessary. Additionally, with standard PDMS thermal bonding steps conducted at 80 ºC, the modified surface chemistry is shown to be able to withstand the entire process.

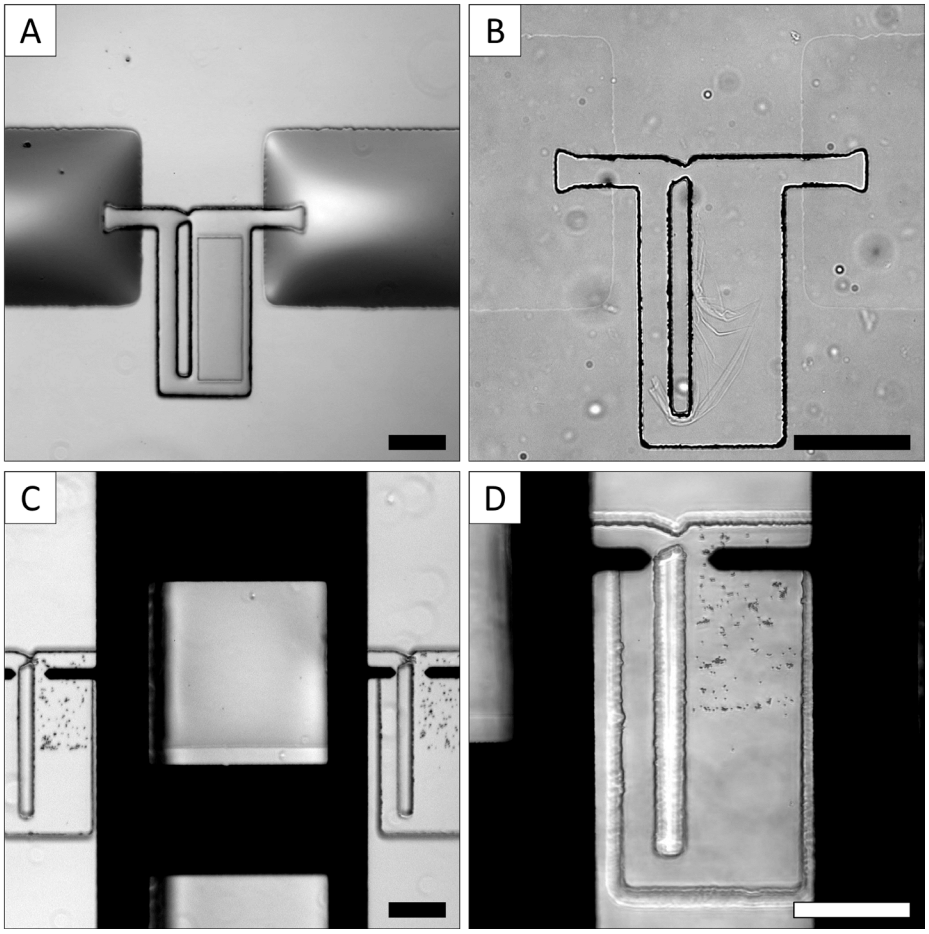

Figure 3-12. Protective patterning and assembly of antibody-conjugated microbeads in PDMS microchannels. (A) Image of photoresist patterned and aligned to a single cell capture compartment in a PDMS device. (B) Remaining photoresist after 6 hours of washing with 1165 photoresist remover. (C) Antibody-conjugated microbeads assembled within the single cell compartments of an assembled PDMS device. Each compartment was only protectively patterned on ½ of its area. (D) Image of the antibody-conjugated microbeads assembled in a single compartment of the PDMS device. Scale bars in each image correspond to 100 μm.

Following bonding of the PDMS to the functionalized substrate the same procedure of surface blocking and streptavidin binding to the patterned biotin-PEG was performed. Antibody-conjugated microbeads were then injected into the microfluidic channels using an infusion syringe pump, pulled down to the surface with a magnet, and assembled onto only the patterned areas with little non-specific assembly on the

unprotected regions of the substrate, as shown in Figure 3-12C and 3-12D. While the assembly is not as dense as in Figure 3-11, this is mainly due to the small number of microbeads in the microchannels. Additionally, it can be seen in Figure 3-12D that the microbeads appear to be clumped together. Over applying the magnet can cause the magnetic microbeads to clump together, so this issue may be resolved by more careful application of the magnet during assembly. Despite these minor issues, we have shown successful assembly of antibody-conjugated microbeads onto protectively patterned functionalized substrate surfaces using methodology that is completely compatible with standard PDMS microfluidic device assembly.

3.4.4 Summary

Antibody-conjugated microbeads were successfully assembled onto protectively patterned, functionalized glass substrate surfaces using a method that is compatible with standard PDMS microfluidic device assembly. Glass substrates were chemically modified with biotin-PEG using conventional silane chemistry and then protectively patterned using photoresist and photolithographic methods. The photoresist layer was sufficient to protect the surface-bound biotin-PEG from the harmful substrate activation (exposure to oxygen plasma in an UVO cleaner) which is necessary for strong permanent bonding of PDMS to the glass substrates. These methods overcome many of the current challenges in assembling PDMS microfluidic devices with patterned and functionalized surfaces. More importantly, these methods present an effective mechanism in which antibody-conjugated microbead arrays may be assembled into the single-cell capture compartments in the

PDMS microfluidic devices. By employing a protective patterning method, along with scalable photolithographic methods which can be used to pattern arrays, a high-density antibody-conjugated microbead array could be assembled into each individual trap compartment and allow for rapid on-chip proteome analysis of a single cell immediately after cell lysis.

3.5 Summary and Future Directions

To overcome the current challenges associated with single cell proteome analysis we have developed high-density antibody-conjugated bead arrays as well as methods for assembling these arrays directly into the single-cell trap compartments in PDMS microfluidic devices. Using standard photolithographic methods, high-density arrays could be fabricated in which antibody-conjugated antibodies were assembled using electric-field directed assembly. Moreover, detection levels in the picomolar range were achieved, which are comparable to the protein concentrations of mid-to-highly expressed proteins from single cells. Such an array of 1.2 μm microbeads assembled at a 2.4 μm pitch means that within a single cell compartment with dimensions of 250 μm by 250 μm, an array of ~10,000 microbeads could be assembled. This could allow for the interrogation of hundreds to thousands of unique proteins in multiplicate.

Methods for integration of such microbead arrays directly into PDMS microfluidic devices were developed using protective photolithographic patterning and were shown to be compatible with standard permanent bonding of PDMS to glass substrates. These methods involved first chemically modifying the glass substrates and

then using photoresist patterns to protect the surface chemistry from the harmful oxygen plasma treatment necessary to activate the substrate surface for PDMS bonding. Following bonding, the photoresist was removed and it was shown that the surface chemistry remained viable. Antibody-conjugated microbeads could be assembled onto the surface using magnetic assembly directly in PDMS single-cell trap compartments with little non-specific binding in unprotected regions. Additionally, by incorporating each array directly into the single cell trap compartments, there is no loss of sample and analytes remain at a high concentration. Altogether, these methodologies provide a novel solution for single cell proteome analysis directly on-chip in the single-cell analysis devices.

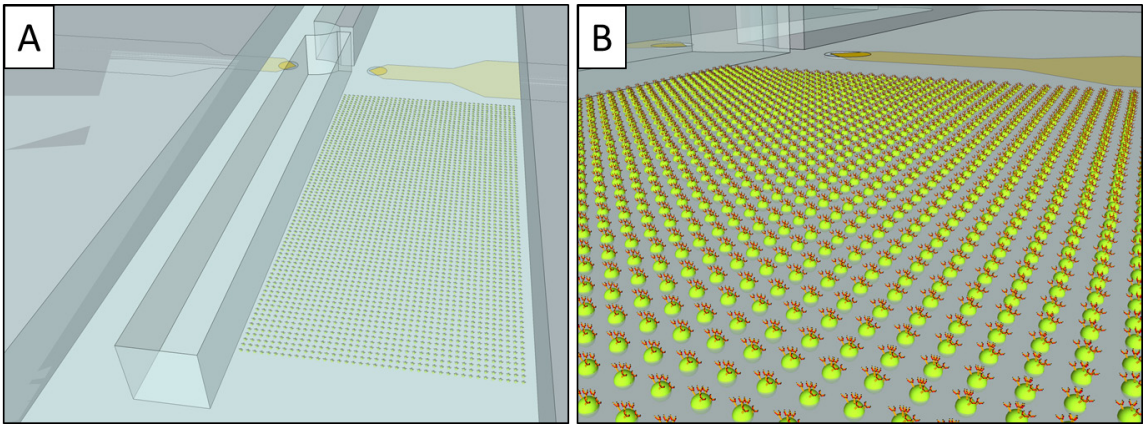

Figure 3-13. Incorporation of high-density antibody-microbead arrays into the single-cell analysis compartments. (A) Using protective patterning and magnetic bead assembly high-density antibody-conjugated microbead arrays can be assembled directly into the single-cell capture compartments. (B) The high-density arrays will enable analysis of thousands of proteins directly from each single-cell with no sample loss.

Future work will focus on incorporating the protective patterning methods to assemble high-density microbead arrays within each compartment, as shown in Figure 3-13. Additionally, a significant challenge will be finding sensitive antibody pairs that are

capable of detecting proteins at single cell concentrations which may range from low picomolar to femtomolar. To truly interrogate the entire proteome, microbead encoding strategies will also need to improve and may require a combination of fluorescent and spatial encoding. Nonetheless, the current work discussed in this chapter is a significant step in developing new technologies for analyzing the entire proteome from single cells directly on-chip in PDMS devices.

3.6 Acknowledgements

This work was supported in part by grants from the NIH/NHGRI (R21HG004130 and R01HG004084) and the NSF under a CAREER award to X. H. (BES-0547193). A portion of this work was conducted at the Triangle National Lithography Center at North Carolina State University (NCSU). We thank David Vellenga and Marcio Cerullo at NCSU for their training, technical support and services, which included DUV photolithography and BARC etching. A portion of this work was done in the nanofabrication facility at the University of California, Santa Barbara (UCSB), part of the NSF funded NNIN network. We thank Dr. Brian Thibeault for training and technical support at UCSB. Part of this work was also performed in the Nano3 facility at CalIT^2 at the University of California, San Diego (UCSD). We thank Michael Clark for dicing our wafers and Larry Grissom and Ryan Anderson for training and technical support at UCSD. We also thank Nora Theilacker for advice and assistance with antibodies, antibody-microbead conjugation and assembly strategies, and image analysis routines.

Chapter 3, in part is a reprint of the material as it appears in: Barbee, K.D., Hsiao, A.P., Roller, E.E., Huang, X. Multiplexed Protein Detection Using Antibody-conjugated Microbead Arrays in a Microfabricated Electrophoretic Device. *Lab on a Chip*, 10 (22), 3084-3093 (2010). The dissertation author was a co-author of this publication.

3.7 References

1. L. Cai, N. Friedman and X. S. Xie, "Stochastic protein expression in individual cells at the single molecule level," *Nature*, vol. 440, no. 7082, pp. 358-362 (2006)

2. M. B. Elowitz, A. J. Levine, E. D. Siggia and P. S. Swain, "Stochastic gene expression in a single cell," *Science*, vol. 297, no. 5584, pp. 1183-6 (2002)

3. B. Huang, H. Wu, D. Bhaya, A. Grossman, S. Granier, B. K. Kobilka and R. N. Zare, "Counting low-copy number proteins in a single cell," *Science*, vol. 315, no. 5808, pp. 81-4 (2007)

4. J. R. S. Newman, S. Ghaemmaghami, J. Ihmels, D. K. Breslow, M. Noble, J. L. DeRisi and J. S. Weissman, "Single-cell proteomic analysis of S. cerevisiae reveals the architecture of biological noise," *Nature*, vol. 441, no. 7095, pp. 840-846 (2006)

5. D. R. Bandura, V. I. Baranov, O. I. Ornatsky, A. Antonov, R. Kinach, X. Lou, S. Pavlov, S. Vorobiev, J. E. Dick and S. D. Tanner, "Mass cytometry: technique for real time single cell multitarget immunoassay based on inductively coupled plasma time-of-flight mass spectrometry," *Analytical Chemistry*, vol. 81, no. 16, pp. 6813-22 (2009)

6. S. C. Bendall, E. F. Simonds, P. Qiu, A. D. Amir el, P. O. Krutzik, R. Finck, R. V. Bruggner, R. Melamed, A. Trejo, O. I. Ornatsky, R. S. Balderas, S. K. Plevritis, K. Sachs, D. Pe'er, S. D. Tanner and G. P. Nolan, "Single-cell mass cytometry of differential immune and drug responses across a human hematopoietic continuum," *Science*, vol. 332, no. 6030, pp. 687-96 (2011)

7. P. O. Krutzik and G. P. Nolan, "Intracellular phospho-protein staining techniques for flow cytometry: Monitoring single cell signaling events," *Cytometry Part A*, vol. 55A, no. 2, pp. 61-70 (2003)

8. S. P. Perfetto, P. K. Chattopadhyay and M. Roederer, "Innovation - Seventeen-colour flow cytometry: unravelling the immune system," *Nature Reviews Immunology*, vol. 4, no. 8, pp. 648-U5 (2004)

9. R. Fan, O. Vermesh, A. Srivastava, B. K. Yen, L. Qin, H. Ahmad, G. A. Kwong, C. C. Liu, J. Gould, L. Hood and J. R. Heath, "Integrated barcode chips for rapid, multiplexed analysis of proteins in microliter quantities of blood," *Nat Biotechnol*, vol. 26, no. 12, pp. 1373-8 (2008)

10. C. Ma, R. Fan, H. Ahmad, Q. Shi, B. Comin-Anduix, T. Chodon, R. C. Koya, C. C. Liu, G. A. Kwong, C. G. Radu, A. Ribas and J. R. Heath, "A clinical microchip for evaluation of single immune cells reveals high functional heterogeneity in phenotypically similar T cells," *Nat Med*, vol. 17, no. 6, pp. 738-43 (2011)

11. B. K. McKenna, J. G. Evans, M. C. Cheung and D. J. Ehrlich, "A parallel microfluidic flow cytometer for high-content screening," *Nat Methods*, vol. 8, no. 5, pp. 401-3 (2011)

12. B. K. McKenna, A. A. Selim, F. Richard Bringhurst and D. J. Ehrlich, "384-channel parallel microfluidic cytometer for rare-cell screening," *Lab Chip*, vol. 9, no. 2, pp. 305-10 (2009)

13. J. S. Mellors, K. Jorabchi, L. M. Smith and J. M. Ramsey, "Integrated microfluidic device for automated single cell analysis using electrophoretic separation and electrospray ionization mass spectrometry," *Analytical Chemistry*, vol. 82, no. 3, pp. 967-73 (2010)

14. A. Salehi-Reyhani, J. Kaplinsky, E. Burgin, M. Novakova, A. J. deMello, R. H. Templer, P. Parker, M. A. A. Neil, O. Ces, P. French, K. R. Willison and D. Klug, "A first step towards practical single cell proteomics: a microfluidic antibody capture chip with TIRF detection," *Lab on a Chip*, vol. 11, no. 7, pp. 1256-1261 (2011)

15. H. Makamba, J. H. Kim, K. Lim, N. Park and J. H. Hahn, "Surface modification of poly(dimethylsiloxane) microchannels," *Electrophoresis*, vol. 24, no. 21, pp. 3607-3619 (2003)

16. C. Priest, "Surface patterning of bonded microfluidic channels," *Biomicrofluidics*, vol. 4, no. 3, pp. (2010)

17. L. Wang, L. Lei, X. F. Ni, J. Shi and Y. Chen, "Patterning bio-molecules for cell attachment at single cell levels in PDMS microfluidic chips," *Microelectronic Engineering*, vol. 86, no. 4-6, pp. 1462-1464 (2009)

18. A. Pandey and M. Mann, "Proteomics to study genes and genomes," *Nature*, vol. 405, no. 6788, pp. 837-846 (2000)

19. G. MacBeath, "Protein microarrays and proteomics," *Nat. Genet.*, vol. 32, no. pp. 526-32 Suppl (2002)

20. E. Phizicky, P. I. H. Bastiaens, H. Zhu, M. Snyder and S. Fields, "Protein analysis on a proteomic scale," *Nature*, vol. 422, no. 6928, pp. 208-215 (2003)

21. J. Madoz-Gúrpide, H. Wang, D. E. Misek, F. Brichory and S. M. Hanash, "Protein based microarrays: A tool for probing the proteome of cancer cells and tissues," *Proteomics*, vol. 1, no. 10, pp. 1279-1287 (2001)

22. V. Knezevic, C. Leethanakul, V. E. Bichsel, J. E. Worth, V. V. Prabhu, J. S. Gutkind, L. A. Liotta, P. J. Munson, E. F. Petricoin III and D. B. Krizman, "Proteomic profiling of the cancer microenvironment by antibody arrays," *Proteomics*, vol. 1, no. 10, pp. 1271-1278 (2001)

23. R. Bellisario, R. J. Colinas and K. A. Pass, "Simultaneous measurement of antibodies to three HIV-1 antigens in newborn dried blood-spot specimens using a multiplexed microsphere-based immunoassay," *Early Hum. Dev.*, vol. 64, no. 1, pp. 21-25 (2001)

24. J. Burbaum and G. M. Tobal, "Proteomics in drug discovery," *Curr. Opin. Chem. Biol.*, vol. 6, no. 4, pp. 427-433 (2002)

25. J. Renart, J. Reiser and G. R. Stark, "Transfer of proteins from gels to diazobenzyloxymethyl-paper and detection with antisera: a method for studying antibody specificity and antigen structure," *Proc. Natl. Acad. Sci. U. S. A.*, vol. 76, no. 7, pp. 3116-3120 (1979)

26. E. Engvall and P. Perlmann, "Enzyme-linked immunosorbent assay (ELISA) quantitative assay of immunoglobulin G," *Immunochemistry*, vol. 8, no. 9, pp. 871-874 (1971)

27. J. W. Silzel, B. Cercek, C. Dodson, T. Tsay and R. J. Obremski, "Mass-sensing, multianalyte microarray immunoassay with imaging detection," *Clin. Chem.*, vol. 44, no. 9, pp. 2036-2043 (1998)

28. P. Arenkov, A. Kukhtin, A. Gemmell, S. Voloshchuk, V. Chupeeva and A. Mirzabekov, "Protein microchips: use for immunoassay and enzymatic reactions," *Anal. Biochem.*, vol. 278, no. 2, pp. 123 - 131 (2000)

29. G. MacBeath and S. L. Schreiber, "Printing proteins as microarrays for high-throughput function determination," *Science*, vol. 289, no. pp. 1760 - 1763 (2000)

30. R. M. T. de Wildt, C. R. Mundy, B. D. Gorick and I. M. Tomlinson, "Antibody arrays for high-throughput screening of antibody-antigen interactions," *Nat. Biotechnol.*, vol. 18, no. 9, pp. 989 - 994 (2000)

31. L. J. Holt, K. Bussow, G. Walter and I. M. Tomlinson, "By-passing selection: direct screening for antibody-antigen interactions using protein arrays," *Nucleic Acids Res.*, vol. 28, no. 15, pp. e72- (2000)

32. H. Zhu, M. Bilgin, R. Bangham, D. Hall, A. Casamayor, P. Bertone, N. Lan, R. Jansen, S. Bidlingmaier, T. Houfek, T. Mitchell, P. Miller, R. A. Dean, M. Gerstein and M. Snyder, "Global Analysis of Protein Activities Using Proteome Chips," *Science*, vol. 293, no. 5537, pp. 2101-2105 (2001)

33. M. D. Moody, S. W. Van Arsdell, K. P. Murphy, S. F. Orencole and C. Burns, "Array-based ELISAs for high-throughput analysis of human cytokines.," *Biotechniques*, vol. no. 1, pp. 186-94 (2001)

34. B. B. Haab, M. J. Dunham and P. O. Brown, "Protein microarrays for highly parallel detection and quantitation of specific proteins and antibodies in complex solutions," *Genome Biology*, vol. 2, no. 2, pp. 0004.1-0004.13 (2001)

35. R.-P. Huang, R. Huang, Y. Fan and Y. Lin, "Simultaneous Detection of Multiple Cytokines from Conditioned Media and Patient's Sera by an Antibody-Based Protein Array System," *Anal. Biochem.*, vol. 294, no. 1, pp. 55-62 (2001)

36. J. Dasso, J. Lee, H. Bach and R. G. Mage, "A comparison of ELISA and flow microsphere-based assays for quantification of immunoglobulins," *J. Immunol. Methods*, vol. 263, no. 1-2, pp. 23-33 (2002)

37. K. L. Kellar and M. A. Iannone, "Multiplexed microsphere-based flow cytometric assays," *Exp. Hematol.*, vol. 30, no. 11, pp. 1227-1237 (2002)

38. A. Goodey, J. J. Lavigne, S. M. Savoy, M. D. Rodriguez, T. Curey, A. Tsao, G. Simmons, J. Wright, S.-J. Yoo, Y. Sohn, E. V. Anslyn, J. B. Shear, D. P. Neikirk and J. T. McDevitt, "Development of Multianalyte Sensor Arrays Composed of Chemically Derivatized Polymeric Microspheres Localized in Micromachined Cavities," *J. Am. Chem. Soc.*, vol. 123, no. 11, pp. 2559-2570 (2001)

39. M. Herrmann, E. Roy, T. Veres and M. Tabrizian, "Microfluidic ELISA on non-passivated PDMS chip using magnetic bead transfer inside dual networks of channels," *Lab Chip*, vol. 7, no. 11, pp. 1546-52 (2007)

40. A. H. Diercks, A. Ozinsky, C. L. Hansen, J. M. Spotts, D. J. Rodriguez and A. Aderem, "A microfluidic device for multiplexed protein detection in nano-liter volumes," *Anal. Biochem.*, vol. 386, no. 1, pp. 30-35 (2009)

41. X. Qiu, J. A. Thompson, Z. Chen, C. Liu, D. Chen, S. Ramprasad, M. Mauk, S. Ongagna, C. Barber, W. R. Abrams, D. Malamud, P. L. A. M. Corstjens and H. H. Bau, "Finger-actuated, self-contained immunoassay cassettes," *Biomed. Microdev.*, vol. 11, no. 6, pp. 1175-1186 (2009)

42. T. M. Blicharz, W. L. Siqueira, E. J. Helmerhorst, F. G. Oppenheim, P. J. Wexler, F. F. Little and D. R. Walt, "Fiber-optic microsphere-based antibody array for the analysis of inflammatory cytokines in saliva," *Anal. Chem.*, vol. 81, no. 6, pp. 2106-2114 (2009)

43. V. Sivagnanam, B. Song, C. Vandevyver and M. A. M. Gijs, "On-Chip Immunoassay Using Electrostatic Assembly of Streptavidin-Coated Bead Micropatterns," *Anal. Chem.*, vol. 81, no. 15, pp. 6509-6515 (2009)

44. C. J. Easley, J. M. Karlinsey, J. M. Bienvenue, L. A. Legendre, M. G. Roper, S. H. Feldman, M. A. Hughes, E. L. Hewlett, T. J. Merkel, J. P. Ferrance and J. P. Landers, "A fully integrated microfluidic genetic analysis system with sample-in-answer-out capability," *Proc. Natl. Acad. Sci. U. S. A.*, vol. 103, no. 51, pp. 19272-19277 (2006)

45. J. F. Zhong, Y. Chen, J. S. Marcus, A. Scherer, S. R. Quake, C. R. Taylor and L. P. Weiner, "A microfluidic processor for gene expression profiling of single human embryonic stem cells," *Lab Chip*, vol. 8, no. 1, pp. 68-74 (2008)

46. K. L. Ewalt, R. W. Haigis, R. Rooney, D. Ackley and M. Krihak, "Detection of biological toxins on an active electronic microchip," *Anal. Biochem.*, vol. 289, no. 2, pp. 162-72 (2001)

47. V. N. Morozov, S. Groves, M. J. Turell and C. Bailey, "Three Minutes-Long Electrophoretically Assisted Zeptomolar Microfluidic Immunoassay with Magnetic-Beads Detection," *J. Am. Chem. Soc.*, vol. 129, no. 42, pp. 12628-12629 (2007)

48. J. Wu, Y. Yan, F. Yan and H. Ju, "Electric Field-Driven Strategy for Multiplexed Detection of Protein Biomarkers Using a Disposable Reagentless Electrochemical Immunosensor Array," *Anal. Chem.*, vol. 80, no. 15, pp. 6072-6077 (2008)

49. J. K. Ng, E. S. Selamat and W.-T. Liu, "A spatially addressable bead-based biosensor for simple and rapid DNA detection," *Biosens. Bioelectron.*, vol. 23, no. 6, pp. 803-810 (2008)

50. K. L. Michael, L. C. Taylor, S. L. Schultz and D. R. Walt, "Randomly Ordered Addressable High-Density Optical Sensor Arrays," *Anal. Chem.*, vol. 70, no. 7, pp. 1242-1248 (1998)

51. M. Han, X. Gao, J. Z. Su and S. Nie, "Quantum-dot-tagged microbeads for multiplexed optical coding of biomolecules," *Nat. Biotechnol.*, vol. 19, no. 7, pp. 631-635 (2001)

52. K. L. Gunderson, S. Kruglyak, M. S. Graige, F. Garcia, B. G. Kermani, C. Zhao, D. Che, T. Dickinson, E. Wickham, J. Bierle, D. Doucet, M. Milewski, R. Yang, C. Siegmund, J. Haas, L. Zhou, A. Oliphant, J.-B. Fan, S. Barnard and M. S. Chee, "Decoding Randomly Ordered DNA Arrays," *Genome Res.*, vol. 14, no. 5, pp. 870-877 (2004)

53. S. Birtwell and H. Morgan, "Microparticle encoding technologies for high-throughput multiplexed suspension assays," *Integr. Biol.*, vol. 1, no. 5-6, pp. 345-362 (2009)

54. K. D. Barbee, A. P. Hsiao, M. J. Heller and X. Huang, "Electric field directed assembly of high-density microbead arrays," *Lab Chip*, vol. 9, no. pp. 3268-3274 (2009)

55. G. Folcher, H. Cachet, M. Froment and J. Bruneaux, "Anodic corrosion of indium tin oxide films induced by the electrochemical oxidation of chlorides," *Thin Solid Films*, vol. 301, no. 1-2, pp. 242-248 (1997)

56. M. D. Abramoff, P. J. Magelhaes and S. J. Ram, "Image processing with ImageJ," *Biophotonics Intl.*, vol. 11, no. 7, pp. 36-42 (2004)

57. D. J. Anderson, "Determination of the lower limit of detection," *Clin. Chem.*, vol. 35, no. 10, pp. 2152-2153 (1989)

58. A. Hucknall, D.-H. Kim, S. Rangarajan, R. T. Hill, W. M. Reichert and A. Chilkoti, "Simple Fabrication of Antibody Microarrays on Nonfouling Polymer Brushes with Femtomolar Sensitivity for Protein Analytes in Serum and Blood," *Adv. Mater.*, vol. 21, no. 19, pp. 1968-1971 (2009)

59. P. Jain, G. L. Baker and M. L. Bruening, "Applications of Polymer Brushes in Protein Analysis and Purification," *Ann. Rev. Anal. Chem.*, vol. 2, no. 1, pp. 387-408 (2009)

60. I. L. Medintz, H. T. Uyeda, E. R. Goldman and H. Mattoussi, "Quantum dot bioconjugates for imaging, labelling and sensing," *Nat. Mater.*, vol. 4, no. 6, pp. 435-46 (2005)

61. B. Schweitzer, S. Wiltshire, J. Lambert, S. O'Malley, K. Kukanskis, Z. Zhu, S. F. Kingsmore, P. M. Lizardi and D. C. Ward, "Immunoassays with rolling circle DNA amplification: A versatile platform for ultrasensitive antigen detection," *Proc. Natl. Acad. Sci. U. S. A.*, vol. 97, no. 18, pp. 10113-10119 (2000)

62. N. V. Dziomkina, M. A. Hempenius and G. J. Vancso, "Symmetry Control of Polymer Colloidal Monolayers and Crystals by Electrophoretic Deposition on Patterned Surfaces," *Adv. Mater.*, vol. 17, no. 2, pp. 237-240 (2005)

63. M. Trau, D. A. Saville and I. A. Aksay, "Assembly of Colloidal Crystals at Electrode Interfaces," *Langmuir*, vol. 13, no. 24, pp. 6375-6381 (1997)

64. B. Cordovez, D. Psaltis and D. Erickson, "Trapping and storage of particles in electroactive microwells," *Appl. Phys. Lett.*, vol. 90, no. 2, pp. 024102 (2007)

65. K. D. Barbee and X. H. Huang, "Magnetic assembly of high-density DNA arrays for genomic analyses," *Analytical Chemistry*, vol. 80, no. 6, pp. 2149-2154 (2008)

66. K. D. Barbee, M. Chandrangsu and X. Huang, "Fabrication of DNA polymer brush arrays by destructive micropatterning and rolling-circle amplification," *Macromol Biosci*, vol. 11, no. 5, pp. 607-17 (2011)

4 METHODS FOR SINGLE-CELL GENE EXPRESSION PROFILING

4.1 Abstract

Elucidating the entire gene expression profile, or transcriptome, from single cells provides for a powerful tool in uncovering subpopulations of cells and revealing subtle differences in transcription that may play key roles in cellular development, differentiation, response to drugs, or progression of disease. In this chapter, I present strategies and methods for implementing gene expression profiling from many single cells directly in the PDMS microfluidic device. Methods for quantitatively capturing single-cell mRNA on pre-functionalized and protectively patterned glass surfaces directly in PDMS microchannels is presented. Additionally, I present results of mRNA capture kinetics indicating that quantitative mRNA capture is possible in minutes directly on-chip. Single, covalently bound cDNA molecules can then be generated directly on the substrate surface. Transcripts could be digitally enumerated by single-molecule sequencing methods. Altogether, these methods present a potential technology capable of digital identification of the entire transcriptome from many single cells within the integrated PDMS microfluidic device.

4.2 Introduction

Gene expression varies greatly amongst individual cells, even within a population of the same cell type[1-12]. These differences may be attributed to stochastic variation at the transcription and translational level, but could also play a role in changes to cellular states. These subtle differences amongst a population of cells may in fact play key roles in areas such as development, differentiation, or progression of diseases such as cancer[13, 14]. The transcriptional profile of a cell serves as a signature of its functional state and can be regarded as a measure of the biological identity of a particular cell or class of cells. The ability for comprehensive transcription profiling at the single-cell level is essential to measure cellular heterogeneity and to precisely define cell types. This will allow us to characterize rare cells such as early-stage cancer cells and stem cells. Analysis of cells in bulk is insufficient, thus it is imperative that single-cell technologies be created which can further identify these minute transcriptional differences.

Traditional analysis of mRNA transcripts is limited in its throughput as well as sensitivity. Methods such as *in situ* hybridization or flow-cytometry, though functional directly at the single cell level, can only analyze a small number of transcripts at one time[15-17]. Other methods such as quantitative PCR and microarray analysis both require amplification and are less effective at single-cell levels[18-21]. The most effective method of comprehensive analysis involves state-of-the-art sequencing technology. Currently available technologies using these methods, such as RNA-seq using high throughput sequencing technologies, require many cells or amplification of the transcripts from

single cells[22]. This has limitations in that it is well known that the amplification step introduces bias and significant sample loss[12, 13].

To minimize sample loss and keep single-cell mRNA concentrations high during reactions, microfluidic approaches have been developed[23-28]. While these methods have shown steps towards increased sensitivity in single-cell analysis, they often perform only the mRNA capture and cDNA synthesis on-chip. Downstream steps are conducted off-chip and still require amplification and detection by sequencing, microarray, or PCR. Thus, there is still significant risk of sample loss and disproportionate amplification. A solution to this loss of signal from low copy number transcripts involves direct single-molecule sequencing[29]. The ideal device would be able to capture mRNA and analyze the transcripts all on-chip with minimal movement of the sample. To date, there has only been one instance of direct mRNA sequencing by Helicos, but their methods do not support single-cell analysis[30].

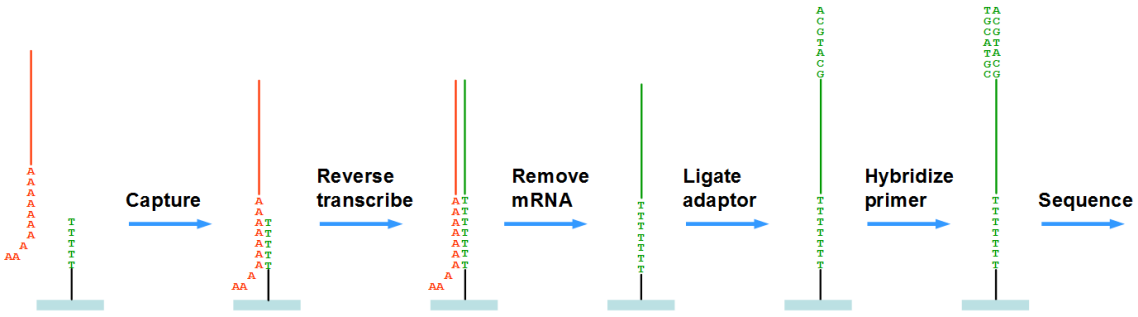

Figure 4-1. Single cell mRNA capture and analysis methodology. mRNA from single cells will be captured by hybridization of the 3'-polyA tails to pre-functionalized polyT DNA on the substrate surface. cDNA will be generated by reverse transcription and will generate a covalently bound single-cell cDNA library on the surface. After ligation of a known sequence adaptor, transcripts will be identified using single-molecule sequencing methods

Here I present methods for integrating the single-cell PDMS microfluidic device with on-chip processing and capturing of single-cell mRNA transcripts. Analysis of the

mRNA transcripts within the single-cell analysis device will follow the steps outlined in Figure 4-1. Briefly, mRNA must be captured onto a pre-functionalized surface, converted to cDNA, and finally identified using single-molecule sequencing methods. These methods follow similarly to those by Ozsolak *et al*[31]. However, Ozsolak *et al*. methods required hundreds of cells, were performed on a Helicos flowcell, and do not yet support single-cell analysis.

It is extremely crucial that the mRNA capture step result in quantitative capture of each transcript. Only then will enumeration of each transcript provide an accurate and unbiased profile from each cell. Thus, the work in this chapter focuses on obtaining quantitative mRNA capture directly in PDMS microchannels, which has not yet been shown. These methods, like those in Chapter 3, include surface functionalization and protective patterning to generate a polyT surface in a manner compatible with PDMS device assembly. It is then shown that this surface is not only clean enough for single-molecule imaging, but can support quantitative capture of mRNA directly from HeLa cells at single-cell concentrations. Ultimately, these methods will be integrated into the PDMS single-cell analysis devices and allow for quantitative capture and detection of mRNA transcripts from single-cells.

4.3 Experimental Methods

Alignment mark fabrication on coverslips

Coverglass substrates (50x50 mm, #1.5 thickness, Fisher) were first cleaned in batch mode by submerging a rack of coverslips into a 2% Micro-90 detergent solution

and sonicating for 15 minutes. The coverslips were then thoroughly rinsed with dH_2O and stored in dH_2O until further use. In the clean room the coverslips were transferred to a custom-built PTFE rack and then immersed into a solution of Piranha Etch (3:1 H_2SO_4:H_2O_2, CAUTION, EXTREMELY DANGEROUS!) and placed into a water bath at 80 ºC for 1 hour to remove any remaining organic residues. Afterwards, the coverslips were rinsed in dH_2O extensively and stored in dH_2O until use.

Cleaned coverslips were dried by nitrogen air gun and dehydration baked on a hotplate at 150 ºC for 10 minutes. Substrates were then spin-coated with Futurrex NR9-1500 negative-tone photoresist (Futurrex, Inc.) at 4000 rpm and soft-baked for 1 minute at 150 ºC. Using a custom designed transparency photomask (FineLine Imaging), the substrates were exposed on a Karl Suss MA6 mask aligner for 81.8 seconds at 11 mW/cm^2. Following UV exposure, the photoresist underwent a post-exposure bake at 100 ºC for 1 minute and then was developed in Resist Developer 6 (RD6, Futurrex) by dipping for 6 seconds followed by rinsing in dH_2O.

Following photoresist patterning, the substrates were coated with titanium (Ti) and gold (Au) on a Denton Discovery 18 sputter system. A 10 nm-thick Ti film and a 200 nm-thick Au film were sputtered at 150 W and 200 W respectively, and at 3.0×10^{-3} Torr Ar at 36-38 sccm. Unwanted photoresist and metal was then removed by lift-off in acetone in an ultrasonic water bath. Substrates were finally rinsed extensively in clean acetone and methanol before being dried in a vacuum desiccator where they were stored until further use.

Chemical surface modification of glass coverslips

Stock coverglass substrates were first cleaned by rinsing briefly in a 2% Micro-90 detergent solution. The substrates were then immersed in acetone and placed into an ultrasonic water bath for 15 minutes. The solution was exchanged with methanol and the substrates sonicated for an additional 15 minutes before a final rinse with dH_2O. Coverslips with fabricated metal alignment marks did not require this initial set of cleaning steps.

The substrate surfaces were activated by immersing in 14% nitric acid for a minimum of 1 hour. The substrates were subsequently rinsed with dH_2O and dried with an argon air gun. A 2% solution of 3-aminopropyltriethoxysilane (APTES, Fisher) in 95% ethanol was prepared and let to sit for 5 minutes before the glass substrates were immersed into the solution for 5 minutes. The substrates were then washed with acetone before drying in a 110 ºC oven for 10 minutes. A 1 mM bi-functional carboxyl-PEG (CM-PEG-CM, MW 1000, Laysan Bio.) solution was prepared in dimethylformamide (DMF) with 5 mM triethylamine and 10 mM EDC-HCl (Advanced ChemTech, Inc.). A small volume of 100 µL of this solution was then pipetted onto one glass substrate and another substrate was inverted and placed onto the first to sandwich the solution in between. This allowed functionalization of two substrates simultaneously. The substrates were placed into a humid dish and allowed to incubate at room temperature for a minimum of 2 hours. Next, the substrates were taken apart and each rinsed in acetone and dried with an argon air gun or by vacuum desiccator. Immediately after, a 25 mM solution of MS-PEG4 (Thermo Fisher Scientific) in DMF with 5 mM triethylamine was prepared and sandwiched between the two coverslip substrates as before. This step

allowed any unreacted carboxyl groups on the surface to be converted to a methyl-PEG molecule. After reacting at room temperature for a minimum of 1 hour, the substrates were again washed in acetone followed by methanol, and finally dried in a vacuum desiccator where they were stored until use.

PDMS mold and device fabrication

All PDMS channel and valve layer molds were fabricated as stated in Chapter 2. Additionally, all PDMS fabrication follows the methods outlined in Chapter 2 as well. Alignment marks were patterned to ensure alignment to the protectively patterned substrate regions.

Protective patterning and PDMS microchannel bonding

Functionalized glass substrates were spin-coated with Shipley S1805 positive-tone photoresist (Microposit) at 4000 rpm and then soft-baked at 80 ºC for 2 minutes. Using a custom designed transparency photomask (FineLine Imaging) the mask was aligned to the pre-fabricated metal alignment marks and exposed using a Karl Suss MA6 mask aligner for 10 seconds at 11 mW/cm^2. Following exposure, the photoresist was developed away using MF-319 or MF-321 developer by immersion for 60 seconds followed by rinsing in dH_2O. The substrates were finally dried by nitrogen air gun.

The glass coverslips, along with pre-fabricated PDMS channels and valves, were activated by exposure to oxygen plasma in a UVO cleaner (Jelight) for 4 minutes. Immediately after activation, the glass substrates were submerged in 1165 remover (Microposit) and sonicated for 5 minutes to remove the protective photoresist layer.

Substrates were then thoroughly rinsed in dH_2O and methanol, and finally dried by argon air gun. These steps must be performed without delay because the surface activation decays with time. Next, the PDMS channels and valves are aligned to the substrate on a custom built alignment system and permanently bonded by placing into an 80 ºC oven for a minimum of 2 hours. Assembled devices were stored in a vacuum desiccator until use.

Poly-T surface modification

Just before use in experiments, PDMS microchannels were injected with a solution of 5 μM NH_2-polyT single-stranded DNA (5'-NH_2-T_{50}-3', Integrated DNA Technologies) and 10 mM EDC in 100 mM (*N*-morpholino)ethanesulfonic acid (MES, pH 5.0) using either a syringe pump (Cavro XR Rocket Pump, Tecan Group) at 5 μL/s injection rate or an infusion syringe pump (Chemyx) at 10 μL/hr infusion rate. Higher flow rates were used in linear PDMS channels whereas the slower flow rate was used in the single-cell capture devices. The NH_2-polyT was allowed to react in the microchannels at room temperature for at least 2 hours. Subsequently, the microchannels were flushed with 2X salt-sodium citrate with 0.02% Tween-20 (SSCT) buffer.

Synthetic mRNA preparation

Plasmid DNA carrying the inserted gene encoding phi29 DNA polymerase was extracted from *E. coli* and purified. After linearization by restriction enzymes, a 30-cycle PCR was performed to amplify the inserted gene with a primer designed to include a 150-base long poly-d(T) tail. This creates a coding strand DNA with a 150-base long d(T) tail at the 3' –end.

In vitro transcription followed using the PCR DNA product as a template with HiScribe™ T7 *in vitro* Transcription Kit (New England Biolabs) according to the manufacturer's specifications. Fluorescein-12-UTP (Enzo Life Sciences) was added into the transcription reaction at two different concentrations: either 2% or 10% of the total UTP concentration. The reaction mix was treated with DNase-I to digest all the DNA after transcription and the remaining mRNA containing the 150-base poly(A) tail (mRNA-150A) was purified by a MEGAclear Kit (Ambion). Murine RNase inhibitor was added into the mRNA-150A product to protect it from degradation.

Denaturing 1.2% agarose gel electrophoresis of the mRNA was used to analyze the purity and integrity of the fluorescent mRNA product. This was done by applying glyoxal into the gel and running buffer and then loading glyoxylated mRNA.

Verification of surface chemistry and protective patterning

Initial tests of the surface chemistry and ability to capture mRNA were performed in simple 15 mm long by 250 μm wide, straight PDMS microchannels with no valve layer. The protective photoresist pattern was either a pattern consisting of 150 μm by 100 μm rectangles at a pitch of 200 μm or a rectangular mask 10 mm long by 150 μm wide which masked the entire fluidic channel surface. The surface molecules under the patterned photoresist were protected during UVO exposure and should bind mRNA while the rest of the channel served as a built-in negative control.

Following polyT functionalization in the PDMS channels, a solution of 0.5 μM 25-mer polyA oligo conjugated to Cy5 (Integrated DNA Technologies) in 2X SSCT was injected into the channel by syringe pump. The oligo was allowed to hybridize at room

temperature for 15 minutes and then the channels were flushed with 2X SSCT buffer. Channel surfaces were imaged using total internal reflection fluorescence (TIRF) microscopy on a Zeiss Observer.Z1 inverted microscope with TIRF slider, Definite Focus, Andor iXon X3 EM-CCD camera, and custom controller software. Images were acquired in TIRF mode using a 642 nm excitation laser at 2.8 mW power with a 100x oil objective (1.46 NA, Zeiss Plan-Apochromat) using a 100 ms exposure and 20 gain setting. Images acquired in standard epifluorescence mode were with the same laser and power settings, but with a 40x oil objective (1.3 NA, Zeiss Plan-Apochromat) with a 100 ms exposure and 20 gain setting.

HeLa cell mRNA capture and cDNA synthesis on functionalized surfaces

For these sets of experiments, 50 x 50 mm glass coverslips were fully functionalized with polyT following previously mentioned methods, but were not protectively patterned. Microfluidic channels were formed using double-sided tape (Scapa 702) and a pre-drilled glass slide. Channels were designed in AutoCAD (AutoDesk) and cut into the tape using a CAMM-1 Servo cutter plotter (Roland). Channels were loaded with a protein-free blocking buffer (Pierce) for 1 hour at room temperature and then washed with a lysis/binding buffer (500 mM LiCl, 1% LiDS, 10 mM EDTA, 5 mM DTT, 100 mM Tris-HCl pH 7.5; from Dynal mRNA Direct kit, Invitrogen).

HeLa cells were taken from culture by using trypsin/EDTA to remove the cells from the flask surface. Cell were counted and then mixed into the lysis/binding buffer at a cell concentration of 1 cell per nL. This concentration was chosen to mimic the

approximate concentration of the cells in the PDMS single-cell analysis devices. Cell lysates were loaded into the channels by pipette and allowed to incubate at room temperature for 20 minutes. Channels were then flushed with Washing Buffer A (10 mM Tris-HCl, pH 7.5, 150 mM LiCl, 0.1% LiDS, 1 mM EDTA) and Washing Buffer B (10 mM Tris-HCl, pH 7.5, 150 mM LiCl, 1 mM EDTA) from the Dynal mRNA Direct kit (Invitrogen). cDNA was then generated by injecting into each channel a cDNA synthesis mix from a SuperScript III First-strand synthesis kit (Invitrogen). All reaction conditions were according to the manufacturer's specifications except that no primer was included and for some reactions a 5-25% proportion of fluorescein-12-dCTP (Perkin-Elmer) to native dCTP was used. Negative control reactions contained no SuperScript III reverse transcriptase. Channel inlet and outlet ports were sealed with tape and the chip placed onto a custom made thermal block controlled by PC. Reverse transcription was run at 46 ºC for 3 hours and terminated by heating at 85 ºC for 5 minutes. The captured mRNA was then removed by loading RNaseH solution into each channel and incubating at 37 ºC for 20 minutes. Finally, the channels were flushed out with PBS buffer. For reactions using 100% native dNTP, the cDNA was counter-stained for 15 minutes with 1X SYBR Gold (Invitrogen) in PBS.

Single cDNA molecules were then imaged using TIRF microscopy on a Zeiss Observer.Z1 inverted microscope, TIRF slider, Definite Focus, Andor iXon X3 EM-CCD camera, and custom controller software. Images were acquired using a 488 nm excitation laser at 10.0 mW power with a 100x oil objective (1.46 NA, Zeiss Plan-Apochromat) with a 100 ms exposure and 60 gain setting.

mRNA capture kinetics experiments in PDMS microfluidic channels

Simple 15 mm long by 250 μm wide, straight PDMS microchannels were functionalized with polyT as mentioned previously. For this set of experiments, the fluidic channels were protectively patterned with a rectangular mask 10 mm long by 150 μm wide which masked the entire fluidic channel surface. This was meant to maximize the polyT functionalized surface area. Following polyT functionalization, channels were flushed clean with 2X SSCT. Using a syringe pump (Cavro XR Rocket Pump, Tecan Group) 10 μL of a 58 pM solution of mRNA-150A in 2X SSCT was pulled into the fluidic channel. Immediately after the solution was loaded, a custom acquisition program was implemented which acquired images at preset time intervals at the same field of view. All imaging was done using TIRF microscopy on a Zeiss Observer.Z1 inverted microscope, TIRF slider, Definite Focus, Andor iXon X3 EM-CCD camera, and custom controller software. Images were acquired using a 488 nm excitation laser at 5.0 mW power with a 100x oil objective (1.46 NA, Zeiss Plan-Apochromat) with a 200 ms exposure and 100 gain setting. The same experiment was repeated in a channel that was not functionalized with polyT.

HeLa cell mRNA capture kinetics experiments in PDMS microchannels

Simple 15 mm long by 250 μm wide, straight PDMS microchannels were functionalized with polyT as mentioned above. For this set of experiments, the fluidic channels were protectively patterned with a rectangular mask 10 mm long by 150 μm wide which masked the entire fluidic channel surface. This was meant to maximize the

polyT functionalized surface area. Following polyT functionalization, channels were flushed clean with 2X SSCT.

HeLa cells were taken from culture by using trypsin/EDTA to remove the cells from the flask surface. Cells were counted and then mixed into a lysis buffer (500 mM LiCl, 1% LiDS, 10 mM EDTA, 5 mM DTT, 100 mM Tris-HCl pH 7.5) with 2.5 nM concentration of NH_2-25mer polyT-Cy3 probes (Integrated DNA Technologies) at a final cell concentration of 1 cell per 3 nL. This concentration was chosen to mimic the single-cell microfluidic devices whose secondary compartments have a volume of ~3 nL. Cells were lysed by thoroughly mixing the solution by pipette.

Using a syringe pump (Cavro XR Rocket Pump, Tecan Group) 10 µL of the HeLa lysate solution was pulled into the fluidic channel. Immediately after the solution was loaded, a custom acquisition program was implemented which acquired images at preset time intervals at the same field of view. All imaging was done using TIRF microscopy on a Zeiss Observer.Z1 inverted microscope, TIRF slider, Definite Focus, Andor iXon X3 EM-CCD camera, and custom controller software. Images were acquired using a 532 nm excitation laser at 5.0 mW power with a 100x oil objective (1.46 NA, Zeiss Plan-Apochromat) with a 200 ms exposure and 100 gain setting. The same experiment was repeated in a channel that was not functionalized with polyT. As an additional control, another experiment was conducted in a polyT functionalized microchannel with the lysis and probe buffer only. These controls were implemented to test the non-specific binding of the mRNA and the Cy3 oligo probe to the surface.

Kinetics experiments image and data analysis

Analysis of acquired TIRF microscopy single-molecule images was conducted using a custom macro in ImageJ[31]. The macro takes an image and subtracts the background using a rolling ball radius of 3. Next, the image was inverted and a threshold applied. For control experiment images, the threshold applied was a Max Entropy threshold. For the other experiments an Otsu, IsoData, or custom threshold (min: 0, max: 0.95*max) was applied. The specific threshold was determined by selecting the threshold that best identified single-molecules. Following the threshold application, a particle count was performed. Because we did not know the exact number of fluorophores associated with each molecule, all size molecules were included in the count. For some sets of images where photo-bleaching of the fluorophores was evident, images were summed together in the series such that each molecule in each image would be consistently counted. Data obtained from the images was then compiled in MATLAB (Mathworks) and plotted using the Curve Fitting Toolbox. A nonlinear least squares fitting method based on the Trust-Region algorithm was applied to generate the optimal fit to the equation f(x) = a*(1-exp(-b*x)), which is the expected equation for pseudo-first order reaction kinetics.

4.4 Results and Discussion

Surface functionalization and protective patterning

Similar to the protective patterning and surface functionalization scheme discussed in Chapter 3, a method was employed here to allow for surface based capture

of mRNA transcripts from single cells within the compartments of the PDMS microfluidic device. The methodology employed is illustrated in Figure 4-2.

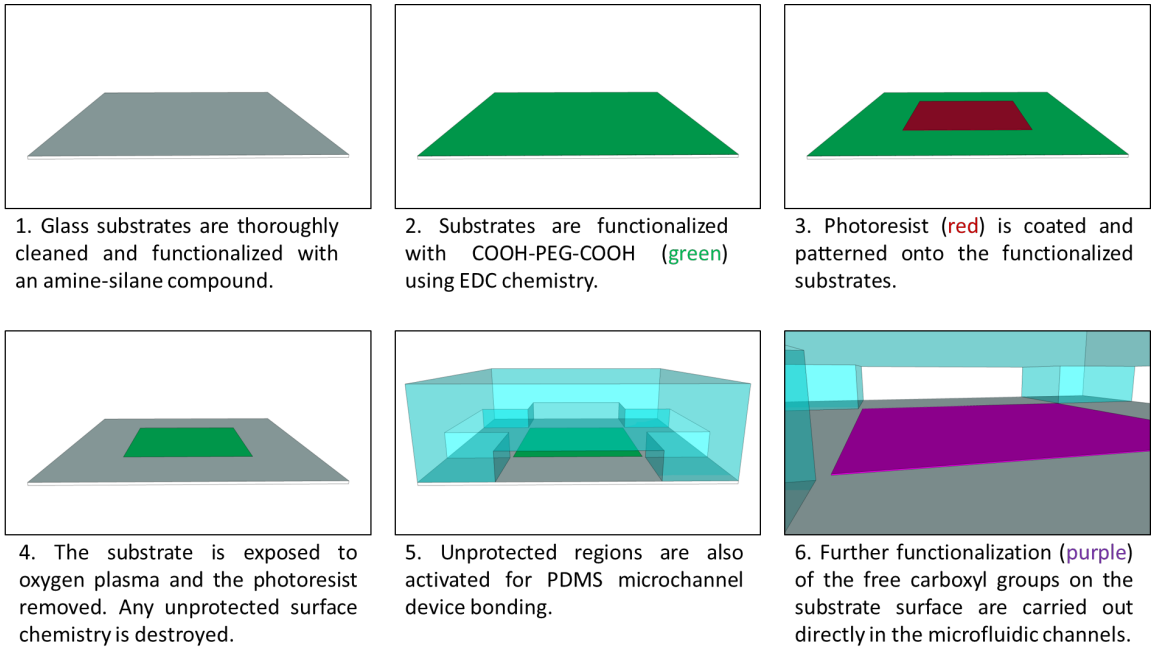

Figure 4-2. Protective patterning scheme for producing carboxyl surfaces in PDMS microchannels. Cleaned substrates are pre-functionalized and protectively patterned with photoresist and standard lithographic methods. The photoresist protects the surface chemistry during harmful exposure to oxygen plasma. This method also allows for standard PDMS device assembly. Subsequent modifications to free carboxyl groups are performed directly in the PDMS microfluidic channels.

The steps are very similar to the methods used in Chapter 3, but with a different type of surface molecules. Here we first functionalize the glass surface using standard silane chemistry with APTES. The free amine is then conjugated to a COOH-PEG1000-COOH molecule using standard EDC chemistry. The glass substrate, now coated with carboxyl functionality, undergoes the protective patterning procedure. Using a photomask and standard photolithography, a positive-tone photoresist is patterned onto the substrate to protect the underlying surface chemistry from the harmful oxygen plasma and UV exposure during the activation step in a UVO cleaner. This step destroys any exposed

surface chemistry as well as activates the glass surface such that the PDMS microchannel and valve layers can be permanently bonded to the glass. Again, it is crucial to remove the photoresist before PDMS bonding because the photoresist is much harder to fully remove from within the microfluidic channels. This is especially important with regards to mRNA analysis because single-molecule detection requires the surface be as clean as possible to ensure low incidence of false detection.

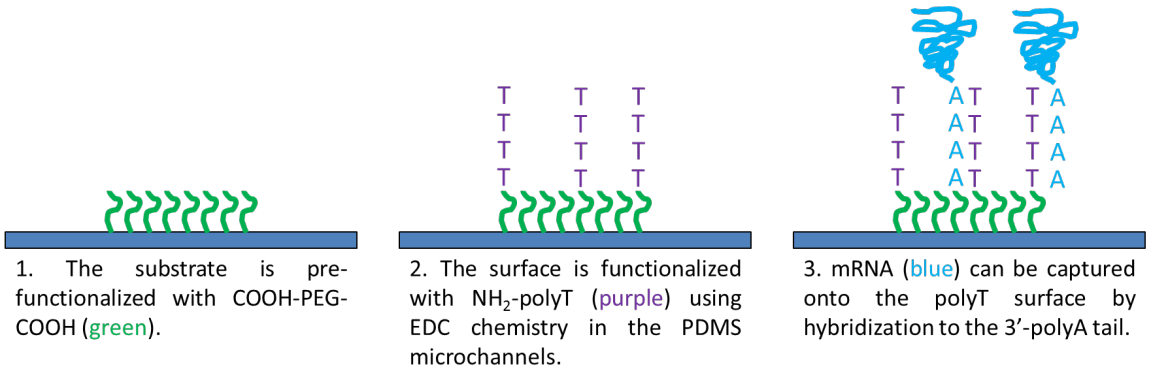

Figure 4-3. Functionalization scheme of substrate surfaces for capture of mRNA. Following PDMS device assembly, the free carboxyl groups are conjugated to NH_2-50mer-polyT using EDC chemistry. The polyT on the surface allows for capture of mRNA in solution by hybridization to the 3'-polyA tails on each transcript.

mRNA capture requires functionalization of the substrate surface with a molecule capable of capturing mRNA. In this case, we have chosen to functionalize the free carboxyl groups on the substrate surface with a NH_2-50mer-polyT oligo, as outlined in Figure 4-3. Many current mRNA purification kits and methods use polyT capture, so this method was chosen for use in this technology as well. Mammalian cell mRNA transcripts have 3'-polyA tails on average of around 200 bases, so the polyT must be shorter than the polyA tail to ensure proper priming of the mRNA for cDNA synthesis[32]. The 50mer-polyT fulfills this requirement and additionally, a 50 base-pair T:A sequence has a

melting temperature over 50 ºC meaning that the hybridization and capture of the mRNA to the polyT surface will be strong and rapid. As an added degree of versatility, the carboxyl functionalized surfaces may also be conjugated to a multitude of other DNA, proteins, or detection molecules.

Verification of surface functionality

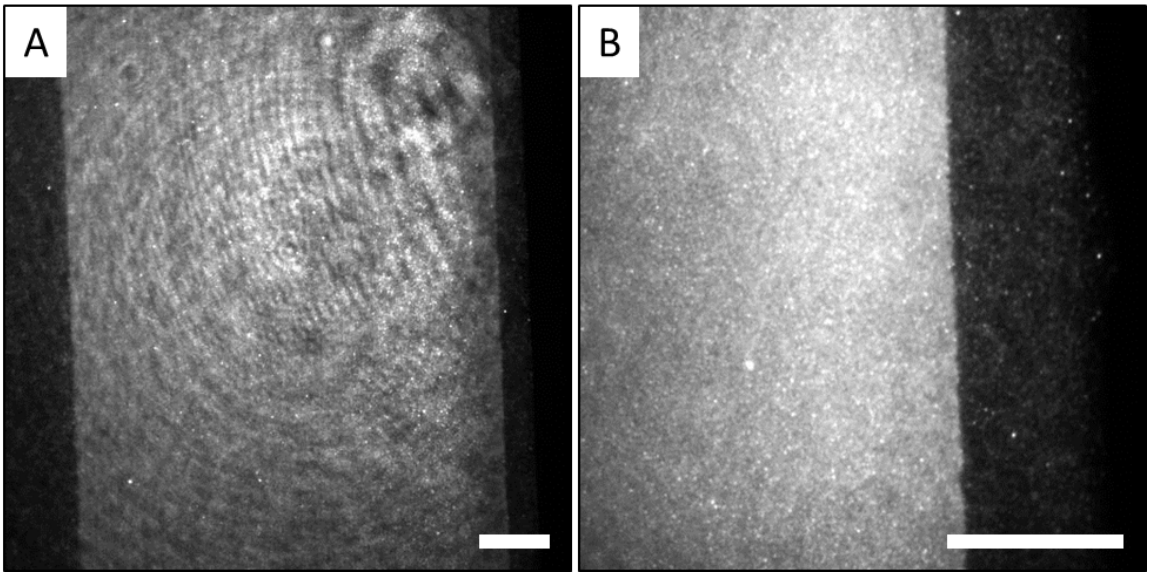

Figure 4-4. Verification of the polyT surface by Cy5-labeled 25mer-polyA oligo capture. (A) Fluorescent micrograph at 40x magnification of the captured oligo at a high-density in the PDMS microfluidic channel. (B) Fluorescent micrograph at 100x magnification showing a distinct boundary where the substrate surface was and was not protectively patterned. All scale bars correspond to 25 μm.

To verify that the protective patterning of the COOH-PEG-COOH followed by the polyT conjugation in the PDMS microfluidic channels was successful, a 0.5 μM solution of a Cy5-labeled 25mer-polyA oligo was injected into the fluidic channels and allowed to hybridize to the polyT on the substrate surface. This high concentration of oligo, along with the high-density polyT surface, produced a clearly fluorescent substrate

surface where the surface modification remained functional. The results of these experiments are seen in Figure 4-4A and B. In Figure 4-4A, a distinct strip of fluorescence is seen which corresponds to the protectively patterned region along the length of the 15 mm PDMS channel. Furthermore, in Figure 4-4B, acquired using a 100x oil objective in TIRF mode, the boundary between the protectively patterned and non-patterned region is very clear. Where the substrate was protected, there is an extremely high density of fluorescent oligo bound to the surface. In the region between the protectively patterned area and the PDMS wall, there is still some non-specific binding seen, but to a significantly lower degree. This region serves as a built-in negative control and indicates that if the surface is not protectively patterned, then the pre-modified surface cannot capture the oligo effectively. The protectively patterned region is seen to be fairly uniform along the entirety of the channel. This indicates that the strategy of pre-functionalization of COOH-PEG-COOH, protective patterning, PDMS device assembly, and polyT conjugation in the channels provides for a uniform and functional surface.

Other experiments were attempted, although not detailed here, where the polyT DNA oligo was conjugated to the glass substrates before protective patterning. While this method precludes the necessity to perform functionalization reactions within the intact PDMS microchannels, similar experiments hybridizing the Cy5-labeled 25mer-polyA oligo probe were unsuccessful. Instead of observing a densely fluorescent rectangular area, the entire channel surface bound little oligo probe and there was no distinction between protected and unprotected areas. Although our lab's previous experiments in destructive patterning successfully patterned DNA, those substrates were exposed only to oxygen plasma in a plasma descum machine[33]. In my methods, the surfaces were exposed

to UV, oxygen plasma, and ozone in the UVO cleaner. It is well known that UV can damage DNA, especially forming pyrimidine dimers, and thus the pre-functionalized polyT on the substrate surface may be rendered ineffective at capturing the polyA oligo probes[34]. Additionally, it has been shown that ozone can cause single-stranded DNA breaks and damage as well[35]. Consequently, it was determined that the photoresist patterns, although sufficient to protect the modified surface from oxygen plasma could not protect the surface from prolonged UV and ozone exposure. Thus, the substrate surfaces must have the NH_2-polyT conjugation performed after the protective patterning and PDMS bonding steps. These results, along with those in Chapter 3, also indicate that any PEG functionalized surface can withstand the entire protective patterning and PDMS bonding process without loss of functionality.

Surface density and mRNA capture kinetics calculations

With regards to mRNA capture, there are two key concerns that must be addressed for single-molecule mRNA analysis to be successful. The first is the quality of the substrate surface for conducting single-molecule imaging using TIRF microscopy. After the many steps involving surface functionalization and protective patterning with photoresist, it is imperative that the substrate surface remain clean such that single mRNA molecules, and subsequent single-molecule sequencing labeled-nucleotides, can be distinguished confidently. The second concern is the ability to quantitatively capture the mRNA transcripts from a single cell. As mentioned in the introduction, a single cell has only around 5×10^5 total mRNA transcripts with a wide range of copy number for each transcript type. In order to effectively analyze each transcript and generate an

expression profile, it is imperative that most, if not all, the mRNA be captured onto the surface. To investigate the ability to overcome these issues, mRNA capture kinetics experiments were performed in the PDMS microfluidic channels, but first, some calculations were performed to aid in experimental design.

Firstly, with regards to the ability to capture all mRNA from a single cell, it is important that the surface be modified with enough polyT to capture the transcripts. The limiting factors in the number of polyT available on the substrate surface are the number of COOH-PEG-COOH available for conjugation to the polyT as well as the surface area (packing density). A simple calculation of the radius of hydration (R_h) of the carboxyl-PEG molecule using Flory's mean radius calculation gives[36]**:**

$R_h = a*n^{\gamma}$ a = monomer length (PEG monomer: 0.35 nm)

n = number of monomers (22 units in PEG1000)

$\gamma = 0.6$ for a good solvent

$R_h = 2.24$ nm

Given a secondary compartment with surface area of 1.2×10^5 μm^2, a fully packed surface can hold 7.6×10^9 COOH-PEG-COOH molecules.

Now considering the polyT oligo, a similar surface density calculation can be performed as follows[26, 37]:

$R_h = 0.5*(L*p/3)0.5$ L = linear length of ssDNA = L = n*a

a = monomer length (0.43 nm)

n = number of monomers (50)

L = 215 nm

p = persistence length of ssDNA = 1.26 nm (in 100 mM MES)

$R_h = 4.75$ nm

Within the same compartment, the surface can hold 1.7×10^9 polyT molecules. Because the polyT has a larger radius of hydration, there can be fewer molecules of polyT on the surface than the number of carboxyl-PEG molecules; thus it is in fact the polyT that limits the total number of mRNA capture sites on the surface. Regardless, with only around 5×10^5 total mRNA transcripts per cell, there is significant excess of polyT on the surface. This density of polyT is assumed to be achieved since the polyT conjugation reaction uses a 5 μM solution, which in the compartment volume of 3 nL corresponds to 9×10^9 polyT molecules. Of course using a higher concentration will ensure maximal coverage of the surface. Additionally, different salt concentrations can be used to alter the radius of hydration to generate denser or sparser surfaces if needed.

If the surface has 1.7×10^9 polyT molecules, then this corresponds to a "bulk" concentration in each 3 nL compartment of about 0.94 μM. The concentration of mRNA from the single cell in each compartment is only about 0.3 nM. Thus, the second-order reaction of the hybridization of mRNA to the polyT on the surface can be simplified to a pseudo-first order reaction where the polyT concentration is said to remain constant. It is then expected that the capture of mRNA on the surface over time will follow as:

$$A(t) = A_{\max}(1 - e^{-kt})$$

A(t) is the number of mRNA captured onto the surface with A_{max} being all the mRNA molecules from each single cell. All experimental data collected was fit to an exponential function of this type.

Before running kinetics experiments it had to be determined on what time scales the experiments should be run. After lysis, the mRNA transcripts are contained within

each 3 nL secondary compartment where capture only occurs on the substrates surface. Thus, complete capture is highly dependent on the diffusion of the mRNA molecules. A quick calculation of an mRNA molecule's diffusion coefficient, given that the average mRNA molecule is about 1400 base-pairs in length is as follows [38]:

$$D = \frac{K_b T}{6\pi\eta R_h}$$

$K_b = 1.8 \times 10^{-23}$ m^2 * kg/s^2

$\eta = 0.001$ kg/(m*s) (viscosity of water)

$R_h = 5.35$ nm (p = 0.57 nm, L = 602 nm)

$D = 4.07 \times 10^{-11}$ m^2/s

Given the mean displacement as $\langle x^2 \rangle = 2Dt$, with a channel height of 25 μm, it would take on average only about 7.7 seconds for an mRNA molecule to diffuse the height of the channel. Of course the mRNA capture also depends on the probabilistic event that the 3'-polyA tail collides in the correct conformation with the polyT on the surface, and this is well documented in other works[39, 40]. Nonetheless, it is expected that mRNA capture will occur rapidly, on the order of tens of seconds to hundred seconds, given the small volume and low channel height. Kinetics experiments were chosen to be run for about 400 seconds total duration.

These calculations lead to the conclusion that the surface is functionalized with a high-density of polyT and that this high-density reduces the second-order mRNA capture kinetics to a pseudo-first order reaction. Additionally, given the small volume and channel height, it is expected that the capture of mRNA transcripts occur rapidly on the order of tens to hundreds of seconds.

mRNA capture kinetics in PDMS microchannels

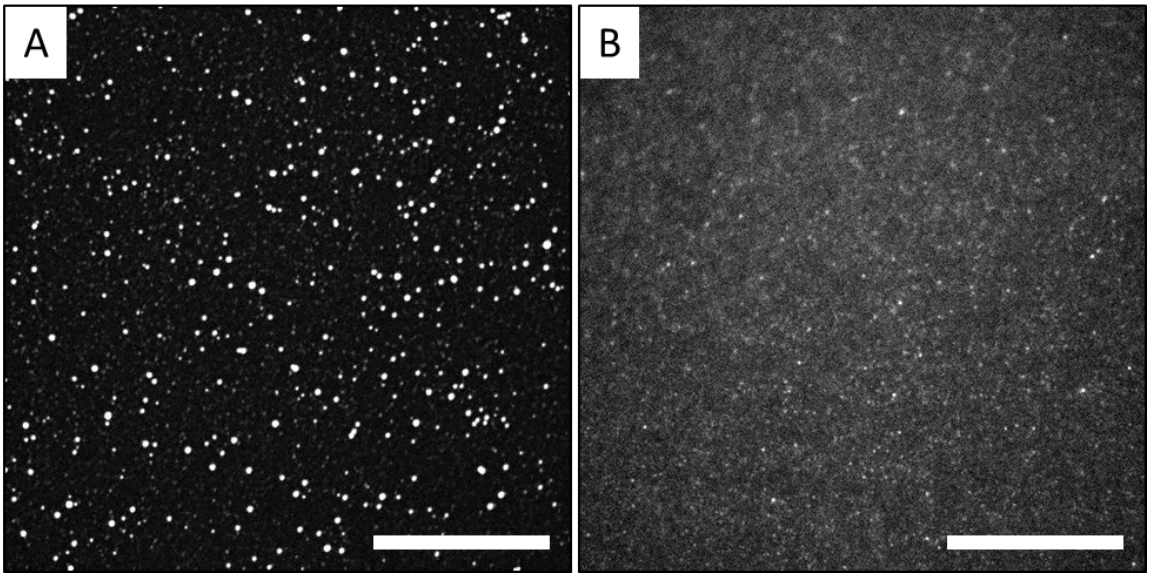

Figure 4-5. Single fluorescein-mRNA-150A molecule capture on functionalized surfaces in PDMS microchannels. (A) Fluorescent micrograph of single mRNA-150A molecules captured onto the functionalized substrate surface from a 58 pM bulk solution. (B) A control channel without polyT on the surface shows little mRNA-150A binding. Both images were acquired ~200 seconds after mRNA-150A solution injection into each microchannel. All scale bars correspond to 25 μm. Each image was adjusted for brightness and contrast.

Initial mRNA capture kinetics experiments were conducted using synthesized fluorescein-mRNA-150A. This allowed a specified concentration, 58 pM, to be used which mimicked the approximate concentration of single cell mRNA in a secondary compartment. Moreover, each mRNA molecule had incorporated fluorescein-UTP which allowed for easy single-molecule imaging without need for any secondary probe. Each imaged spot was assumed to be an mRNA molecule. Experiments were conducted both in a polyT functionalized microchannel as well as a channel with no polyT on the surface (carboxyl-PEG only). Results shown in Figure 4-5 from these experiments show images acquired 200 seconds after mRNA-150A injection into the microchannels. Comparison of Figure 4-5A and B clearly shows that there is minimal non-specific binding of the

mRNA-150A to the control surface. Conversely, in Figure 4-5A, many mRNA-150A molecules have been captured by hybridization to the polyT surface. The quality of the images acquired attests to the fact that the surface chemistry and protective patterning is indeed compatible with single-molecule imaging. The control image, Figure 4-5B, shows a very clean surface with few non-specific molecules bound. Additionally, the chemistry on the surface is robust enough to withstand all the processing steps yet still functional and able to capture mRNA by hybridization.

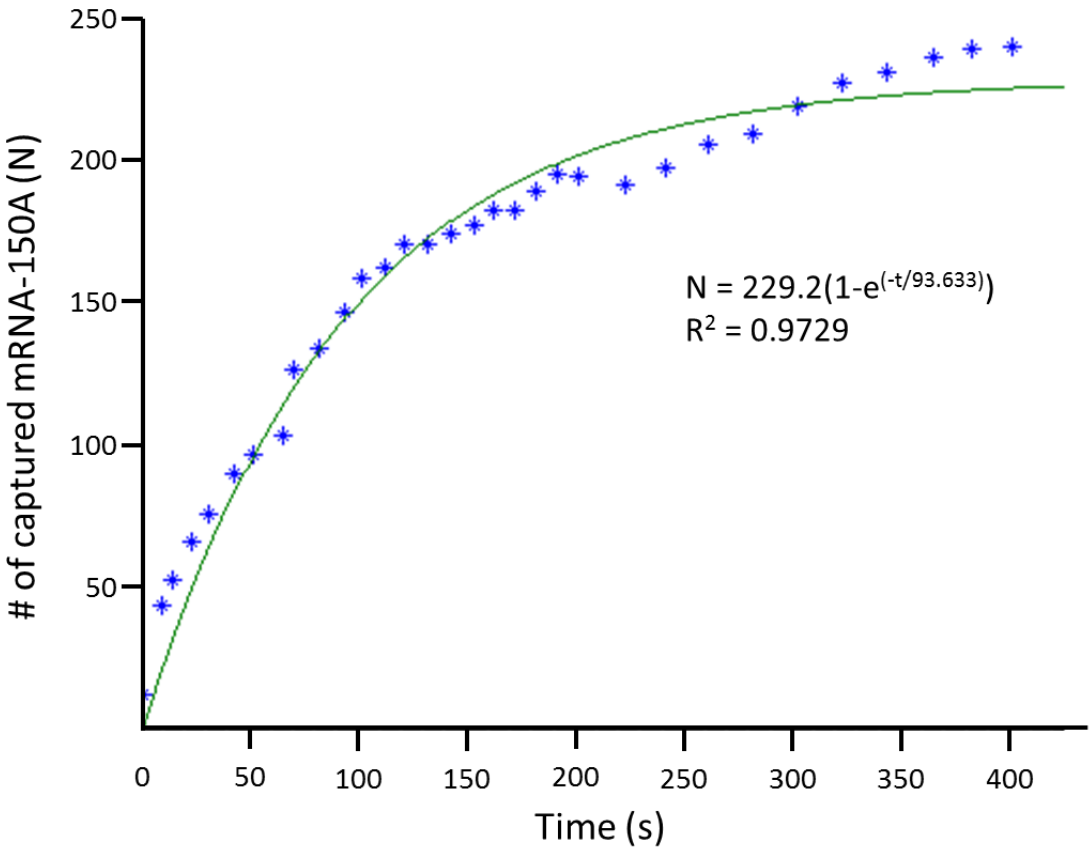

Figure 4-6. Capture kinetics of synthetic mRNA-150A in PDMS microchannels. Single mRNA-150A molecules were counted over time as they were captured onto the polyT functionalized surface from a 58 pM bulk solution. The data was fit with a single-exponential function with an $R^2 = 0.97$ and results indicate a time-constant of 93.6 seconds.

Single-molecule TIRF microscopy data for the kinetics experiments was collected and analyzed using a custom macro which counted the total number of mRNA-150A molecules captured in each image. A plot of the results is illustrated in Figure 4-6. Data was fit to an exponential functional with an R^2-value of 0.97, indicating a very good fit to the expected pseudo-first order reaction model. With a time-constant of 93.6 seconds, it is evident that the mRNA capture is relatively quick and full capture occurs on the order of hundreds of seconds. In fact, quantitative capture of mRNA seems to be possible in just a few minutes.

It is evident; however, in Figure 4-6 that the total count of surface bound mRNA molecules is not very high. In one field of view using the 100x objective, there should be about 5600 molecules in the volume directly above the field of view (given a 58 pM starting concentration). The low count seen in the plot could indicate that some mRNA molecules have non-specifically bound to the PDMS walls themselves, thus reducing the number of mRNA available to be captured on the substrate surface. Additionally, the fluorescein photobleaches relatively quickly and it is possible that over time even though the molecule is bound on the surface, it is not counted because the fluophore has been bleached. The particle counting macro also could introduce an artificial under-count of the particles. The macro relies on a threshold to differentiate between the background and the mRNA molecules. However, because the fluorescein-UTP is incorporated at random, each mRNA product can have a wide range of fluorescence. Ultimately, some of the less fluorescently intense molecules may be thresholded out and not counted. Despite these factors and given that the capture of each mRNA is an independent process; the actual molecule count is not what is important. Instead, it is the kinetics that is significant and

which points to the fact that single mRNA molecules can be captured onto the surface in the matter of a few minutes directly in the pre-functionalized PDMS microchannels.

HeLa cell mRNA capture kinetics

Following the success of the mRNA-150A capture and kinetics experiments on the polyT functionalized substrates in PDMS microchannels, experiments were carried out with HeLa cell lysates. Capturing and monitoring the capture of mRNA from a real cell sample is not quite as simple. In order to label only the mRNA transcripts from the cell, a short Cy3-labeled 25-mer polyT oligo was used. This probe was designed to be shorter so that the 50-base polyT on the substrate surface could still hybridize to the 3'-polyA tail of each transcript. Estimating that the mRNA concentration would be around 0.3-0.5 nM, the short probe was included into the lysis/binding buffer at a concentration of 2.5 nM. This would be a 5:1 to 10:1 ratio of probe to mRNA. If the ratio is too high, then it is possible that enough probes could bind to the mRNA polyA tail and saturate it, meaning that it cannot hybridize to the polyT on the surface. However, if it is too low, then many mRNA may not bind to a probe or bind only a single probe resulting in very low fluorescent signal. The optimal ratio of probe to mRNA still requires empirical testing, but will not be simple because the actual concentration of mRNA from a single cell is not definitively known.

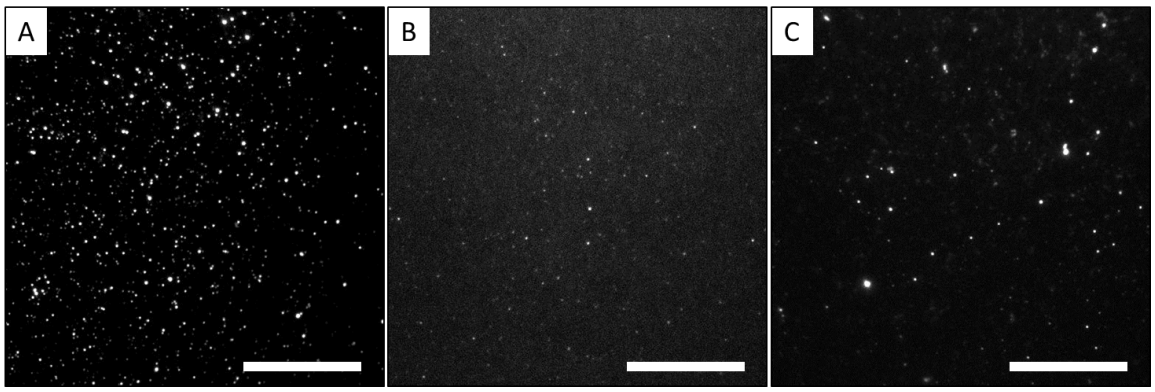

Figure 4-7. Single mRNA molecules from HeLa cells captured on functionalized surfaces in PDMS microchannels. (A) mRNA from HeLa cell lysates captured onto polyT functionalized substrates. (B) A negative control with no HeLa mRNA shows little non-specific binding of the Cy3-25mer-polyT probe onto the surface. (C) A negative control surface with no polyT shows few HeLa mRNA molecules binding on the surface. All images acquired with TIRF microscopy at ~200 seconds after sample injection into the microchannels. All scale bars correspond to 25 μm.

Results from the HeLa kinetics experiments in different microchannels are shown in Figure 4-7. In Figure 4-7A, it is seen that many mRNA transcripts have been captured onto a polyT functionalized surface. In Figure 4-7B, the image shows a control experiment in which no HeLa cell lysates were added to the lysis/binding mix. This experiment was used to test the non-specific binding level of the Cy3-labeled 25mer-polyT probe to the surface. From this image it is seen that there are only a few spots on the surface which indicate that the non-specific binding of the probe itself to the surface is low. Figure 4-7C shows an image from another control experiment in which HeLa lysates with the oligo probe are introduced into a channel that has not undergone polyT functionalization. The image shows a small number of mRNA non-specifically bound to the substrate surface, but not nearly as many spots as seen in Figure 4-7A. While the surface does have some level of non-specific binding, it is evident that this level is low

and that a properly functionalized polyT surface is necessary to capture mRNA directly from HeLa cell lysates.

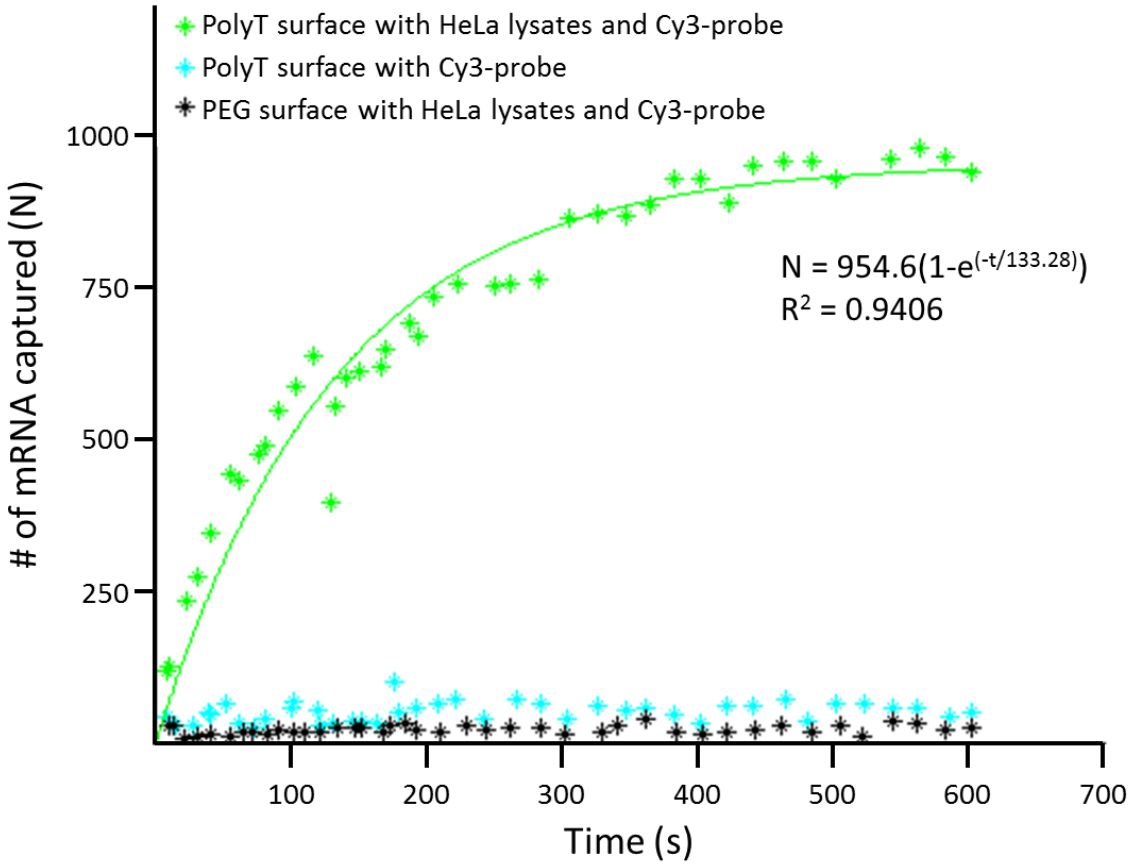

Figure 4-8. Capture kinetics of HeLa cell mRNA in PDMS microfluidic channels. mRNA from HeLa cells was captured onto a polyT functionalized surface in PDMS microfluidic channels at a cell concentration of 0.33 cells/nL. A Cy3-25mer-polyT probe at 2.5 nM was included in the lysis/binding buffer to label the single mRNA molecules. Control experiments (cyan, black) included one channel with no polyT and one channel with polyT but with the Cy3-25mer-polyT probe only and no HeLa mRNA. The kinetics plot shows little non-specific capture in control channels and good capture of HeLa mRNA with a time-constant of 133.28 seconds. Data was fit with a single-exponential function with an $R^2 = 0.94$.

Kinetics data was analyzed and is displayed in Figure 4-8. Analysis of this data shows similar results to those of the mRNA-150A capture kinetics. The data fits a single exponential function with an R^2-value of 0.94 indicating a good fit with a pseudo-first order reaction. Moreover, the time constant falls around a similar range at 133.28 seconds

indicating that transcripts can be captured quickly and quantitatively in the matter of minutes. Because the data compares well with the mRNA-150A kinetics data, it is assumed that the polyT probe did not interfere significantly with the ability to capture each transcript on the polyT surface. If there was interference, then the kinetics can be assumed to be faster than we observed.

Analysis of the HeLa mRNA data required application of a custom threshold which was determined manually. Because it is hard to predict the number of the polyT probes bound to the mRNA transcripts there was a very wide range of fluorescence intensity associated with the imaged spots. A standard Otsu or IsoData threshold significantly under-counted the molecules and thus a custom threshold was applied. Future work should focus on a more definitive and reliable image analysis method.

Although this set of experiments was conducted in linear PDMS channels and not in the single-cell capture devices themselves, the channel dimensions are identical and the HeLa lysates solution was diluted to the same concentration that would be present in each secondary analysis compartment. Therefore, these results are very convincing in proving that mRNA transcripts from single cells can be quantitatively captured onto pre-functionalized surfaces in PDMS microchannels.

cDNA synthesis from HeLa mRNA on functionalized surfaces

Following mRNA capture onto the substrate surfaces, the next key step involves the synthesis of cDNA from the captured transcripts. The polyT capture DNA on the substrate surface also serves as a primer for the production of cDNA by reverse-transcription. This step creates a covalently-linked library of single-cell cDNA on the

substrate surface that can be probed by hybridization or sequenced by single-molecule sequencing methods. Moreover, because the cDNA is covalently conjugated to the surface, it serves as a robust platform for which many reactions can be performed, one after another. Additionally, the cDNA is much more stable than the mRNA which allows for longer term storage and repeated use.

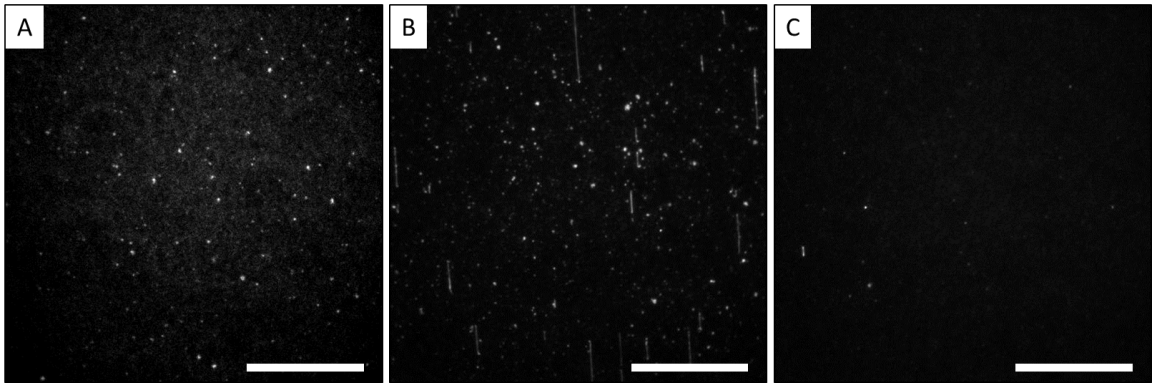

Figure 4-9. cDNA synthesis on polyT functionalized substrates. HeLa cell mRNA was captured onto polyT functionalized surfaces from a 1 cell/nL solution and reverse transcription performed to generate covalently-linked cDNA on the surface. (A) Single cDNA molecules incorporating fluorescein-dCTP at a ratio of 1:3 to native dCTP. (B) Single cDNA molecules with 100% native dNTP post-stained with SYBR gold on the polyT surface. (C) Negative control channel, which used a reaction solution without reverse-transcriptase, post-stained with SYBR gold showing no cDNA synthesis on the surface.

In cDNA synthesis experiments, HeLa cell mRNA was captured onto polyT functionalized glass substrates in microchannels assembled using double-sided tape and pre-drilled glass slides. Although not performed in PDMS devices, the substrate surface chemistry is identical and serves as a good initial test for mRNA capture and subsequent cDNA synthesis. Following mRNA capture, cDNA was synthesized using a standard SuperScript III reverse-transcription kit. In some channels, fluorescein-dCTP was incorporated to label the cDNA product such that it could be observed using TIRF microscopy. Other channels used 100% native dNTP and were post-stained with SYBR

Gold. Results of such experiments are shown in Figure 4-9. Figure 4-9A shows cDNA synthesized on the substrate surface which incorporated fluorescein-dCTP. Many distinct fluorescent spots can be seen on the surface indicating that cDNA synthesis was successful. Similarly, in Figure 4-9B, the fluorescent micrograph shows cDNA synthesized on the surface and stained with SYBR Gold. Again, many bright spots can be seen on the surface which corresponds to synthesized cDNA molecules. As a control, a reaction was run which did not contain any SuperScript III reverse-transcriptase, and this result in seen in Figure 4-9C. Following SYBR Gold staining, there are only a few spots seen on the surface. Because the SYBR Gold does not discriminate what type of DNA it stains, this result shows that not only is there no cDNA on the surface there is also little non-specifically bound genomic DNA or remaining mRNA on the surface. These results indicate that cDNA can be generated on the polyT functionalized glass surface directly from captured HeLa cell mRNA at a low cell concentration similar to that in the secondary compartments of the final PDMS device.

4.5 Summary and Future Directions

Single-cell gene expression profiling requires the ability to capture and identify all mRNA transcripts from a single cell. Here I have presented methods to overcome the extensive challenges associated with the quantitative capture of all mRNA from single cells in PDMS microfluidic devices. Methods for the chemical surface modification of glass substrates with COOH-PEG-COOH using standard silane chemistry, along with protective photolithographic patterning, provides for a mechanism in which defined

surface functionality is integrated with standard PDMS microfluidic device assembly. These methods overcome many of the existing challenges associated with surface functionalization and patterning within intact PDMS devices. These functionalized substrates were then conjugated to a polyT oligo and shown to be able to capture mRNA from both a low concentration, 58 pM, bulk solution as well as from HeLa cell lysates at a concentration analogous to that in the single-cell analysis devices. Quantitative capture results were shown by analysis of mRNA capture kinetics experiments and revealed that mRNA from single cells could be captured on the order of a few minutes with little to no non-specific binding. The mRNA capture kinetics was shown to match a pseudo-first order reaction. Additionally, initial results were described that indicated single covalently bound cDNA molecules could be synthesized from the captured mRNA transcripts on a polyT-functionalized substrate surface. Together, these results show that mRNA from a single cell can be quantitatively captured onto pre-functionalized and protectively patterned surfaces in PDMS devices.

Future work will aim to fully integrate these methods into the single-cell analysis device and show the process of mRNA capture to cDNA synthesis from whole cells. Single molecule sequencing-by-synthesis, which is already ongoing in the lab, will then require implementation and optimization. Although these involve extensive work, the final technology will enable entire transcriptome profiling from many single cells in parallel. This promises to reveal significant and detailed information about the true distribution of cellular states in a population, and have important implications in areas studying stem cell differentiation, drug response, and disease progression.

4.6 Acknowledgements

I would like to thank Matthew Walsh for his contributions and help with this work. His assistance in surface chemistry, data analysis, and single-molecule imaging and experimentation were instrumental. I would like to thank Dr. Eric Roller for his assistance in setup and implementation of TIRF microscopy equipment and software. I would also like to thank Dr. Zhixia Liu for synthesizing mRNA-150A for use in experiments. I would like to thank Ho Suk Lee and Ximin Chen for their assistance in cell culture. Portions of this work were conducted in the Nano3 clean room facility at UCSD. I would like to thank Dr. Bernd Fruhberger, Larry Grissom, Ryan Anderson, Sean Parks, and Dr. Xuekun Lu for their assistance in training with equipment.

4.7 References

1. L. Cai, N. Friedman and X. S. Xie, "Stochastic protein expression in individual cells at the single molecule level," *Nature*, vol. 440, no. 7082, pp. 358-362 (2006)

2. A. Citri, Z. P. Pang, T. C. Sudhof, M. Wernig and R. C. Malenka, "Comprehensive qPCR profiling of gene expression in single neuronal cells," *Nat Protoc*, vol. 7, no. 1, pp. 118-27 (2012)

3. A. Diercks, H. Kostner and A. Ozinsky, "Resolving cell population heterogeneity: real-time PCR for simultaneous multiplexed gene detection in multiple single-cell samples," *PLoS One*, vol. 4, no. 7, pp. e6326 (2009)

4. M. B. Elowitz, A. J. Levine, E. D. Siggia and P. S. Swain, "Stochastic gene expression in a single cell," *Science*, vol. 297, no. 5584, pp. 1183-6 (2002)

5. T. Kalisky and S. R. Quake, "Single-cell genomics," *Nat Methods*, vol. 8, no. 4, pp. 311-4 (2011)

6. Y. Kuang, I. Biran and D. R. Walt, "Simultaneously monitoring gene expression kinetics and genetic noise in single cells by optical well arrays," *Analytical Chemistry*, vol. 76, no. 21, pp. 6282-6 (2004)

7. J. M. Levsky and R. H. Singer, "Gene expression and the myth of the average cell," *Trends Cell Biol*, vol. 13, no. 1, pp. 4-6 (2003)

8. J. R. S. Newman, S. Ghaemmaghami, J. Ihmels, D. K. Breslow, M. Noble, J. L. DeRisi and J. S. Weissman, "Single-cell proteomic analysis of S. cerevisiae reveals the architecture of biological noise," *Nature*, vol. 441, no. 7095, pp. 840-846 (2006)

9. A. Raj, C. S. Peskin, D. Tranchina, D. Y. Vargas and S. Tyagi, "Stochastic mRNA synthesis in mammalian cells," *PLoS Biol*, vol. 4, no. 10, pp. e309 (2006)

10. N. Rosenfeld, J. W. Young, U. Alon, P. S. Swain and M. B. Elowitz, "Gene regulation at the single-cell level," *Science*, vol. 307, no. 5717, pp. 1962-5 (2005)

11. A. Stahlberg, D. Andersson, J. Aurelius, M. Faiz, M. Pekna, M. Kubista and M. Pekny, "Defining cell populations with single-cell gene expression profiling: correlations and identification of astrocyte subpopulations," *Nucleic Acids Res*, vol. 39, no. 4, pp. e24 (2011)

12. M. Bengtsson, A. Stahlberg, P. Rorsman and M. Kubista, "Gene expression profiling in single cells from the pancreatic islets of Langerhans reveals lognormal distribution of mRNA levels," *Genome Res*, vol. 15, no. 10, pp. 1388-92 (2005)

13. N. Navin and J. Hicks, "Future medical applications of single-cell sequencing in cancer," *Genome Med*, vol. 3, no. 5, pp. 31 (2011)

14. A. Stahlberg, M. Kubista and P. Aman, "Single-cell gene-expression profiling and its potential diagnostic applications," *Expert Rev Mol Diagn*, vol. 11, no. 7, pp. 735-40 (2011)

15. M. Batish, A. Raj and S. Tyagi, "Single molecule imaging of RNA in situ," *Methods Mol Biol*, vol. 714, no. pp. 3-13 (2011)

16. E. M. Gaynor, M. L. Mirsky and H. A. Lewin, "Use of flow cytometry and RT-PCR for detecting gene expression by single cells," *Biotechniques*, vol. 21, no. 2, pp. 286-91 (1996)

17. J. M. Levsky, S. M. Shenoy, R. C. Pezo and R. H. Singer, "Single-cell gene expression profiling," *Science*, vol. 297, no. 5582, pp. 836-40 (2002)

18. C. H. Hartmann and C. A. Klein, "Gene expression profiling of single cells on large-scale oligonucleotide arrays," *Nucleic Acids Res*, vol. 34, no. 21, pp. e143 (2006)

19. K. Kurimoto and M. Saitou, "Single-cell cDNA microarray profiling of complex biological processes of differentiation," *Current Opinion in Genetics & Development*, vol. 20, no. 5, pp. 470-477 (2010)

20. M. Saitou, Y. Yabuta and K. Kurimoto, "Single-cell cDNA high-density oligonucleotide microarray analysis: detection of individual cell types and properties in complex biological processes," *Reproductive Biomedicine Online*, vol. 16, no. 1, pp. 26-40 (2008)

21. K. Taniguchi, T. Kajiyama and H. Kambara, "Quantitative analysis of gene expression in a single cell by qPCR," *Nat Methods*, vol. 6, no. 7, pp. 503-6 (2009)

22. F. Tang, C. Barbacioru, Y. Wang, E. Nordman, C. Lee, N. Xu, X. Wang, J. Bodeau, B. B. Tuch, A. Siddiqui, K. Lao and M. A. Surani, "mRNA-Seq whole-transcriptome analysis of a single cell," *Nat Methods*, vol. 6, no. 5, pp. 377-82 (2009)

23. A. H. Diercks, A. Ozinsky, C. L. Hansen, J. M. Spotts, D. J. Rodriguez and A. Aderem, "A microfluidic device for multiplexed protein detection in nano-liter volumes," *Anal. Biochem.*, vol. 386, no. 1, pp. 30-35 (2009)

24. Y. Gong, A. O. Ogunniyi and J. C. Love, "Massively parallel detection of gene expression in single cells using subnanolitre wells," *Lab Chip*, vol. 10, no. 18, pp. 2334-7 (2010)

25. J. S. Marcus, W. F. Anderson and S. R. Quake, "Microfluidic single-cell mRNA isolation and analysis," *Analytical Chemistry*, vol. 78, no. 9, pp. 3084-9 (2006)

26. A. K. White, M. VanInsberghe, O. I. Petriv, M. Hamidi, D. Sikorski, M. A. Marra, J. Piret, S. Aparicio and C. L. Hansen, "High-throughput microfluidic single-cell RT-qPCR," *Proceedings of the National Academy of Sciences of the United States of America*, vol. 108, no. 34, pp. 13999-14004 (2011)

27. J. F. Zhong, Y. Chen, J. S. Marcus, A. Scherer, S. R. Quake, C. R. Taylor and L. P. Weiner, "A microfluidic processor for gene expression profiling of single human embryonic stem cells," *Lab Chip*, vol. 8, no. 1, pp. 68-74 (2008)

28. P. Liu and R. A. Mathies, "Integrated microfluidic systems for high-performance genetic analysis," *Trends Biotechnol*, vol. 27, no. 10, pp. 572-81 (2009)

29. L. T. Sam, D. Lipson, T. Raz, X. Cao, J. Thompson, P. M. Milos, D. Robinson, A. M. Chinnaiyan, C. Kumar-Sinha and C. A. Maher, "A comparison of single molecule and amplification based sequencing of cancer transcriptomes," *PLoS One*, vol. 6, no. 3, pp. e17305 (2011)

30. T. D. Harris, P. R. Buzby, H. Babcock, E. Beer, J. Bowers, I. Braslavsky, M. Causey, J. Colonell, J. Dimeo, J. W. Efcavitch, E. Giladi, J. Gill, J. Healy, M. Jarosz, D. Lapen, K. Moulton, S. R. Quake, K. Steinmann, E. Thayer, A. Tyurina, R. Ward, H. Weiss and Z. Xie, "Single-molecule DNA sequencing of a viral genome," *Science*, vol. 320, no. 5872, pp. 106-109 (2008)

31. M. D. Abramoff, P. J. Magelhaes and S. J. Ram, "Image processing with ImageJ," *Biophotonics Intl.*, vol. 11, no. 7, pp. 36-42 (2004)

32. G. Brawerman, "The Role of the Poly(a) Sequence in Mammalian Messenger-Rna," *Crc Critical Reviews in Biochemistry*, vol. 10, no. 1, pp. 1-38 (1981)

33. K. D. Barbee, M. Chandrangsu and X. Huang, "Fabrication of DNA polymer brush arrays by destructive micropatterning and rolling-circle amplification," *Macromol Biosci*, vol. 11, no. 5, pp. 607-17 (2011)

34. R. P. Sinha and D. P. Hader, "UV-induced DNA damage and repair: a review," *Photochem Photobiol Sci*, vol. 1, no. 4, pp. 225-36 (2002)

35. T. J. Cheng, H. P. Kao, C. C. Chan and W. P. Chang, "Effects of ozone on DNA single-strand breaks and 8-oxoguanine formation in A549 cells," *Environ Res*, vol. 93, no. 3, pp. 279-84 (2003)

36. J. E. Hearst, "Statistical mechanics of chain molecules. PAUL J. FLORY, Wiley (Interscience), New York, 1969, 432 pp. $17.50," *Journal of Polymer Science Part A-2: Polymer Physics*, vol. 8, no. 3, pp. 487-487 (1970)

37. B. Tinland, A. Pluen, J. Sturm and G. Weill, "Persistence Length of Single-Stranded DNA," *Macromolecules*, vol. 30, no. 19, pp. 5763-5765 (1997)

38. S. S. Sommer and J. E. Cohen, "The size distributions of proteins, mRNA, and nuclear RNA," *Journal of Molecular Evolution*, vol. 15, no. 1, pp. 37-57 (1980)

39. V. Chan, D. J. Graves and S. E. McKenzie, "The biophysics of DNA hybridization with immobilized oligonucleotide probes," *Biophysical Journal*, vol. 69, no. 6, pp. 2243-2255 (1995)

40. K. Pappaert, P. Van Hummelen, J. Vanderhoeven, G. V. Baron and G. Desmet, "Diffusion-reaction modelling of DNA hybridization kinetics on biochips," *Chemical Engineering Science*, vol. 58, no. 21, pp. 4921-4930 (2003)

5 ELECTRIC-FIELD DIRECTED ASSEMBLY OF ACTIVE ENZYME-NANOPARTICLE LAYERS

5.1 Abstract

A method is presented for the electric-field directed self-assembly of higher order structures composed of alternating layers of biotin nanoparticles and streptavidin/avidin-conjugated enzymes carried out on a microelectrode array device. Enzymes included in the study were glucose oxidase (GOx), horseradish peroxidase (HRP) and alkaline phosphatase (AP); all of which could be used to form a light emitting microscale glucose sensor. Directed assembly included fabricating multilayer structures with 200 nm or 40 nm GOx-avidin-biotin-nanoparticles, with AP-streptavidin-biotin nanoparticles, and with HRP-streptavidin-biotin-nanoparticles. Multilayered structures were also fabricated with alternate layering of HRP-streptavidin-biotin nanoparticles and GOx-avidin-biotin nanoparticles. Results showed that enzymatic activity was retained after the assembly process, indicating that substrates could still diffuse into the structures and that the electric field based fabrication process itself did not cause any significant loss of enzyme activity. These methods provide a solution to overcome the cumbersome passive layer-by-layer assembly methods to efficiently fabricate higher order active biological and chemical hybrid structures that can be useful for creating novel biosensors and drug delivery nanostructures, as well as for diagnostic applications.

5.2 Introduction

With recent advances in the assembly of nanoparticles (NPs) into higher order structures and components, the ability to incorporate biologically active molecules has become more important[1, 2]. Considerable research efforts are now directed towards the fabrication and integration of biologically active molecules into NP structures that could be used in drug delivery, biological and chemical sensors, and diagnostics. In most cases, these higher order structures are fabricated with passive layer-by-layer (LBL) techniques to self-assemble the molecules into organized structures through specific interactions including covalent binding, gold-thiol interactions, electrostatic interactions and protein-ligand binding[3-11]. However, passive processes are concentration dependent and these methods require complex processes and long incubation times in high concentration solutions of molecules. Moreover, in order to direct the assembly onto specific sites, blocking agents or physical patterning such as lithography is necessary[12]. To circumvent these issues, active processes have been developed, including DC electrophoretic deposition and magnetic field assisted deposition[13-18]. Also, work has been carried out on the use of AC dielectrophoretic techniques to manipulate NPs[19-21]. The application of electric fields allows for rapid, site-directed concentration of macromolecules, polymers, and NPs to enhance the self-assembly process. Such methods have been employed to produce colloidal aggregates as well as pattern NPs atop electrode surfaces[17, 22-29]. In addition, non-specific binding and high background, which play a crucial role in the incorporation and detection of biological molecules, can be reduced with electrode patterns which direct the molecules toward the active site where deposition is preferred

and away from non-active regions. More recently, the method of electrophoretic deposition has been applied to biological components. This powerful tool has enabled devices to be made which utilize the electric fields to enhance DNA hybridization, to form protein layers for biosensors and to pattern cells[30-36].

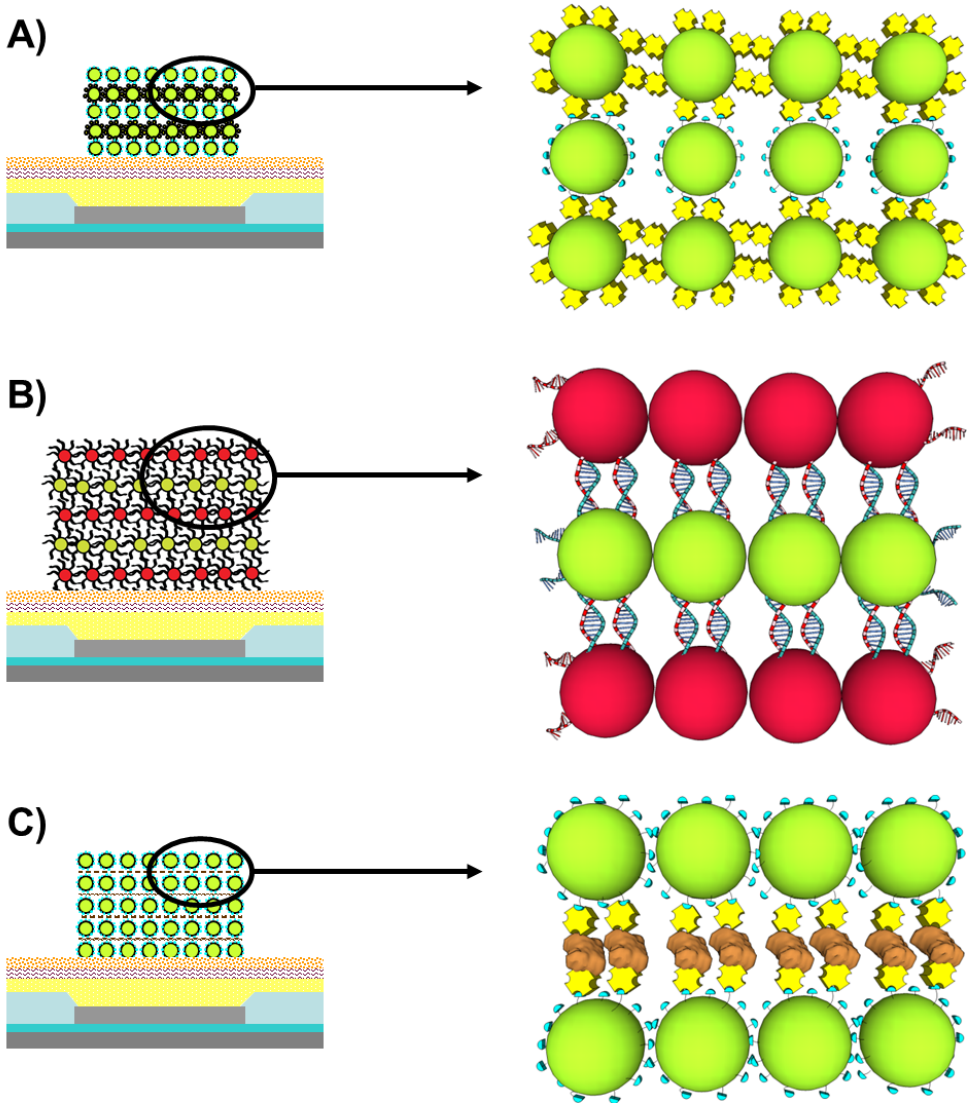

Figure 5-1. Electric field directed assembly (layering) of biomolecule-NPs by different binding mechanisms. (A) NP layering with alternate biotin (blue)-functionalized NPs and streptavidin (yellow)-functionalized NPs. (B) NP layering by hybridization of complementary DNA sequences. (C) NP layering of biotin-functionalized NPs with streptavidin-functionalized enzymes (brown). (Image not to scale)

Recently we have shown the ability to construct higher order NP structures by electric field directed self-assembly through the specific interactions of complementary DNA sequences as well as through protein-molecule interactions (Figure 5-1A and 5-1B)[14, 37, 38]. We now present the ability to integrate active enzymes into these NP structures by directed electrophoretic means (Figure 5-1C); thus providing a new bottom-up fabrication method for patterning and constructing structures from NPs in a rapid and combinatorial fashion atop a microarray.

5.3 Experimental Methods

CMOS Microarray Setup

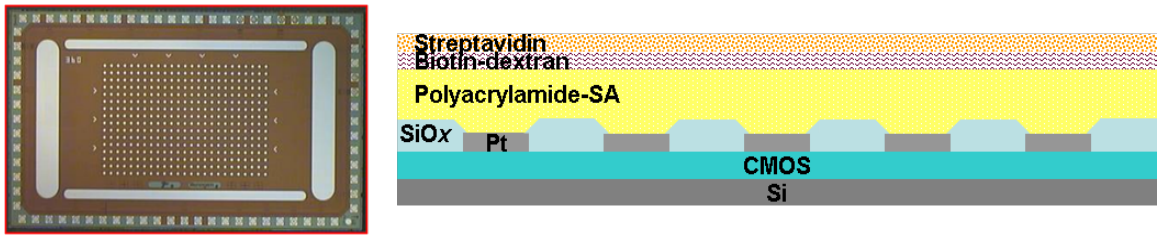

Figure 5-2. Images of the 400 site platinum electrode CMOS microelectronic array and a cross-section of the structure. The microarray is 4 mm x 7 mm and each microelectrode is 55 µm in diameter.

An ACV 400 CMOS electronic microarray (Nanogen, Inc.), shown in Figure 5-2, which consists of 400 individually controllable 55µm-diameter platinum electrodes was used for all layer assembly experiments. The microarray chip is over-coated by the manufacturer with a streptavidin-embedded polyacrylamide hydrogel which serves as a permeation layer. The device was computer-controlled using ACV400 software. The software allowed each electrode to be configured to independently source 0 to 5 V or 0 to

1 μA per electrode, with each electrode on the array capable of being independently biased.

Chip Preparation.

To prepare the chip surface as depicted in the cross-section in Figure 5-2, the microarray chip was first washed by pipetting 20 μL deionized water (dH_20, Millipore, 18MΩ) onto and off of the chip a total of 10 times. Subsequently, 20 μL of a 2 μM biotin-dextran (Sigma) solution in dH_2O was pipetted onto the chip and allowed to incubate for 30 minutes at room temperature. The chip was then washed again with dH_2O, followed by incubation with 20 μL of a 1 mg/mL solution of streptavidin (Sigma) in dH_2O for 30 minutes at room temperature. Finally, the chip was washed with 100 mM L-histidine buffer and kept moist prior to use.

Preparation of NPs and enzymes.

Yellow-green fluorescent biotin coated NPs, 200 nm and 40 nm diameter, (Molecular Probes, ex505, em515) were diluted to 0.01% (38 pM for 200 nm NPs and 4.7 nM for 40 nm NPs) in 100 mM L-histidine buffer. This suspension was vortexed and sonicated in a water bath for 15 minutes just prior to use to break up any aggregates. Additionally, glucose oxidase-avidin (GOx-avidin, Rockland) was diluted to 30 nM, streptavidin-alkaline phosphatase (streptavidin-AP, Sigma) was diluted to 40 nM and streptavidin-peroxidase (streptavidin-HRP, Sigma) was diluted to 95 nM in 100 mM L-histidine buffer just prior to use.

DC electric field directed assembly of streptavidin/avidin enzymes and biotin NPs

NP and enzyme addressing conditions are derived from previous work [14]. In brief, 20 μL of the 200 nm biotin NP solution or enzyme solution was pipetted onto the chip. The selected electrodes were biased positive and activated with a constant DC current of 0.25 μA for 15 seconds to concentrate and assemble the particles or enzymes atop the activated electrodes. The solution was then removed and the chip washed with 20 μL of L-histidine buffer a total of three times. Assembly of the layer structures was achieved by alternating the addressing of biotin NPs with streptavidin/avidin enzymes. Every structure was capped with a final layer of biotin NPs. Different layer structures include: layers of biotin NPs and GOx-avidin, layers of biotin NPs and streptavidin-AP, layers of biotin NPs and streptavidin-HRP, and layers of biotin NPs with alternate GOx-avidin and streptavidin-HRP to produce bi-enzyme structures. Identical conditions were employed to assemble layers of 40 nm biotin NPs with streptavidin-AP.

Monitoring of layer assembly by fluorescence and ImageJ calculations

Monitoring of layer growth was done by real-time imaging on an epifluorescent Leica microscope, with a Hamamatsu Orca-ER CCD using a custom LabVIEW interface. Images were acquired throughout the layering process and processed in ImageJ. For analysis, each image had its background subtracted with a rolling ball radius of 50. The image was then inverted and threshold fixed using the IsoData threshold. Manual adjustments were made to include as many electrodes as possible. A corresponding mask was generated to ensure each measured electrode area was identical. Raw integrated

density values for each electrode were then acquired by mapping the data in the original image to the generated mask image.

Verification of enzyme activity via x-ray film

The verification of enzyme activity was performed on chips composed of alternate layers of 200 nm biotin NPs with either GOx-avidin or streptavidin-AP as the enzyme layers. All 400 electrodes on the array were activated to maximize the total number of fabrication sites for the layer structures. For the structures assembled with GOx-avidin a reaction solution consisting of 227 mM glucose (Sigma), 8.4 mM luminol (Fluka), and 0.1 mg/mL peroxidase (Sigma) in 0.035 M Tris-HCl (pH 8.4) was prepared. The chips were washed with 100 mM L-histidine buffer and then with 0.1M Tris-HCl (pH 8.0). Subsequently, 15 μL of the reaction solution was pipetted onto the chip surface. For chips with layer structures assembled using streptavidin-AP, the chips were washed with 100 mM L-histidine buffer and then 15 μL of CDP-star chemiluminescent reagent (Sigma) was dispensed onto the chips.

The chips were then wrapped in plastic wrap to prevent solution loss and placed into a cassette with x-ray film (Denville Scientific) for overnight exposure. The film was developed in a Hope Micro-Max developer, scanned, and analyzed using ImageJ. The relative intensity from each chip was normalized to a chip that did not undergo layer assembly which was cleaned, prepared with the appropriate reaction solution, and exposed overnight as well.

Environmental Scanning Electron Microscopy (ESEM) of the enzyme-NP layer

After assembly of the enzyme-NP layers, the chip was washed multiple times with 100 mM L-histidine buffer and then all solution was removed from the surface to allow the chip to dry. Chips were then coated with either 40 nm of gold sputtered via a Denton Discovery 18 sputter system or 40 nm of chromium via Denton IV desktop sputter coater. Fractures were introduced into the structures by careful cutting with a razor blade. Images were then acquired on a Phillips XL30 ESEM using a 10 kV beam in high vacuum mode.

5.4 Results and Discussion

Assembly of enzyme-NP layers and verification of proper layer formation

The assembly of NP layers was monitored by epifluorescence imaging; however, because only the biotin NPs are fluorescent it was first important to verify that the NP-enzyme layers were forming as proposed with alternate layering of enzymes and NPs, as opposed to formation due to non-specific interactions of the biotin NPs to themselves. This was done by organizing the electrodes into three specific regions, as shown in Figure 5-3A. Region A consisted of microelectrodes which were never activated. This section served as a negative control to measure the amount of passive binding to the chip surface that would occur simply due to the presence of NPs and enzyme during alternate addressing steps. Region B consisted of microelectrodes only activated when the biotin NPs were addressed. This region served to measure the amount of non-specific binding of the NPs to themselves. Additionally, it served to show the amount of passive assembly

that could occur if no enzyme was actively addressed to these microelectrode sites. Finally, region C consisted of microelectrodes which were activated during all addressing steps of NPs and enzymes. Microelectrodes in this region were expected to have proper formation of enzyme-NP layers.

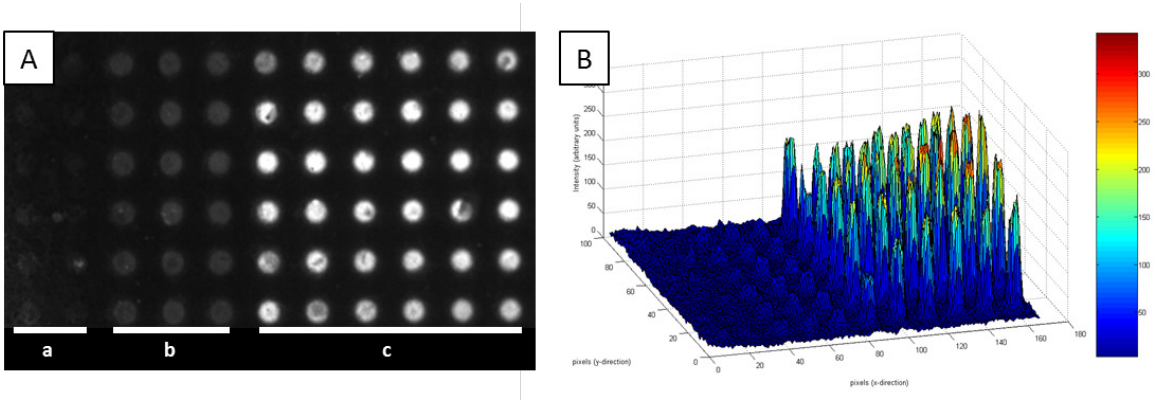

Figure 5-3. Verification of the assembly of enzyme-nanoparticle layers. (A) Fluorescence image of a section of the CMOS microarray after addressing 39 combined layers of biotin NPs and GOx-avidin. a) No current applied. b) Current applied ONLY when biotin NPs were addressed. c) Current applied when BOTH biotin NPs and GOx-avidin were addressed. (B) Corresponding MATLAB plot of the relative fluorescence intensity (z-axis) of each electrode.

The results in Figure 5-3A and 5-3B indicate that the microelectrodes in region A have a fluorescent signal near that of the background, which is the surface of the chip between the electrodes; thus indicating that a very low number of fluorescent biotin NPs passively bound to the streptavidin surface at these sites. Microelectrodes in region B, which were only activated when biotin NPs were addressed, have a low level fluorescent signal and the microelectrodes in region C, which were activated when both NPs and GOx-avidin were addressed, have a high level fluorescent intensity indicating that multiple layers of NPs formed in region C. Comparison of fluorescence intensities between the three regions suggests that in order to construct higher order structures both NPs and enzymes must be addressed to the same site, as in region C. If only biotin NPs

are addressed, as in region B, the NPs will not bind to one another and no higher order structures are formed, therefore there is only low fluorescence intensity from the first layer of biotin NPs assembled onto the streptavidin chip surface. These results were verified with all three enzyme types and with both 200 nm and 40 nm NPs.

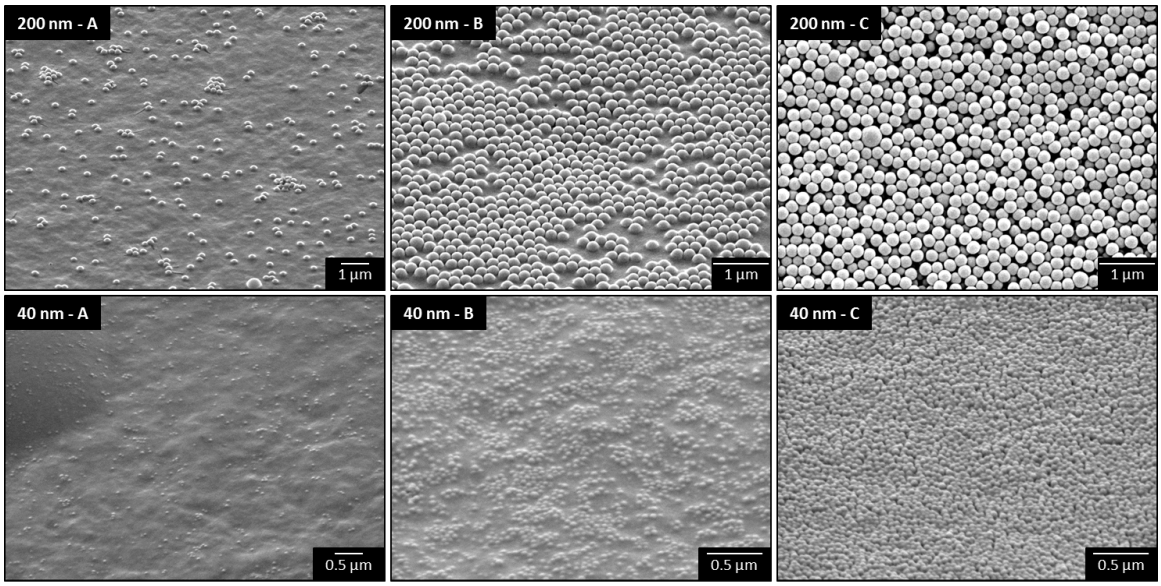

Figure 5-4. Verification of assembly by ESEM. ESEM images of a microelectrode in each region A, B, and C after enzyme-NP assembly. Top row: microelectrodes after assembling 31 total alternating layers of 200 nm biotin NPs and streptavidin-AP. Bottom row: microelectrodes after assembling 21 layers of 40 nm biotin NPs and streptavidin-AP.

In corroboration with the fluorescence data, Figure 5-4 shows environmental scanning electron microscopy (ESEM) images of three microelectrode sites; one each for region A, B, and C after addressing 31 total layers of 200 nm biotin NPs and streptavidin-AP as well as 21 layers of 40 nm biotin NPs and streptavidin-AP on separate microarray chips. The microelectrodes from region A show only a small number of passively attached biotin NPs. The electrodes from region B show nearly a complete monolayer of biotin NPs, despite being exposed to 16 total addressing steps of biotin NPs. This

demonstrates that there is little non-specific binding of the biotin particles to themselves; so despite the electric field directing additional NPs onto the first layer of NPs, they do not stick and are removed during the wash steps. The electrode from region C shows a high number of NPs assembled atop each other. Thus, active directed concentration of both the streptavidin/avidin enzyme and biotin NPs is necessary to assemble the higher order structures and the layer assembly process does indeed proceed as designed. Additionally, the lack of particles on region A's microelectrodes further verifies that electric field directed assembly is efficient and can overcome the diffusion limited process of passive LBL assembly. Each assembly step only required 15 seconds with NP and enzyme concentrations in the pM and nM range. At these time scales and NP and enzyme concentrations, no layers could be formed passively on the region A microelectrodes.

These results show that the electric field directed assembly technology is easily scalable to NPs of various sizes. This allows for tuning of the porosity of the final structures which may help control the (enzyme) substrate turnover and reaction kinetics, both of which would play crucial roles in biosensor devices. For drug delivery particles, the porosity will play a paramount role in the drug release profile. Moreover, we believe that integration of various types of NPs with different biomolecules would also be achievable as long as the proper binding elements are in place. Using multiple sized NPs would enable multiple porosities through the structure which may be needed to optimize reaction rates in multi-enzyme structures. Particles such as quantum dots could be incorporated to enhance detection. Moreover, using other biomolecules such as antibodies or DNA would allow the creation of a wide array of biosensors.

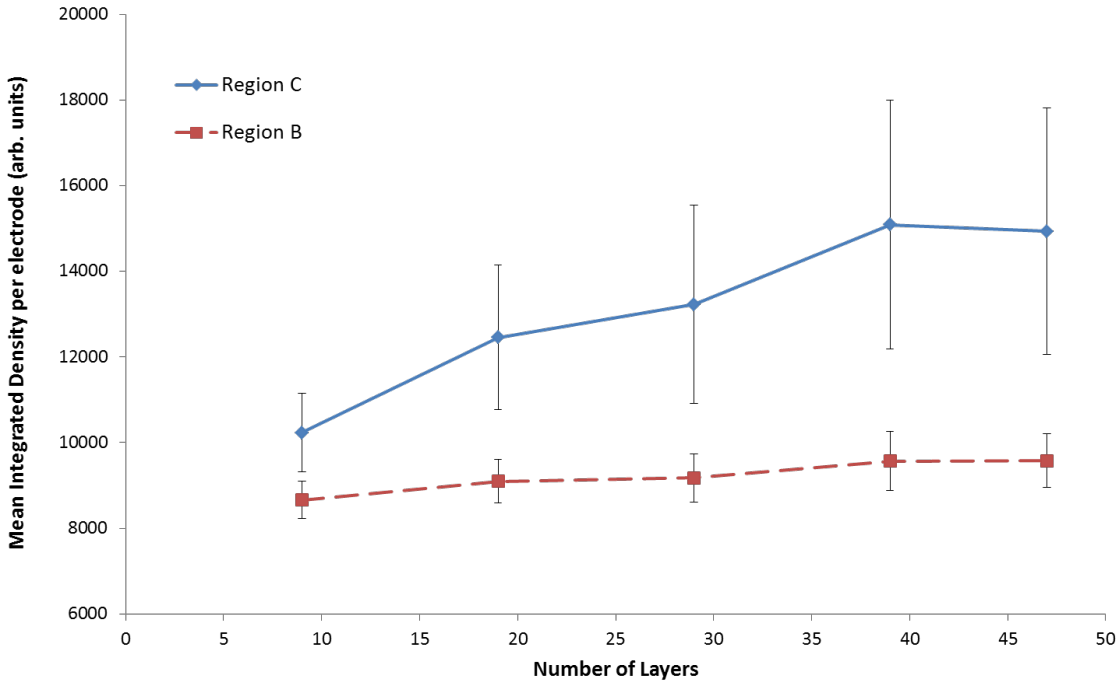

Figure 5-5. Monitoring layer assembly by fluorescence. Plot showing the calculated mean integrated density per microelectrode for microelectrodes in regions B and C in bi-enzyme layer structures of 9, 19, 29, 39, and 47 total layers of 200 nm biotin NPs with alternate enzyme layer addressing of GOx-avidin and streptavidin-HRP.

Monitoring NP layer assembly and quality of layers

Real-time layer assembly was monitored by visualizing increasing fluorescence intensity atop the microelectrode sites. Figure 5-5 shows a plot of the mean integrated density of fluorescence per microelectrode for microelectrodes in regions B and C of a microarray after 9, 19, 29, 39, and 47 total layers of 200 nm biotin NPs with alternate addressing of both GOx-avidin and streptavidin-HRP. From the plot, it is evident that the fluorescence for microelectrodes in region B, microelectrodes activated only when biotin-NPs were addressed, maintain roughly the same fluorescence intensity throughout the layering experiments. These results further substantiate the results in Figures 5-3 and 5-4 that without active electric field directed assembly of streptavidin/avidin-conjugated

enzymes onto the biotin NPs there is no further layer assembly. Additionally, these results verify that multiple types of enzymes can be incorporated into the same structure as long as they are properly functionalized. In this case, there is a streptavidin-functionalized HRP and an avidin-functionalized GOx, both of which can bind to the biotin on the NPs and facilitate layer formation. The plot shows a trend of increasing mean fluorescence for microelectrodes in region C as the total number of layers increases. This is what is expected because as the number of layers increases there are more total fluorescent NPs on each microelectrode. The plot in Figure 5-5, however, does have quite a large amount of variability, which could be attributed to many factors. One factor could be the stoichiometry of the streptavidin conjugation to the enzyme. Streptavidin-HRP was conjugated at a 1:1 ratio and streptavidin-AP at a 2:1 ratio according to the manufacturer's specifications. Streptavidin-AP thus has 4 more available biotin binding sites per enzyme molecule. This increased availability of binding sites makes attachment to biotin NPs more robust and can lead to an increased quality of uniformity of NP layers. Thus, to enhance binding, enzymes can be conjugated with a higher ratio of streptavidin/avidin per enzyme. In addition, as the number of layers increases the stresses on the layer structure increase and the structure could shear or break apart more easily during washes. It is sometimes seen that atop a specific microelectrode the fluorescence intensity would suddenly decrease and this effect was believed to be due to layer fracture and particle loss. Again, a higher stoichiometry of streptavidin to protein would increase the binding interactions between layers and help to prevent structure fracture and NP loss. Finally, another factor could be attributed to non-uniformity in the electric field across

the microarray chip or even across an individual microelectrode. This would also lead to variations in NP and enzyme assembly.

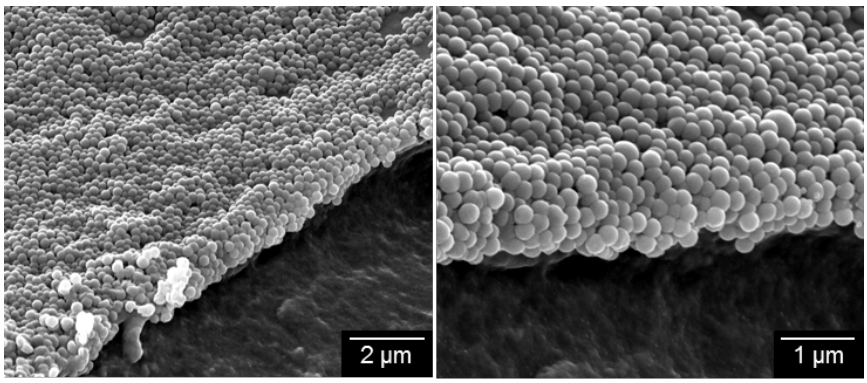

Figure 5-6. ESEM images of enzyme-NP layering. Micrographs show 200 nm biotin NPs layered with GOx-avidin at introduced cuts showing the layering of NPs.

ESEM images, as seen in Figure 5-6, obtained at the edge of introduced fractures reveal the layering of the NPs atop the hydrogel layer. From these micrographs it is evident that the assembled structures have variability in surface topography making it difficult to clearly distinguish one layer from the next. This is mostly attributed to the particle packing orientation as each additional layer of NPs packs onto the layer below. Additionally, this could be due to NP loss during the introduction of a fracture, during the sputtering of the metal over-layer for ESEM imaging, or even during the imaging process itself. In addition, there may be loss during washes and variations in binding across the electrode during the assembly process.

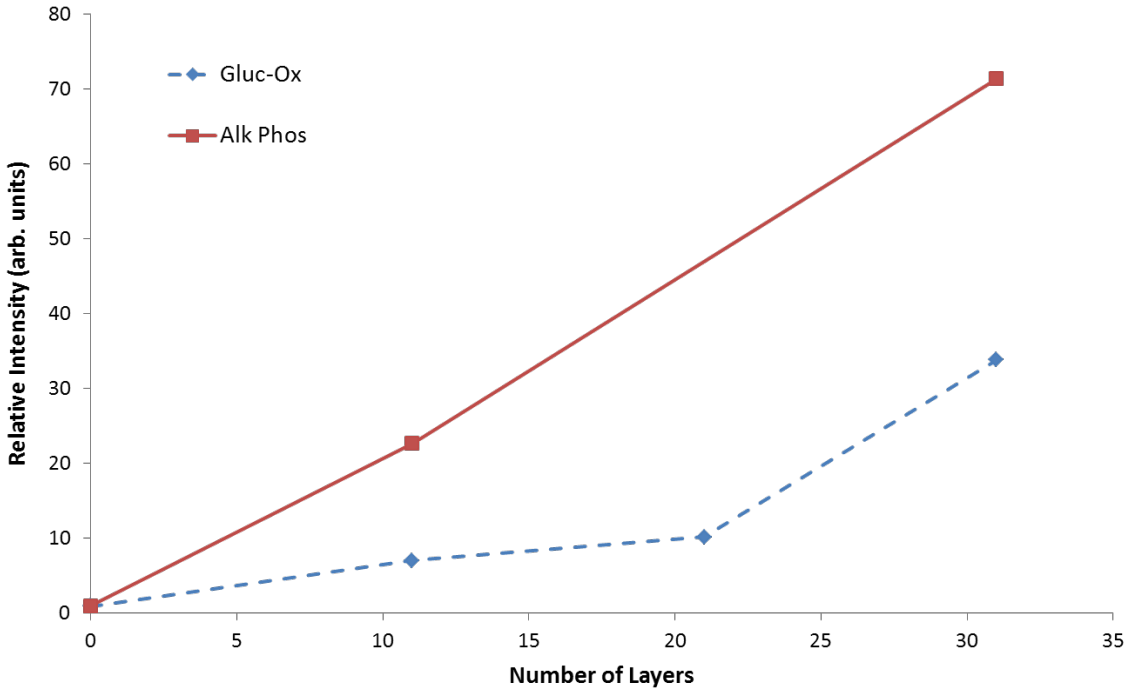

Figure 5-7. Retention of enzyme activity. Plot of the relative intensity of chemiluminescent signal obtained from chips addressed with 0, 11, 21, and 31 layers of 200 nm biotin NPs and GOx-avidin or 0, 11, and 31 layers with streptavidin-AP.

Retention of enzyme activity

Retention of enzyme activity after layer assembly was evaluated by incubating the microarray chips with the appropriate chemiluminescent substrate and then exposing the chips to x-ray film. The results of the scanned and analyzed x-ray film detection of the enzyme-NP layers are shown in Figure 5-7. Data was collected from chips layered with 200 nm biotin NPs and GOx-avidin with 0, 11, 21, and 31 total layers as well as chips layered with 200 nm biotin NPs and streptavidin-AP at 0, 11, and 31 layers. The results show increasing activity detected with an increasing numbers of layers. This trend is seen with both types of enzymes and this indicates that the total enzyme activity can be tuned simply by altering the number of enzyme layers incorporated into each structure. Similar

results could not be obtained from bi-enzyme structures, consisting of both GOx-avidin and streptavidin-HRP, as illustrated in Figure 5-8. This may be due to a number of reasons including poor reagent and substrate quality, poor layer quality, poor structure porosity, insufficient enzyme incorporation into the layers, and a poor detection scheme. A bi-enzyme structure requires optimization due to the coupling of multiple reaction steps. If any one of the reactions is inefficient, then the overall signal may not be detectable. In addition, the products from the first reaction must be able to effectively diffuse to the second set of enzymes; thus the enzyme layering order may be of importance. Additionally, an important aspect of producing active NP layers is the ability to sensitively detect their activity. The x-ray film used in the detection method verified in proof-of-principle that the biological activity of the molecules could be retained after assembly. More sensitive methods, including amperometric detection or highly sensitive imaging, beyond the capabilities of the microelectronic array and imaging system we had available, would allow for a better detection scheme to monitor total activity for each fabricated structure. Nonetheless, the presence of a measurable enzyme activity from the single enzyme structures verifies that the application of an electric field is not only efficient for structure assembly but also gentle enough to preserve the functionality of the enzymes.

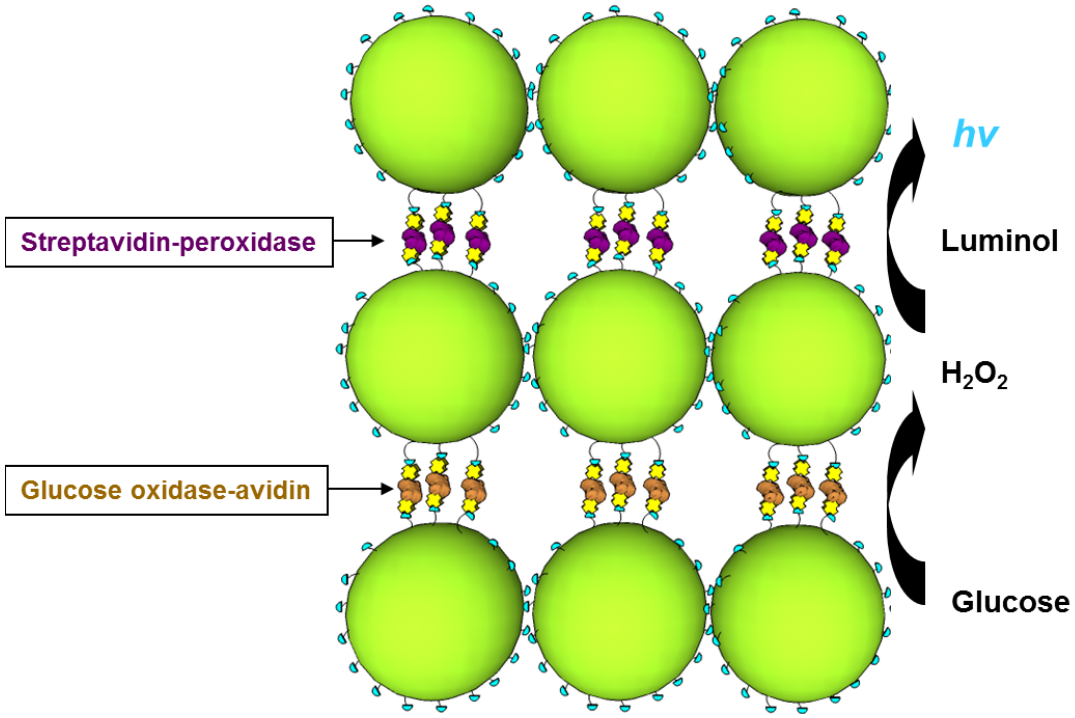

Figure 5-8. Proposed coupling of bi-enzyme NP layers. The incorporation of both streptavidin-HRP and GOx-avidin into the same layer structure may allow for chemical coupling of the layers. The oxidation of glucose by GOx produces hydrogen peroxide which is then a substrate for the chemiluminescent oxidation of luminol, which generates light that can be detected.

Altogether the results showing enzyme-nanoparticle layer assembly and enzyme activity retention demonstrate an efficient and effective method of fabricating biological or chemical sensors. Site-specific layer assembly, demonstrated in this study as well as previous studies, means that multiple types of enzyme-nanoparticle structures can be fabricated on each chip in a combinatorial manner [37]. Additionally, various types of enzymes, proteins, or other biomolecules could be used in conjunction with a wide array of particle types as long as they have complementary binding mechanisms, such as the biotin-streptavidin scheme used here. This would allow for production of high-density microarray sensors capable of analyzing hundreds of analytes at a time.

5.5 Summary and Future Directions

We have successfully demonstrated the ability to fabricate higher-order enzyme-NP structures by electric field directed self-assembly. Through the application of electric field directed assembly, alternating layers of 200 nm or 40 nm biotin NPs and streptavidin/avidin enzymes have been assembled up to 47 layers. These structures included multilayer structures with 200 nm or 40 nm GOx-avidin-biotin-NPs, with AP-streptavidin-biotin NPs, and with HRP-streptavidin-biotin-NPs. The electrophoretic assembly method atop a microelectronic array allows for site-specific fabrication from low concentration solutions of enzymes and NPs. The concentration effect due to the electrophoretic deposition results in rapid layer assembly with minimal passive non-specific binding on inactive sites across the chip. Moreover, the enzymatic activity of the biological molecules was preserved in the assembled structures. In addition, we have assembled structures consisting of multiple enzyme types, GOx-avidin and streptavidin-HRP, which demonstrates the potential of multilevel reactions or detection schemes, including chemiluminescence and bioluminescence. This method of fabrication now provides an efficient mechanism of creating biologically and chemically active NP structures from individual components much more efficiently than traditional passive layer-by-layer methods. Assembly of these structures in a combinatorial manner to specific sites on the chip, using a wide array of biomolecules (proteins and DNA) and nanoparticles would allow for fabrication of high-density microarray sensors for high-throughput analysis. The ability to incorporate multiple types of molecules along with the potential of lift-off, which enables the detachment of these structures from the surface,

renders them more versatile as dispersible biosensors, diagnostic tools and drug delivery vehicles.

Additionally, in relation to Chapter 3, these methods could be used to assemble high-density protein arrays in a combinatorial method within each single-cell capture compartment so long there are individually addressable electrodes. This would circumvent any tedious coding and de-coding strategies. Moreover, these methods in assembling active enzyme layers could produce layers used to interrogate live single-cells by measuring analytes such as cell-secreted molecules or even cellular metabolism.

5.6 Acknowledgements

The authors thank Nanogen, Inc. for supplying microelectronic arrays and the Nanochip 400 system, Dr. Dietrich Dehlinger for assistance and training with the system and methods, Juhi Saha for her help in experiments, and the UCSD Nano3 facility and personnel for training and support on the ESEM.

Chapter 5, in part, is a reprint of the material as it appears in: Hsiao, Alexander P. and Heller, Michael J., "Electric-field directed self-assembly of active enzyme-nanoparticle structures", *Journal of Biomedicine and Biotechnology,* 2012, ID 178487, 9 pages, doi:10.1155/2012/178487, (2012). Copyright 2012 Alexander P. Hsiao, Michael J. Heller, Hindawee Publishing Corp. The dissertation author was the primary investigator and author of this publication.

5.7 References

1. S. Guo and S. Dong, "Biomolecule-nanoparticle hybrids for electrochemical biosensors," *TrAC Trends in Analytical Chemistry*, vol. 28, no. 1, pp. 96-109 (2009)

2. K. Ariga, Q. Ji and J. Hill, "Enzyme-Encapsulated Layer-by-Layer Assemblies: Current Status and Challenges Toward Ultimate Nanodevices " in *Advances in Polymer Science*, F. Caruso, Ed., Springer Berlin / Heidelberg, vol. 229, pp. 51-87 (2010)

3. N. K. Chaki and K. Vijayamohanan, "Self-assembled monolayers as a tunable platform for biosensor applications," *Biosensors and Bioelectronics*, vol. 17, no. 1-2, pp. 1-12 (2002)

4. Y. Kobayashi and J.-i. Anzai, "Preparation and optimization of bienzyme multilayer films using lectin and glyco-enzymes for biosensor applications," *Journal of Electroanalytical Chemistry*, vol. 507, no. 1-2, pp. 250-255 (2001)

5. B. Limoges, J. Savéant and D. Yazidi, "Avidin–Biotin Assembling of Horseradish Peroxidase Multi-Monomolecular Layers on Electrodes," *Australian Journal of Chemistry*, vol. 59, no. 4, pp. 257-259 (2006)

6. Y. Lvov, K. Ariga, I. Ichinose and T. Kunitake, "Assembly of Multicomponent Protein Films by Means of Electrostatic Layer-by-Layer Adsorption," *Journal of the American Chemical Society*, vol. 117, no. 22, pp. 6117-6123 (1995)

7. M. Onda, K. Ariga and T. Kunitake, "Activity and stability of glucose oxidase in molecular films assembled alternately with polyions," *Journal of Bioscience and Bioengineering*, vol. 87, no. 1, pp. 69-75 (1999)

8. M. Onda, Y. Lvov, K. Ariga and T. Kunitake, "Sequential actions of glucose oxidase and peroxidase in molecular films assembled by layer-by-layer alternate adsorption," *Biotechnology and Bioengineering*, vol. 51, no. 2, pp. 163-167 (1996)

9. K. L. Prime and G. M. Whitesides, "Self-assembled organic monolayers: model systems for studying adsorption of proteins at surfaces," *Science (New York, N.Y.)*, vol. 252, no. 5010, pp. 1164-7 (1991)

10. S. V. Rao, K. W. Anderson and L. G. Bachas, "Controlled layer-by-layer immobilization of horseradish peroxidase," *Biotechnology and Bioengineering*, vol. 65, no. 4, pp. 389-396 (1999)

11. T. Hoshi, N. Sagae, K. Daikuhara, K. Takahara and J.-i. Anzai, "Multilayer membranes via layer-by-layer deposition of glucose oxidase and Au nanoparticles on a Pt electrode for glucose sensing," *Materials Science and Engineering: C*, vol. 27, no. 4, pp. 890-894 (2007)

12. X.-M. Zhao, Y. Xia and G. M. Whitesides, "Soft lithographic methods for nano-fabrication," *Journal of Materials Chemistry*, vol. 7, no. 7, pp. 1069-1074 (1997)

13. S. Bharathi and M. Nogami, "A glucose biosensor based on electrodeposited biocomposites of gold nanoparticles and glucose oxidase enzyme," *Analyst*, vol. 126, no. 11, pp. 1919-1922 (2001)

14. D. A. Dehlinger, B. D. Sullivan, S. Esener and M. J. Heller, "Electric-Field-Directed Assembly of Biomolecular-Derivatized Nanoparticles into Higher-Order Structures," *Small*, vol. 3, no. 7, pp. 1237-1244 (2007)

15. S. Dey, K. Mohanta and A. J. Pal, "Magnetic-Field-Assisted Layer-by-Layer Electrostatic Assembly of Ferromagnetic Nanoparticles," *Langmuir*, vol. 26, no. 12, pp. 9627-9631 (2010)

16. M. Shao, X. Xu, J. Han, J. Zhao, W. Shi, X. Kong, M. Wei, D. G. Evans and X. Duan, "Magnetic-Field-Assisted Assembly of Layered Double Hydroxide/Metal Porphyrin Ultrathin Films and Their Application for Glucose Sensors," *Langmuir*, vol. 27, no. 13, pp. 8233-8240 (2011)

17. M. Trau, D. A. Saville and I. A. Aksay, "Field-Induced Layering of Colloidal Crystals," *Science*, vol. 272, no. 5262, pp. 706-709 (1996)

18. K. D. Barbee, A. P. Hsiao, M. J. Heller and X. Huang, "Electric field directed assembly of high-density microbead arrays," *Lab Chip*, vol. 9, no. 22, pp. 3268-74 (2009)

19. R. Krishnan, D. A. Dehlinger, G. J. Gemmen, R. L. Mifflin, S. C. Esener and M. J. Heller, "Interaction of Nanoparticles at the DEP Microelectrode Interface under High Conductance Conditions," *Electrochem commun*, vol. 11, no. 8, pp. 1661-1666 (2009)

20. R. Krishnan and M. J. Heller, "An AC electrokinetic method for enhanced detection of DNA nanoparticles," *J Biophotonics*, vol. 2, no. 4, pp. 253-61 (2009)

21. R. Krishnan, B. D. Sullivan, R. L. Mifflin, S. C. Esener and M. J. Heller, "Alternating current electrokinetic separation and detection of DNA nanoparticles in high-conductance solutions," *Electrophoresis*, vol. 29, no. 9, pp. 1765-74 (2008)

22. R. C. Bailey, K. J. Stevenson and J. T. Hupp, "Assembly of Micropatterned Colloidal Gold Thin Films via Microtransfer Molding and Electrophoretic Deposition," *Advanced Materials*, vol. 12, no. 24, pp. 1930-1934 (2000)

23. L. Besra and M. Liu, "A review on fundamentals and applications of electrophoretic deposition (EPD)," *Progress in Materials Science*, vol. 52, no. 1, pp. 1-61 (2007)

24. T. Haruyama and M. Aizawa, "Electron transfer between an electrochemically deposited glucose oxidase/Cu[II] complex and an electrode," *Biosensors and Bioelectronics*, vol. 13, no. 9, pp. 1015-1022 (1998)

25. A. L. Rogach, N. A. Kotov, D. S. Koktysh, J. W. Ostrander and G. A. Ragoisha, "Electrophoretic Deposition of Latex-Based 3D Colloidal Photonic Crystals: A Technique for Rapid Production of High-Quality Opals," *Chemistry of Materials*, vol. 12, no. 9, pp. 2721-2726 (2000)

26. L. Shi, Y. Lu, J. Sun, J. Zhang, C. Sun, J. Liu and J. Shen, "Site-Selective Lateral Multilayer Assembly of Bienzyme with Polyelectrolyte on ITO Electrode Based on Electric Field-Induced Directly Layer-by-Layer Deposition," *Biomacromolecules*, vol. 4, no. 5, pp. 1161-1167 (2003)

27. Y. Solomentsev, M. Böhmer and J. L. Anderson, "Particle Clustering and Pattern Formation during Electrophoretic Deposition: A Hydrodynamic Model," *Langmuir*, vol. 13, no. 23, pp. 6058-6068 (1997)

28. M. Trau, D. A. Saville and I. A. Aksay, "Assembly of Colloidal Crystals at Electrode Interfaces," *Langmuir*, vol. 13, no. 24, pp. 6375-6381 (1997)

29. S.-R. Yeh, M. Seul and B. I. Shraiman, "Assembly of ordered colloidal aggregrates by electric-field-induced fluid flow," *Nature*, vol. 386, no. 6620, pp. 57-59 (1997)

30. D. R. Albrecht, V. L. Tsang, R. L. Sah and S. N. Bhatia, "Photo- and electropatterning of hydrogel-encapsulated living cell arrays," *Lab on a Chip*, vol. 5, no. 1, pp. 111-118 (2005)

31. J. Cheng, E. L. Sheldon, L. Wu, A. Uribe, L. O. Gerrue, J. Carrino, M. J. Heller and J. P. O'Connell, "Preparation and hybridization analysis of DNA/RNA from E. coli on microfabricated bioelectronic chips," *Nat Biotech*, vol. 16, no. 6, pp. 541-546 (1998)

32. C. F. Edman, D. E. Raymond, D. J. Wu, E. Tu, R. G. Sosnowski, W. F. Butler, M. Nerenberg and M. J. Heller, "Electric Field Directed Nucleic Acid Hybridization on Microchips," *Nucleic Acids Research*, vol. 25, no. 24, pp. 4907-4914 (1997)

33. C. Gurtner, E. Tu, N. Jamshidi, R. W. Haigis, T. J. Onofrey, C. F. Edman, R. Sosnowski, B. Wallace and M. J. Heller, "Microelectronic array devices and techniques for electric field enhanced DNA hybridization in low-conductance buffers," *Electrophoresis*, vol. 23, no. 10, pp. 1543-50 (2002)

34. A. Kueng, C. Kranz and B. Mizaikoff, "Amperometric ATP biosensor based on polymer entrapped enzymes," *Biosensors and Bioelectronics*, vol. 19, no. 10, pp. 1301-1307 (2004)

35. R. G. Sosnowski, E. Tu, W. F. Butler, J. P. O'Connell and M. J. Heller, "Rapid determination of single base mismatch mutations in DNA hybrids by direct electric field control," *Proceedings of the National Academy of Sciences*, vol. 94, no. 4, pp. 1119-1123 (1997)

36. M. J. Heller, D. A. Dehlinger and B. D. Sullivan, "Parallel Assisted Assembly of Multilayer DNA and Protein Nanoparticle Structures Using a CMOS Electronic Array," *AIP Conference Proceedings*, vol. 859, no. 1, pp. 73-82 (2006)

37. D. Dehlinger, B. Sullivan, S. Esener, D. Hodko, P. Swanson and M. J. Heller, "Automated Combinatorial Process for Nanofabrication of Structures Using Bioderivatized Nanoparticles," *Journal of the Association for Laboratory Automation*, vol. 12, no. 5, pp. 267-276 (2007)

38. D. A. Dehlinger, B. D. Sullivan, S. Esener and M. J. Heller, "Directed Hybridization of DNA Derivatized Nanoparticles into Higher Order Structures," *Nano Letters*, vol. 8, no. 11, pp. 4053-4060 (2008)

6 CONCLUSIONS

As single-cell analysis emerges as a significant field of research, technologies are needed that allow for the high-throughput, sensitive quantification of molecules (protein, DNA, mRNA) from single-cells that will help elucidate the true state of a cell and overcome the bias of bulk analysis techniques. In particular, there is interest in developing integrated technologies able to capture many single cells, fully isolate each cell, perform cell lysis, and provide a means of sensitive and quantitative molecular analysis from each cell. This dissertation describes the development of a microfluidic platform capable of performing all the aforementioned functions.

First, I presented the foundation of the single-cell analysis platform: a microfluidic device capable of trapping, isolating, and lysing many single cells in series. Microfluidic devices consisted of a set of PDMS channels and valves bonded to a glass substrate. Single mammalian cells were captured from solution by either dielectrophoresis or hydrodynamic trapping. Captured cells were then isolated from one another using a series of PDMS pneumatic valves. Each cell could then be lysed by either electric field or chemical lysis within small nanoliter-sized compartments. These small volume compartments ensure that the released intracellular molecules are at a high concentration and provide space for incorporation of downstream analysis techniques. More complex devices integrated orthogonal side-channels for injection of lysis and

analysis reagents directly to each single-cell compartment. Future work will focus on increasing the number of traps per device, optimizing channel and valve designs for efficient cell capture, and potentially integrating methods of cell sorting and selection.

Methods were then presented for analysis of proteins using high-density antibody-conjugated microbead arrays as well as methods of integrating array assembly into the single-cell analysis device. Microfabrication is used to produce a high-density array of micron sized wells in which antibody-conjugated microbeads were electrophoretically assembled into. Filling rates of over 99% were routinely achieved. Additionally, methods of spatial and fluorescent encoding were presented to allow high degrees of multiplexing that are necessary to analyze the thousands of proteins from each cell. Using a test antigen, picomolar sensitivity was shown on the arrays. Integration of array assembly which is compatible with standard PDMS device assembly was also presented. To overcome the challenges involved in chemical surface modification and substrate activation for PDMS-glass bonding by oxygen plasma, a method of photolithographic protective patterning was described. Glass substrate surfaces were pre-functionalized with biotin-PEG and patterned using a photoresist mask before exposure to oxygen plasma in a UVO cleaner. PDMS channels and valves could then be permanently bonded to the substrates following standard device assembly methods. Protected substrate areas retained functionality and antibody-conjugated magnetic microbeads were assembled onto the surface directly in single-cell capture compartments. Future work will focus on fully integrating the antibody-conjugated microbead arrays into each compartment. With defined geometry and high-density packing, an array 250 μm by 250 μm in area can hold ten-thousand, 1 μm antibody-conjugated microbeads. Additionally, work is needed in

determining high-affinity antibody pairs capable of sub-picomolar sensitivity for protein detection at single-cell levels.

Methods were then presented for the integration of quantitative mRNA capture in the microfluidic devices for single-cell gene expression profiling applications. With mRNA copy number much lower than that of proteins, it is essential to have quantitative capture of mRNA from single cells. Chemical surface modification of the glass substrates is followed by protective patterning so that a PEG-COOH surface can be integrated directly into the single-cell analysis device. A polyT-DNA functionalized surface was shown to successfully capture mRNA molecules from solution by hybridization to the 3'-polyA tail on each transcript. Additionally, kinetics experiments showed that mRNA could be captured from HeLa cell lysates at concentrations similar to that in the compartments (1 cell per 3 nL) on the order of a few hundred seconds. This indicates that the process from cell capture to quantitative capture of mRNA transcripts can be accomplished in minutes. Additionally, single molecule mRNA capture will enable unbiased identification of each transcript by single-molecule sequencing methods. Future work will focus on fully integrating the mRNA capture methods into the devices and showing mRNA capture from individual cells. Also, integration of cDNA synthesis reactions and optimization of single-molecule sequencing will be investigated directly on-chip. This will then allow for full transcriptome profiling from many single cells in each device.

Finally, I presented work on the electric-field directed assembly of enzyme-nanoparticle layers for biosensor applications. Electric-fields were used to rapidly assemble alternating layers of enzymes and nanoparticles into higher order structures on

specified electrode sites. Following assembly, it was shown that the enzymes retained activity and that total enzyme activity could be tuned by the number of assembled layers. This shows that electric-field directed assembly is not only rapid and efficient, but gentle enough to assemble active biomolecules on the order of seconds per layer. Future work will focus on integrating multiple enzymes and increasing sensitivity of detection. Combinatorial assembly approaches could also be integrated with the electric-field assembly of antibody-conjugated microbead arrays.

The work in this dissertation encompasses the design and fabrication of a microfluidic device capable of trapping, isolating, and lysing many single cells in dedicated nanoliter-sized compartments. In addition, methods for the integration of on-chip, comprehensive and sensitive molecular analysis of protein and gene expression were developed. Future work will focus on complete integration and application of the antibody-conjugated microbead arrays for protein analysis and the polyT surface, along with single-molecule sequencing, for gene expression analysis into the cell capture compartments. Ultimately, the device will allow for protein and gene expression profiling from many single cells and aid in determining the distribution of single cell states. Applying this to areas such as the study of cancer progression, stem cell development, or drug resistance will enable the identification of unique subpopulations of cells crucial to deepening our understanding of cells and molecular pathways. In turn, this will enable improved methods for disease diagnosis and therapeutics.